

## PDF hosted at the Radboud Repository of the Radboud University Nijmegen

The following full text is a publisher's version.

For additional information about this publication click this link.

<http://hdl.handle.net/2066/19105>

Please be advised that this information was generated on 2017-12-05 and may be subject to change.

# Explorations in High Frequency EPR

ISBN 90-9015366-7

# Explorations in High Frequency EPR

Een wetenschappelijke proeve op het gebied van de Natuurwetenschappen,  
Wiskunde en Informatica

## PROEFSCHRIFT

ter verkrijging van de graad van doctor  
aan de Katholieke Universiteit Nijmegen  
volgens besluit van het College van Decanen  
in het openbaar te verdedigen op dinsdag 19 maart 2002,  
des namiddags om 3.30 uur precies.

door

Andries Hendrik Priem

geboren op 26 augustus 1971 te Leiden

Promotor: Prof. Dr. W.R. Hagen  
Copromotor: Dr. E.J. Reijerse

Manuscriptcommissie: Dr. P.J.M. van Bentum  
Dr. M.C. Feiters

## Dankwoord

...en dan is het moment daar dat je na een welgemeend 'hehe' een dankwoord in zit te tikken. Ook al is het daadwerkelijke schrijven van een proefschrift een relatief eenzame bezigheid, het onderzoek dat er voor plaats vond is dat zeker niet. Bij deze zou ik dan ook alle mensen willen bedanken die in meerdere of mindere mate een rol hebben gespeeld bij dit proefschrift.

Dat zijn allereerst alle medewerkers van de (voormalige) afdeling molecuulspectroscopie: Fred Hagen, Ed 'conceptueel hoogwerker' Reijerse, Adri Klaassen, Wiesiek Szweryn, Desiree van der Wey, Pieter van Dam en de stagiaires Sander en Dennis 'mag het 2 millimeter meer zijn'. Ik zou hun allereerst willen bedanken voor hun hulp bij dit onderzoek, en hun bijdrage aan molspec als groep. Daarnaast zou ik met name Adri Klaassen willen bedanken voor zijn niet aflatende (technische) steun als 'de aio' weer eens iets had gesloopt (D'oooh!) of het om andere redenen even niet zag zitten. Ook het feit dat Adri altijd bereid was om zijn nachtrust te verruilen voor een nacht in het magnetenlab mag niet onvermeld blijven.

Jan van Bentum heeft een grote rol gespeeld bij de totstandkoming van dit boekje. Zonder zijn hulp en meetopstelling zou dit een veel dunner proefschrift zijn geworden. Ook zou ik Jan willen bedanken voor het 'proeflezen' van hoofdstuk 2 en 3. Eric van der Horst was altijd bereid om als 'babysit' dan wel mobiel koffielurkpunt te fungeren.

Ik zou Harry, Klaas, Hung en Lijnis willen bedanken voor hun ondersteuning op de momenten dat de apparatuur in het magnetenlab even andere dingen deed dan wat ik me dacht te herinneren van de vorige keer.

Arno Kentgens zou ik willen bedanken voor het onderdak op zijn afdeling dat ik gedurende het laatste half jaar van mijn promotie heb gehad. Dankzij Rene de Gelder zijn de kristalstructuren in hoofdstuk 5 opgelost.

I would like to thank Terrence Meijer for providing me the HiPIP samples. I've had helpful discussions with Naresh Dalal about the peroxychromates, but unfortunately time was running out to convert all these discussions into experiments.

Zoals al vaker gezegd: een gezonde geest in een gezond lichaam. De trainingen van Wilbert Derks waren altijd een prettige manier om energie (en spierpijn :-)) op te doen.

De barjuffen (m/v) en ander bezoekers van café de Mark\* zorgden altijd voor een genereuze verstrekking van snok en antistressstokjes, na alle dagen dat het tegenzat. Of juist meezat. En alle dagen daartussenin.

Tenslotte zou ik vrienden (en dan met name Dave en Evert) en familie willen bedanken voor hun support gedurende de afgelopen jaren, en het aanhoren van een bijna eindeloze serie verhalen over promotiesores in alle soorten en maten.

---

\*Namen op verzoek achtergehouden



# Contents

<b>1</b>	<b>Introduction</b>	<b>9</b>
1.1	EPR vs. HF-EPR . . . . .	9
1.2	EPR of high spin systems . . . . .	13
1.3	Interpretation of ZFS parameters . . . . .	18
1.4	HF-EPR of exchange coupled systems . . . . .	20
<b>2</b>	<b>Optimizing spectrometer performance in HF-EPR by matching cavity design to sample relaxation characteristics</b>	<b>27</b>
2.1	Introduction . . . . .	27
2.2	Experimental . . . . .	29
2.3	Calculation of S/N values . . . . .	31
2.4	Relaxation and microwave power density . . . . .	32
2.5	Case studies . . . . .	35
2.6	Comparison with theory . . . . .	41
2.7	Prospects for very high frequency EPR . . . . .	43
2.8	Conclusion . . . . .	44
<b>3</b>	<b>Multi frequency analysis of high spin powder EPR spectra of Cr(III), Fe(III) and Gd(III) doped <math>\alpha</math>-alumina</b>	<b>47</b>
3.1	Introduction . . . . .	47
3.2	Experimental . . . . .	48
3.3	Results and discussion . . . . .	49
3.3.1	Cr(III) (S=3/2) in $\alpha$ -Al <sub>2</sub> O <sub>3</sub> . . . . .	50
3.3.2	Fe(III) (S=5/2) in $\alpha$ -Al <sub>2</sub> O <sub>3</sub> . . . . .	55
3.3.3	Gd(III) (S=7/2) in $\alpha$ -Al <sub>2</sub> O <sub>3</sub> . . . . .	63
3.3.4	Comparison between different spin states . . . . .	64
3.4	Structural interpretation of ZFS parameters . . . . .	66
3.5	Conclusion . . . . .	70
3.6	Acknowledgments . . . . .	70



---

<b>4</b>	<b>Effects of a distribution in Zero Field Splitting parameters on the EPR lineshape for Fe(III) in rhombic systems</b>	<b>73</b>
4.1	Introduction . . . . .	73
4.2	Method . . . . .	76
4.3	Experimental . . . . .	78
4.4	Results . . . . .	78
4.4.1	EPR of Fe(III)EDTA in water/glycerol . . . . .	79
4.4.2	Fe(III) in rubredoxin. . . . .	91
4.5	Conclusion . . . . .	95
<b>5</b>	<b>Analysis of <math>^{53}\text{Cr(V)}</math> hyperfine interaction in <math>\text{M}_3\text{CrO}_8</math> (M=Li, Na, K, Rb, Cs) compounds.</b>	<b>101</b>
5.1	Introduction . . . . .	101
5.2	Experimental . . . . .	105
5.2.1	Sample preparation . . . . .	105
5.2.2	X-ray diffraction . . . . .	106
5.3	Results . . . . .	107
5.4	Summary . . . . .	109
5.5	Acknowledgments . . . . .	110
<b>6</b>	<b>Valence isomers of biological metal clusters:multiple forms of <math>4\text{Fe-4S}^{3+}</math> clusters in HiPIPs</b>	<b>117</b>
6.1	Abstract . . . . .	117
6.2	Introduction . . . . .	118
6.3	Material & methods . . . . .	119
6.4	Results . . . . .	121
6.5	Discussion . . . . .	128
6.6	Concluding remarks . . . . .	132
6.7	Acknowledgements . . . . .	132
	<b>Summary</b>	<b>135</b>
	<b>Samenvatting</b>	<b>137</b>
	<b>Curriculum Vitae</b>	<b>139</b>

# Chapter 1

## Introduction

### 1.1 EPR vs. HF-EPR

Electron Paramagnetic Resonance (EPR), also called Electron Spin Resonance (ESR), is a technique which measures the absorption of microwave radiation by paramagnetic ions or molecules in a magnetic field. In its standard form, an EPR experiment is done by sweeping the magnetic field, and recording any changes in microwave absorption. From the field positions at which absorption takes place, and from the shape of the absorption spectrum, information of the magnetic and electronic environment of the paramagnetic center can be obtained.

The simplest paramagnetic center, and also the one which one encounters most often during EPR experiments, is a single unpaired electron, also designated as an  $S=1/2$  system. Some typical examples of  $S=1/2$  systems are free radicals, defect centers, hydrogen atoms trapped in crystal matrices and transition metals with one unpaired electron.<sup>1-7</sup>

When a magnetic field is applied to an  $S=1/2$  system, the spin of the unpaired electron can be aligned along the direction of the magnetic field ('up', or  $m_s=+1/2$ )

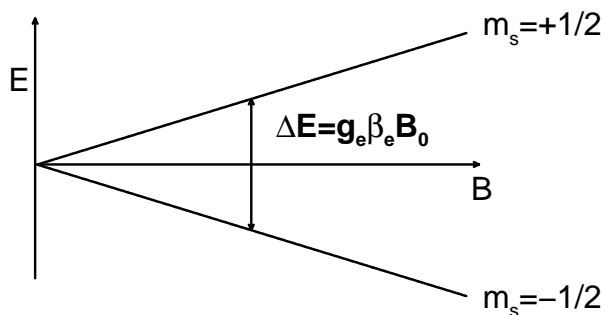


**Figure 1.1:** Splitting of the energy levels of an  $S=1/2$  system by the Zeeman effect.

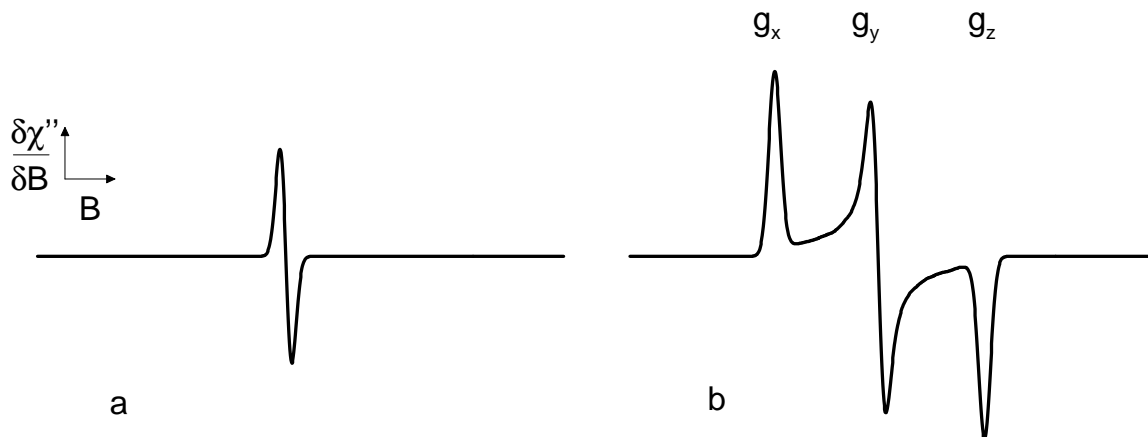


**Figure 1.2:**

**a:** EPR spectrum of a single crystal  $S=1/2$  system. The position of the resonance depends on the orientation of the sample in the magnetic field.

**b:** Powder spectrum of an  $S=1/2$  system.

or against the direction of the magnetic field ('down', or  $m_s=-1/2$ ). The two states have different energies, as indicated in Figure 1.1. This energy level splitting is known as the Zeeman effect.

The energy difference  $\Delta E$  between the two levels is given by

$$\Delta E = h\nu = g_e\beta_e B \quad (1.1)$$

where  $g_e$  is the free electron  $g$ -value (which is 2.0023),  $\beta_e$  is the Bohr magneton,  $h$  is Planck's constant, and  $B$  the external magnetic field. When an oscillating magnetic field with frequency  $\nu$  is applied (in the form of microwave radiation), transitions between the two levels can be induced.

Detection of the energy difference  $\Delta E$  could be done in two ways: by keeping the magnetic field fixed and varying the frequency of the applied electromagnetic radiation, or by using a fixed frequency source and sweeping the field. Since magnetic interactions found in EPR are usually quite large, the latter method has become standard for practical reasons. The choice of microwave frequency has more or less been dictated by the ready availability of 9 GHz microwave components. At this frequency, the field at which resonance takes place for a  $g=2$  system is approximately 0.33 Tesla. In real paramagnetic molecules, interactions with other electrons and nuclei cause the  $g$  value to differ from that of the free electron  $g$  value. In general, these effects are anisotropic.

For systems with a measurable  $g$ -anisotropy, the appearance of the EPR spectrum depends on how the spins are oriented with respect to the magnetic field. For the case of a single crystal with one paramagnetic molecule per unit cell, all molecules can be considered to have the same orientation, resulting in the single resonance

shown in the left plot of Figure 1.2a. The exact field position at which this resonance is observed depends on the orientation of the crystal with respect to the magnetic field. Systems in which all orientations are distributed evenly (ground crystals, amorphous systems and frozen solutions) give a spectrum similar to that shown in Figure 1.2b, which are also called ‘powder spectra’.

Figure 1.2b appears to be more informative, since it gives all the  $g$ -values of all three principal axes in a single experiment. However, when several interactions are present, the resulting spectrum can sometimes be too complex to allow these parameters to be determined. This is especially true when two interactions have nearly the same magnitude. In this case, single crystal EPR studies are often easier to analyze than powder spectra. However, crystals may not be always available. For example, most bioinorganic samples are only available as frozen solutions; crystal formation is notoriously difficult.

A way to circumvent this problem of spectral complexity is by measuring at several microwave frequencies. Since the Zeeman interaction is the only interaction which scales with the magnetic field,  $g$ -anisotropy can often be ignored when the measuring frequency is lowered. Similarly, when the frequency is increased, the other interactions can be regarded as a perturbation to the Zeeman interaction. This is illustrated in Figure 1.3.

The exact field at which resonance takes place is given by

$$B = \frac{h\nu}{g\beta} \quad (1.2)$$

where  $\nu$  is the microwave frequency used. If there are two different features in the spectrum, with  $g$ -values  $g_1$  and  $g_2$ , the field difference between the two features is given by

$$\Delta B = \frac{h\nu}{\beta} \left( \frac{1}{g_1} - \frac{1}{g_2} \right) \quad (1.3)$$

The above two equations show, that if the microwave frequency is doubled, the field at which resonance takes places also doubles; and that the field separation between two spectral features also doubles. If the linewidth remains constant, this means an increase in resolution, which is one of the main driving forces for doing EPR at higher frequencies. This effect is also illustrated in Figure 1.3a, which clearly shows the resolution enhancement of high frequency EPR (abbreviated: HF-EPR).

The increase in resolution combined with an increase in accuracy of  $g$ -value measurements, makes HF-EPR especially suited for studying radicals with unresolved  $g$ -anisotropy. Since the  $g$ -values of radicals are sensitive to their electronic environment, HF-EPR could be used to obtain more information on the local environment of the radical. Some typical examples are the tyrosyl radical in plant photosystem

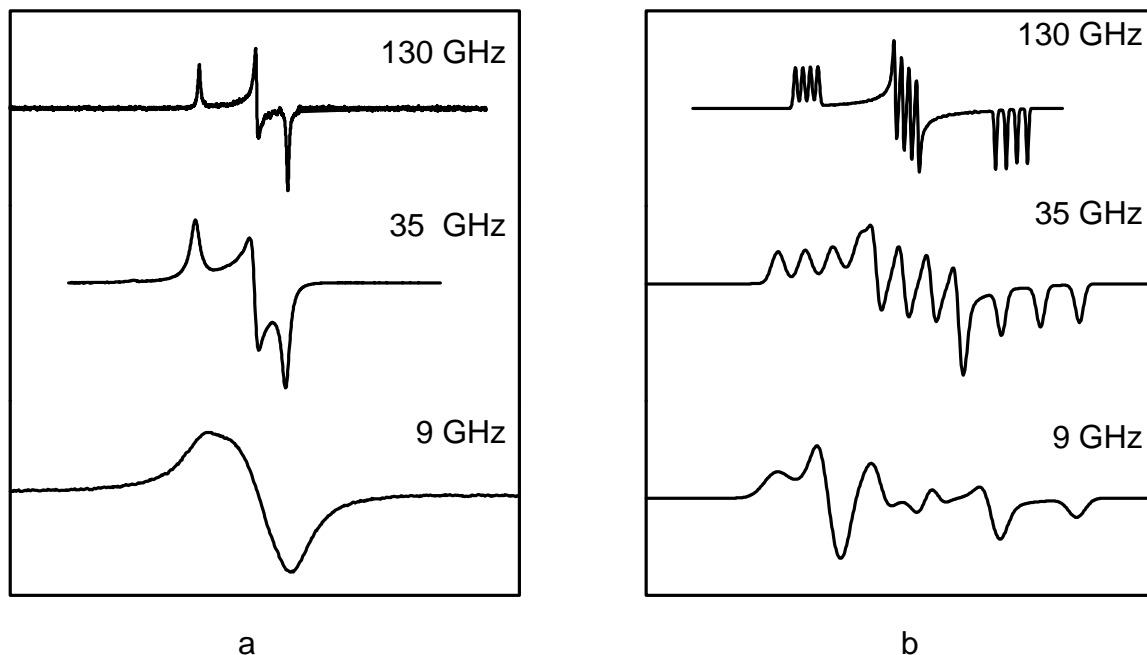


**Figure 1.3:**

**a:** Experimental EPR spectra of  $\text{Cs}_3\text{CrO}_8$ , measured at 9, 35 and 130 GHz, showing the increase in  $g$ -resolution at higher frequencies.

**b:** Simulated EPR spectra at 9, 35 and 130 GHz of an  $S=1/2, I=3/2$  system. The 9 and 35 GHz spectra are complicated by the hyperfine interaction, which is completely resolved at 130 GHz.

II (PSII),<sup>8,9</sup> bovine liver catalase,<sup>10</sup> and ribonucleotide reductase,<sup>8,11-13</sup> Other examples are tryptophanyl radical intermediates in cytochrome-c peroxidase,<sup>14</sup> and chlorophyll-a radical cations in methylene chloride.<sup>15</sup>

Another advantage of HF-EPR is that when the system does not suffer from  $g$ -strain (i.e. when the linewidth in Gauss remains the same when the frequency is increased), HF-EPR should be more sensitive than conventional EPR. In this case, as shown by Poole<sup>16</sup> and Lebedev,<sup>17</sup> the minimum detectable spin concentration scales with  $\nu^{-1/2}$ , whereas the minimum detectable number of spins scales with  $\nu^{-7/2}$ . This means that HF-EPR offers large S/N improvements for small crystals with frequency-independent linewidths, especially if these lines are relatively narrow.

When applied to liquid samples, HF-EPR can offer insight in motional dynamics, in a similar manner as HF-NMR. At conventional EPR frequencies (9 and 35 GHz), rotational dynamics in most fluids are observed on the so-called fast motional timescale, meaning that the EPR spectrum is a superposition of Lorentzian

lines whose widths are related to the correlation time  $\tau_r$ . At millimeter wave frequencies, rotational motions typically encountered are more likely to fall into a slow-motional regime on the EPR timescale. By analyzing the lineshape using the stochastic Liouville equation, combined with a model of the molecular motions, a more detailed picture of the molecular dynamics can be obtained.<sup>18-22</sup>

## 1.2 EPR of high spin systems

In the previous section, high frequency EPR of two-level ( $S=1/2$ ) spin systems was discussed. Species with more than one unpaired electron are also frequently encountered in EPR. These systems can be approximated using the following effective spin Hamiltonian:

$$H = \beta \mathbf{B} \cdot \mathbf{g} \cdot \mathbf{S} + \mathbf{S} \cdot \mathbf{D} \cdot \mathbf{S} \quad (1.4)$$

The spin-spin interaction term  $\mathbf{S} \cdot \mathbf{D} \cdot \mathbf{S}$  leads to a splitting of the energy levels, which is also present when no external magnetic field is present. Therefore, this interaction is usually referred to as zero-field splitting (ZFS), and  $\mathbf{D}$  is referred to as the zero-field tensor.  $\mathbf{D}$  has the property that it is traceless, i.e.

$$D_x + D_y + D_z = 0 \quad (1.5)$$

This allows the spin Hamiltonian given above to be written as:

$$H = \beta \mathbf{B} \cdot \mathbf{g} \cdot \mathbf{S} + D(S_z^2 - S(S+1)/3) + E(S_x^2 - S_y^2) \quad (1.6)$$

where

$$\begin{aligned} D &= \frac{3}{2}D_z \\ E &= \frac{1}{2}(D_x - D_y) \end{aligned}$$

The ZFS interaction can range from  $0.01 \text{ cm}^{-1}$  to several hundred  $\text{cm}^{-1}$ , depending on the environment of the spin system. If  $D \ll h\nu$ , the system is said to be 'completely resolved', and the spin Hamiltonian parameters  $g$  and  $D$  could, in principle, be determined directly from the spectrum.

When  $D \gg h\nu$ , the appearance of the spectrum depends on the number of unpaired electrons. In this 'weak field limit', the energy levels combine to form  $(S+1)/2$  so-called Kramers doublets. These doublets will be split apart when a magnetic field is applied, similar to the  $S=1/2$  case.

Systems with an integer number of unpaired electrons ( $S=1, 2, 3 \dots$ ) will give rise to  $S$  doublets, and a field-independent singlet, as shown in Figure 1.4. Since only

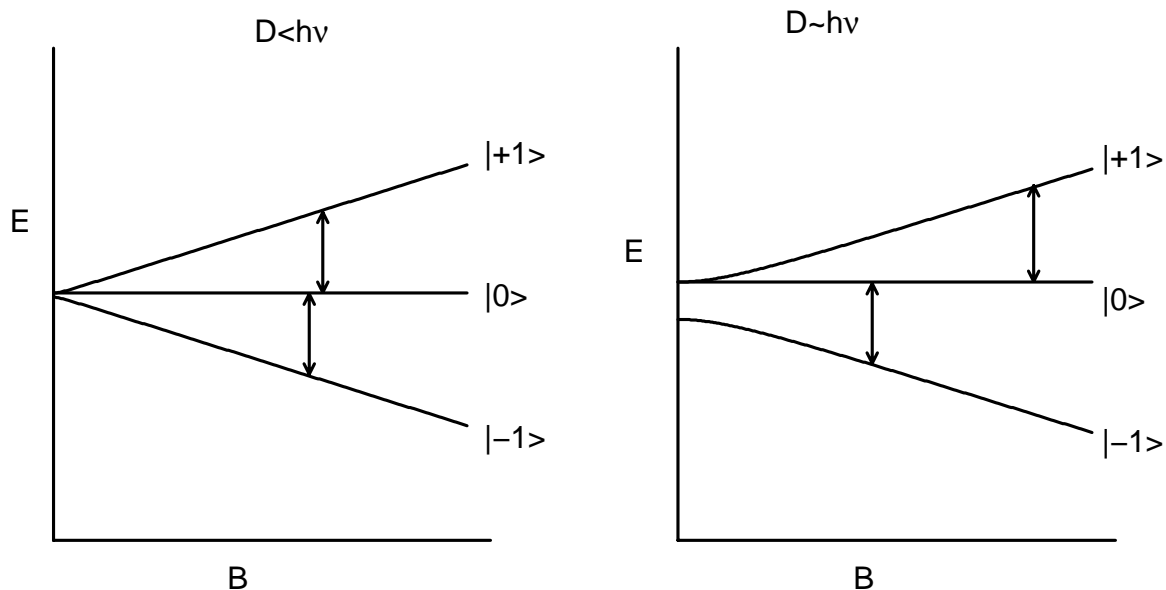


**Figure 1.4:** Zeeman levels and allowed EPR transitions for a triplet ( $S=1$ ) molecule, for  $D < h\nu$  (left) and  $D \approx h\nu$  (right). When  $D > h\nu$ , no spectrum can be observed.

transitions for which  $\Delta m_s = \pm 1$  are allowed, these systems will give no EPR spectrum when  $D > h\nu$ , and are said to be 'EPR-silent'. Increasing the microwave frequency above the ZFS will result in an observable spectrum. This has been demonstrated for several systems, e.g. aqueous chromium(II),<sup>23</sup> Mn(III) porphyrins,<sup>24</sup> Fe(II) in the reduced rubredoxin model  $\text{Fe}(\text{SPh})_4^{2-25}$  and Ni(II) in  $\text{Ni}(\text{en})_3(\text{NO}_3)_2$ .<sup>26</sup>

In contrast to integer spin systems, high-spin systems with a half-integer number of electrons ( $S=3/2$ ,  $S=5/2$ ,  $S=7/2$ ) always give an observable EPR spectrum (as far as allowed by the relaxation parameters of the particular system). Since this thesis mainly focuses on high-spin  $\text{Fe}^{3+}$ , an  $S=5/2$  system, we will limit ourselves to  $S=5/2$  systems here; the same principles discussed for  $S=5/2$  systems are also valid for  $S=3/2$  and  $S=7/2$  systems. The reader is referred to Weltner<sup>2</sup> for a general review of high spin systems. Expressions for the energy levels of  $S=3/2$  systems are given by Brickman and Kothe<sup>27</sup> and Pilbrow<sup>28</sup> in the low  $D$  limit ( $D \ll g\beta B$ ), and for  $D \gg g\beta B$  by Singer.<sup>29</sup> Energy levels of  $S=7/2$  systems (including the higher order terms  $b_4^x$  and  $b_6^x$ ) when  $D \gg h\nu$  are given by Geschwind<sup>30</sup> and Low;<sup>31</sup> Nicklin analyses  $S=7/2$  systems in the limit  $D \ll h\nu$ .<sup>32</sup>

The appearance of the EPR spectrum depends on the size of the ZFS; some typical cases are shown in Figures 1.5 to 1.7. When the ZFS is much larger than the microwave energy, which is a frequently occurring situation when measur-

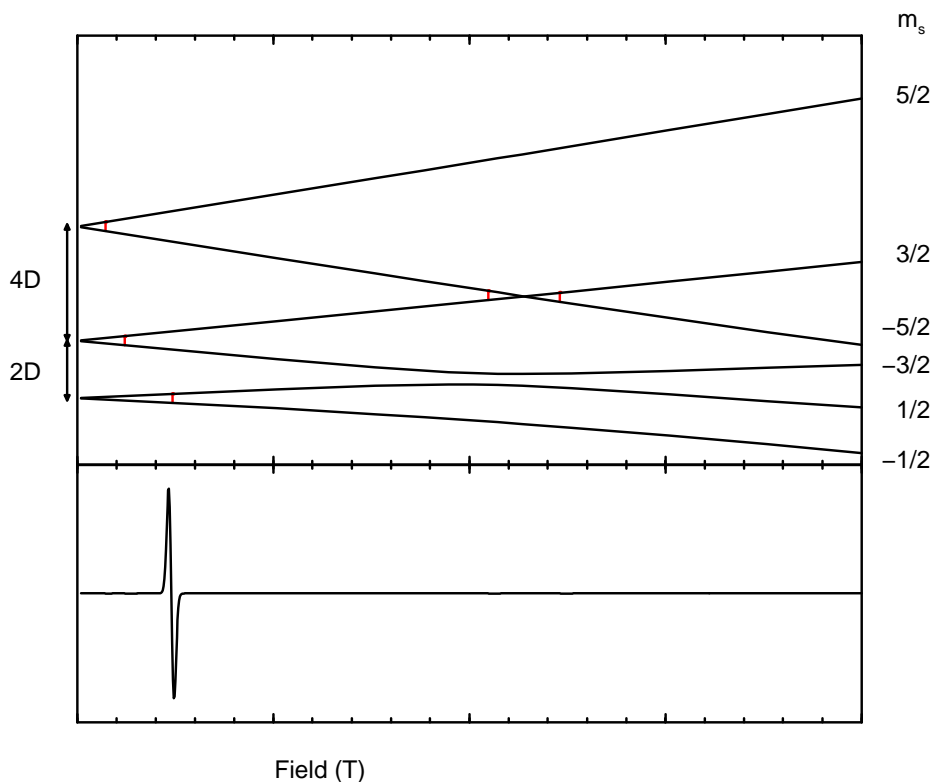


**Figure 1.5:** EPR spectrum of a single crystal axial  $S=5/2$  system when  $D \gg h\nu$ . Allowed transitions are indicated with a small bar between the energy levels.

ing bioinorganic complexes, a spectrum similar to that in the bottom of Figure 1.5 is obtained. For these systems, the microwave quantum is not large enough to bridge the gap between the Kramers doublets. Because the states are no longer true spin states, due to mixing by the zero-field splitting, the  $\Delta M_s = \pm 1$  rule no longer holds. The resultant effect is that the three transitions from within the three Kramers doublets are within the reach of the microwave quantum. Not all transitions have noticeable transition probabilities, and these are also related to the orientation of the system in the magnetic field.<sup>5,7</sup>

This figure also shows that the field positions of these peaks are no longer directly related to the real  $g$ -values of the spin system, but depend mainly on the coordination of the spin system. As a result, these  $g$ -values are also called 'effective  $g$ -values'. For example,  $S=5/2$  systems with axial symmetry are defined by effective  $g$ -values at  $g=6.0$  and  $g=2.0$ ;  $S=5/2$  systems with rhombic symmetry are characterized by effective  $g$ -values at 4.3 and 9.6.

Since there is a straightforward correlation between coordination and effective  $g$ -values, by calculating the effective  $g$ -values as a function of rhombicity, a series of so-called 'rhombograms' can be calculated, which enable to determine spin state



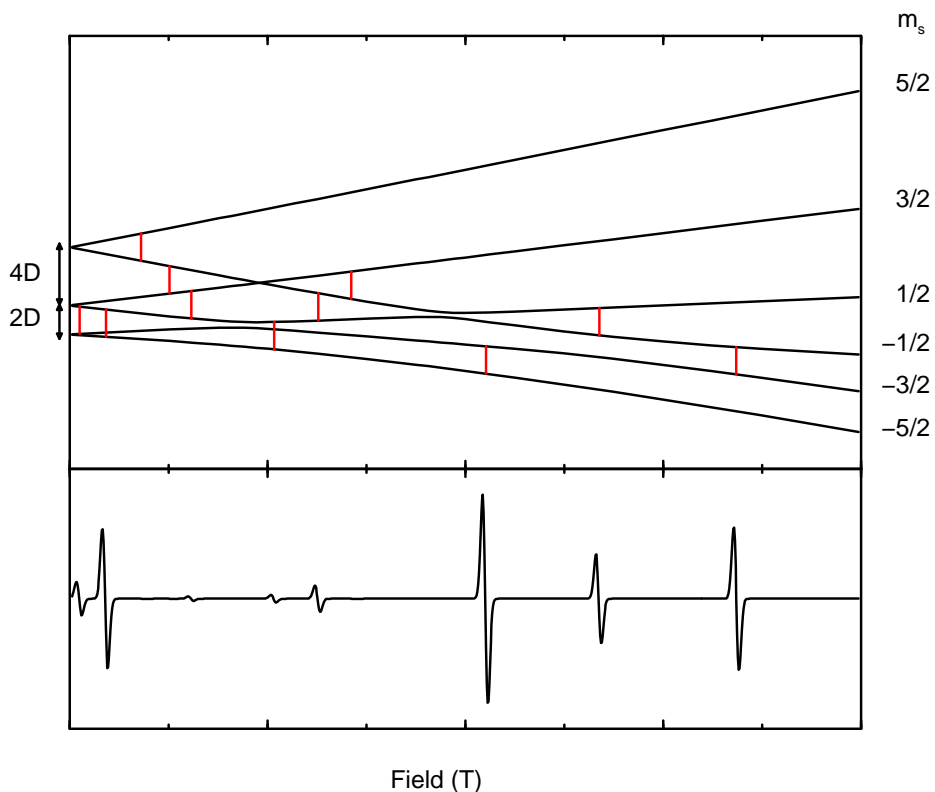


**Figure 1.6:** EPR spectrum of a single crystal axial  $S=5/2$  system when  $D \approx h\nu$ .

and the rhombicity  $E/D$  from given effective  $g$ -values.

From effective  $g$ -values, it is only possible to estimate the ratio  $E/D$ ; the size of the ZFS can only be determined indirectly from the temperature dependence of the intensity of the EPR transitions, with a relatively large error.<sup>33, 34</sup>

When the microwave frequency is increased, the effective  $g$ -values starts to shift and/or split into multiple transitions. For axial systems, this occurs when the condition  $2D \gg g_{\text{eff}}\beta B$  no longer holds; for an axial  $S=5/2$  system, the effective  $g$ -value is now given by

$$g_{\text{eff}} = 3g_{\perp} - \frac{6g_{\perp}^3\beta^2 B^2}{4D^2} \quad (1.7)$$

This was the basis for Alpert's experiment in which the  $D$ -value for methemoglobin was determined.<sup>35</sup> For rhombic systems, a similar expression can not be given since when the energy levels start to shift, the  $g=4.3$  resonance is the result of a number of overlapping resonances, which have different field dependencies depending on the  $E/D$  ratio.<sup>36, 37</sup> Generally, it can be said that the microwave frequency  $h\nu$  should be larger than  $D/3$  before the effective  $g$ -value starts to shift and/or split.

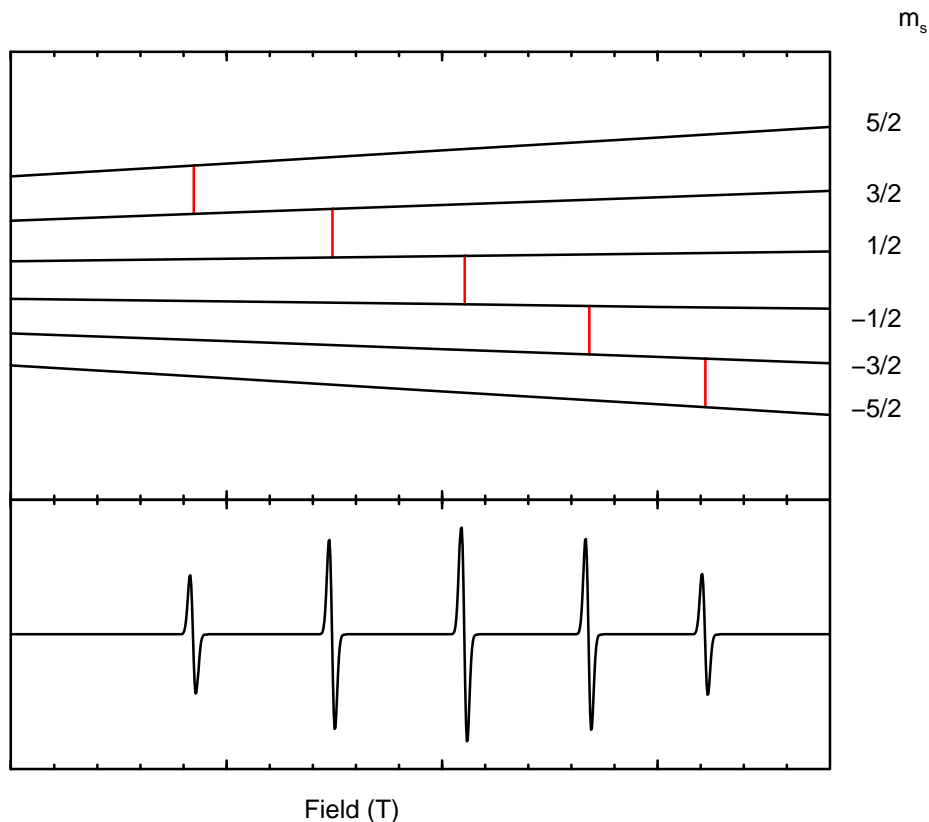


**Figure 1.7:** EPR spectrum of a single crystal axial  $S=5/2$  system when  $D \ll h\nu$ .

When  $D \approx h\nu$ , the spectrum becomes very complicated, as can be seen in Figure 1.6. In this region, the appearance of the spectrum is very sensitive to changes in the ZFS parameters. This means that spectra taken in this regime can be used to check all ZFS parameters. Unfortunately, it is not possible to give straightforward relations for the peak positions in this regime; this is especially true for powder spectra. Furthermore, peak positions and linewidths can also be obscured by distributions in ZFS parameters.

When  $D \ll h\nu$ , a spectrum similar to that in Figure 1.7 can be measured for axial systems. From this spectrum,  $D$  can be directly obtained by measuring the separations between the perpendicular transitions or parallel transitions, since these are split by  $|D|$  and  $|2D|$  respectively. In case of a slight rhombic distortion,  $E$  can be determined by measuring the splitting in the perpendicular peaks.<sup>38</sup>

### 1.3 Interpretation of ZFS parameters: The Newman superposition model

The superposition model was originally introduced to describe lanthanide crystal field parameters,<sup>39, 40</sup> but it has also been applied to describe  $3d^5$  ions as  $\text{Fe}^{3+}$  and  $\text{Mn}^{2+}$ .<sup>41, 42</sup> It has proven to be relatively succesful to estimate ZFS parameters for a known structure of a defect in a crystal.<sup>41-46</sup>

The superposition model is based on the following assumptions:

- The crystal field acting on the open-shell electrons of the paramagnetic ion is the resultant of a sum of contributions coming from individual ions in the crystal.
- Only contributions from the neighbouring ions (commonly referred to as ligands) are taken into account.
- Each single-ion contribution is axially symmetric about the line joining its center to that of the paramagnetic ion.

To simplify the interpretation, a fourth assumption is often added:

- Single-ligand contributions are dependent only on the nature of the ligand and its distance from the paramagnetic ion, and do not depend on other properties of the host crystal (e.g. polarisability).

The above assumptions essentially mean that the interaction results from overlap and covalency mechanisms. The model is not applicable in strongly ionic compounds where crystal-field calculations, such as the polarisable point-charge model, are more appropriate.<sup>47, 48</sup>

In this model, the spin Hamiltonian parameters  $D$ ,  $E$  and the higher order terms  $a$  and  $F$  can be expressed in terms of the Stevens operators  $B_k^q$  using the following relations:

$$\begin{aligned} D &= 3B_2^0 = b_2^0 & E &= B_2^2 = b_2^2/3 \\ a &= 24B_4^4 = 2b_4^4/5 & F &= 36(5B_4^0 - B_4^4) = 3(b_4^0 - b_4^4/5) \end{aligned}$$

According to the superposition model, spin Hamiltonian parameters  $B_k^q$  are given by:

$$B_k^q = \bar{B}_{k,q}(R_0) \sum K_{kq}(\theta, \phi) \left( \frac{R_0}{R_i} \right)^{t_2} \quad (1.8)$$

**Table 1.1:** Coordination factors  $K_{kq}(\theta, \phi)$  in Stevens normalization, taken from ref. 40.

k	q	$K_{kq}(\theta, \phi)$
2	0	$\frac{1}{2}(3 \cos^2 \theta - 1)2$
	1	$3 \sin 2\theta \cos \phi$
	2	$\frac{3}{2} \sin^2 \cos 2\phi$
4	0	$\frac{1}{8}(35 \cos^4 \theta - 30 \cos^2 \theta + 3)$
	1	$5(7 \cos^3 \theta - 3 \cos \theta) \sin \theta \cos \phi$
	2	$\frac{5}{2}(7 \cos^2 \theta - 1) \sin^2 \theta \cos 2\phi$
	3	$35 \cos \theta \sin^3 \theta \cos 3\phi$
6	0	$\frac{1}{16}(231 \cos^6 \theta - 315 \cos^4 \theta + 105 \cos^2 \theta - 5)$
	1	$\frac{21}{4}(33 \cos^5 \theta - 30 \cos^3 \theta + 5 \cos \theta) \sin \theta \cos \phi$
	2	$\frac{105}{32}(33 \cos^4 \theta - 18 \cos^2 \theta + 1) \sin^2 \theta \cos 2\phi$
	3	$\frac{105}{8}(11 \cos^3 \theta - 3 \cos \theta) \sin^3 \theta \cos 3\phi$
	4	$\frac{63}{16}(11 \cos^2 \theta - 1) \sin^4 \theta \cos 4\phi$
	5	$\frac{693}{8} \cos \theta \sin^5 \theta \cos 5\phi$
6	$\frac{231}{32} \sin^6 \theta \cos 6\phi$	

where  $R_i$  is the distance between the metal ion and ligand  $i$ ,  $\theta$  is the angle between the ligand and the z-axis of a Cartesian set fixed at the metal ion, and  $\phi$  is the angle in the xy-plane. Coordination factors  $K_{kq}$  are given in Table 1.1.  $\bar{B}_{k,q}(R_0)$ ,  $R_0$  and  $t_2$  are empirically determined parameters, and depend on the metal ion and ligands. Calculation of ZFS parameters using the superposition model is possible by taking values for  $R_i$ ,  $\theta$  and  $\phi$  from a crystal structure of the compound of interest, and combining these with  $\bar{B}_{k,q}(R_0)$ ,  $R_0$  and  $t_2$  as available in the literature for various metal-ligand combinations.<sup>41, 49-51</sup> For doped crystals, this approach allows the determination of the substitution site, if there are different sites in the crystal with differing geometries. For systems for which the substitution site is known, the superposition model can be used to probe the environment of the metal ion, since often the paramagnetic impurity does not occupy the exact position of the other ions in the host crystal.

This last application raises a question regarding the superposition model: the values of  $\bar{B}_{k,q}(R_0)$ ,  $R_0$  and  $t_2$  are usually determined by EPR on doped crystals and X-ray crystallography; ‘average’ values for  $\bar{B}_{k,q}(R_0)$ ,  $R_0$  and  $t_2$  for a particular metal-ligand combination are obtained by combining several systems with comparable symmetries. However, for these systems it is assumed that impurity displacements can be ignored, and do not affect  $R_0$ . The subsequent use of the superposition model to calculate impurity displacements is not an independent determination.

Another problem is of a more practical nature: the superposition model requires a value for every parameter  $\bar{B}_{k,q}(R_0)$ , if these are to be evaluated. Although values for  $\bar{B}_2^0(R_0)$  are relatively well-defined, values for  $\bar{B}_2^2(R_0)$  have been given much

less attention. This is also due to the fact that a lot of the systems studied using the superposition model are axial systems, i.e.  $E = b_2^2 = 0$ . Furthermore, especially the higher order terms are not always estimated, which means that values for  $\bar{B}_4^q(R_0)$  are scarce.

In spite of these difficulties, the superposition model is often used to calculate ZFS parameters, and gives reliable results within the errors of the model parameters.

## 1.4 HF-EPR of exchange coupled systems

The systems described previously were either radicals or single-atom spin systems. Clusters of metal ions are also frequently encountered in bioinorganic chemistry, in the form of [2Fe-2S] centers (ferredoxins, ) [3Fe-4S], [4Fe-4S] and various other forms of iron-sulfur clusters.<sup>52-54</sup> Other examples involving oxygen and nitrogen as ligands are binuclear oxo-bridged Fe(III) complexes,<sup>55-58</sup> and various 'molecular magnets' of which  $\text{Mn}_{12}\text{Ac}$  is a representative example.<sup>59-62</sup>

In these clusters, the spins on neighboring metals atoms or ions may exchange either through direct overlap of their orbitals (direct exchange) or via overlap with bridging atoms (superexchange). This effectively results in a decreased energy for the ground state of the coupled complex. The spin Hamiltonian of two spins  $S_1$  and  $S_2$  which are coupled via a direct exchange mechanism is described by the Hamiltonian:

$$H_{exchange} = -JS_1 \cdot S_2 \quad (1.9)$$

Isotropic exchange tends to align neighboring spins either parallel or anti-parallel to each other. However, in most cases the spins are also coupled indirectly through spin-orbit interaction and superexchange through neighboring ligands. For most bioinorganic clusters, superexchange is the prevailing mechanism of exchange coupling, since there usually are no direct metal-metal bonds present. Since superexchange depends on the ligands surrounding the cluster, this means that this interaction is essentially anisotropic in nature. As shown in ref. 2, p. 306ff, Equation 1.9 can be rewritten as

$$H_{exchange} = -\frac{1}{2}J(S(S+1) - \frac{3}{2}) - D(S_z^2 - \frac{1}{3}S(S+1)) + E(S_x^2 - S_y^2) \quad (1.10)$$

This expression is analogous in form to the ZFS term arising from spin-spin interaction in high spin systems. Here,  $D$  and  $E$  arise from exchange interaction, but they also include magnetic dipole-dipole interactions between unpaired spins. Since the dipolar interaction depends on the distance between the two dipoles, in absence of other anisotropic effects,  $D$  and  $E$  can provide a value for the interatomic distance. An example is the study of Fournel *et al* of trimethylamine

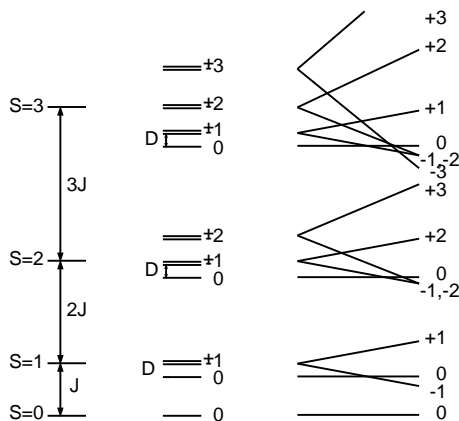


**Figure 1.8:** Schematic energy level diagram for a pair of antiferromagnetically coupled atoms with  $S_i = S_j = 3/2$  and isotropic exchange dominating. Zero-field splittings and Zeeman levels are exaggerated. (after Weltner<sup>2</sup>).

dehydrogenase, who calculated the distance between the flavin mononucleotide radical and the [4Fe-4S] cluster using HF-EPR.<sup>63</sup>

For two metal sites  $a$  and  $b$ , the spin Hamiltonian given in equation 1.10 gives rise to a so-called spin ladder of states with absolute energies

$$E_s = \frac{1}{2}J(S(S+1) - S_a(S_a+1) - S_b(S_b+1)) \quad (1.11)$$

where  $S_a$  and  $S_b$  are the spin of the individual sites, and  $S$  is the total spin of the system. Since the last two terms are constant, these are usually dropped.

The situation encountered most often experimentally is that  $J \gg D$ , and  $D$  is either small or comparable to the Zeeman interaction. This results in a series of spin states ( $S=0$ , (singlet),  $S=1$  (triplet), etc) separated by  $J, 2J, 3J \dots$ , as shown in Figure 1.8. Each of these states can be treated independently, and for each state characteristic values for  $D$  and  $E$  can be determined.

From observing the intensities of the various EPR lines as a function of temperature, one can identify to which  $S$ -value each line belongs, and also determine the spacing  $J$  between the energy levels.<sup>64</sup> In this case, HF-EPR can be used to simplify the EPR spectra of the individual spin states, just as it simplifies ‘normal’ high spin states. This is demonstrated by the work of Holgate for Fe(III)HEDTA dimers,<sup>57</sup> and by Ozarowski on Fe(III)EDTA dimers.<sup>58</sup>

When the individual spins  $S_a$  and  $S_b$  are not equal, the system can also be subject to another type of exchange interaction called double exchange, or charge delocalization.<sup>52, 65</sup> For example, an  $\text{Fe}^{3+}\text{-Fe}^{2+}$  system could be described as a mixture of the states  $\text{Fe}_a^{3+}\text{-Fe}_b^{2+}$ ,  $\text{Fe}_b^{3+}\text{-Fe}_a^{2+}$ , and all states in between, e.g.  $\text{Fe}_a^{2.5+}\text{-Fe}_b^{2.5+}$ . This

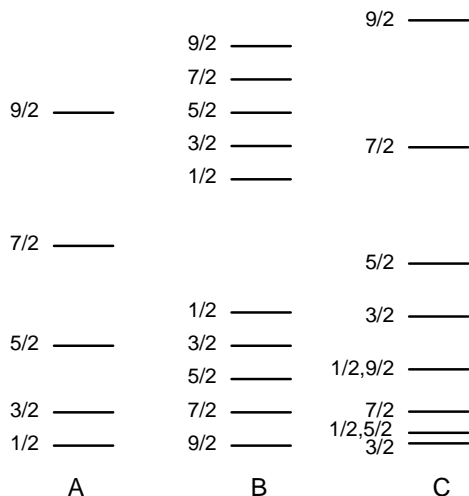


**Figure 1.9:** Spin ladder of a dinuclear Fe(III)–Fe(II) cluster subject to superexchange with  $J \gg B$  (A),  $J \ll B$  (B) or  $J = B/2$  (C). The three spin ladders are not normalized to the same energy scale. After Hagen<sup>52</sup>

results in a second term in the spin ladder equation:

$$E_s = \frac{1}{2}J(S(S+1)) \pm B(S + \frac{1}{2}) \quad (1.12)$$

in which  $B$  is a measure for the charge delocalization. Depending on the size of  $J$  and  $B$ , three different situations can occur:

$J \gg B$ : The excess electron is essentially localized, and a spin ladder as in Figure 1.9a is obtained. At low temperatures, an  $S=1/2$  spectrum would be measured.

$J \ll B$ : The excess electron is fully delocalized, and the spin states are arranged as in Figure 1.9b. The low temperature EPR is that of an  $S=9/2$  system.

$J \approx B$ : The energy levels are arranged in an irregular, nested pattern as shown in Figure 1.9c, and the EPR spectrum depends on the value of  $J/B$ .

Using HF-EPR it might be possible to measure transitions between the ground state and low-lying excited states. Although this most likely requires frequencies in the THz range, it offers a possibility of directly measuring the size of the double exchange. A proof of principle is the study of  $\text{Tm}^{3+}$  ions in lanthanum and thulium ethylsulphate.<sup>66</sup>

# Bibliography

- [1] J.A. Weil, J.R. Bolton, and J.E. Wertz. *Electron Paramagnetic Resonance: elementary theory and practical applications*. Wiley-Interscience, New York, 1994.
- [2] W. Weltner Jr. *Magnetic atoms and molecules*. Dover publications, New York, 1989.
- [3] M. Bersohn and J.C. Baird. *An introduction to electron paramagnetic resonance*. W.A. Benjamin, New York, 1966.
- [4] G. Lancaster. *Electron spin resonance in semiconductors*. Hilger & Watts, London, 1966.
- [5] I. Bertini and R.S. Drago, editors. *ESR and NMR of paramagnetic species in biological and related systems*. D. Reidel Publishing Company, Dordrecht, Holland, 1979.
- [6] W.S. Brill. *Transition metals in biochemistry*. Springer-Verlag, Berlin, 1977.
- [7] A. Abragam and B. Bleaney. *Electron paramagnetic resonance of transition ions*. Clarendon Press, Oxford, 1970.
- [8] S. Un, M. Atta, M. Fontecave, and A.W. Rutherford, *J. Am. Chem. Soc.*, **1995**, *117*, 10713.
- [9] P. Dorlet, A. Boussac, A.W. Rutherford, and S. Un, *J. Phys. Chem. B*, **1999**, *103*, 10945.
- [10] A. Ivanchich, T.A. Mattioli, and S. Un, *J. Am. Chem. Soc.*, **1999**, *121*, 5743.
- [11] A.M. Liu, A.L. Barra, H. Rubin, G.Z. Lu, and A. Graslund, *J. Am. Chem. Soc.*, **2000**, *122*, 1974.
- [12] P.J. van Dam, J.P. Willems, P.P. Schmidt, S. Potsch, A.L. Barra, W.R. Hagen, B.M. Hoffman, K.K. Andersson, and A. Graslund, *J. Am. Chem. Soc.*, **1998**, *120*, 5080.
- [13] A. Liu, S. Potsch, A. Davydov, A.L. Barra, H. Rubin, and A. Graslund, *Biochemistry*, **1998**, *37*, 16369.
- [14] A. Ivanchich, P. Dorlet, D.B. Goodin, and S. Un, *J. Am. Chem. Soc.*, **1977**, *123*, 5050.
- [15] P.J. Bratt, O.G. Poluektov, M.C. Thurnauer, J. Krzystek, L.C. Brunel, J. Schrier, Y.W. Hsiao, M. Zerner, and A. Angerhofer, *JPCb*, **2000**, *104*, 6973.
- [16] C.P. Poole. *Electron Spin Resonance*. J. Wiley, New York, 1967.
- [17] Y.S. Lebedev, *Modern pulsed and continuous-wave electron spin resonance*, (Wiley-Interscience, New York), p. 121ff, 1990.



- [18] Z. Liang and J.H. Freed, *J. Phys. Chem. B*, **1999**, *103*, 6384.
- [19] K.A. Earle, D.E. Budil, and J.H. Freed, *J. Chem. Phys.*, **1993**, *97*, 13289.
- [20] J. Pilar, J. Labsky, A. Marek, D.E. Budil, K.A. Earle, and J.H. Freed, *Macromolecules*, **2000**, *33*, 4438.
- [21] A.A. Nevzorov and J.H. Freed, *J. Chem. Phys.*, **2000**, *112*, 1413.
- [22] T.I. Smirnova, A.I. Smirnov, R.L. Belford, and R.B. Clarkson, *J. Am. Chem. Soc.*, **1998**, *120*, 5060.
- [23] J. Telser, L.A. Pardi, J. Krzystek, and L.-C. Brunel, *Inorg. Chem.*, **2000**, *37*, 5769.
- [24] D.P. Goldberg, J. Telser, J. Krzystek, A.G. Montalban, L.-C. Brunel, A.G.M. Barrett, and B.M. Hoffman, *J. Am. Chem. Soc.*, **1997**, *119*, 8722.
- [25] M.J. Knapp, J. Krzystek, L.-C. Brunel, and D.N. Hendrickson, *Inorg. Chem.*, **2000**, *39*, 281.
- [26] P.J. van Dam, A.A.K. Klaassen, E.J. Reijerse, and W.R. Hagen, *J. Mag. Res.*, **1998**, *130*, 140.
- [27] G. Brickman and G. Kothe, *J. Chem. Phys.*, **1973**, *59*, 2807.
- [28] J.R. Pilbrow, *J. Mag. Res.*, **1978**, *31*, 479.
- [29] L.S. Singer, *J. Chem. Phys.*, **1955**, *23*, 379.
- [30] S. Geschwind and J.P. Remeika, *Phys. Rev.*, **1961**, *122*, 757.
- [31] W. Low and A. Zusman, *Phys. Rev.*, **1963**, *130*, 14.
- [32] R.C. Nicklin, J.K. Johnstone, R.G. Barnes, and D.R. Wilder, *J. Chem. Phys.*, **1973**, *59*, 1652.
- [33] J. Peisach, W.E. Blumberg, S. Ogawa, E.A. Rachmilewitz, and R. Oltzik, *J. Biol. Chem.*, **1971**, *246*, 3342.
- [34] W.E. Blumberg and J. Peisach, *Ann. New York Acad. Sci.*, **1973**, *222*, 539.
- [35] Y. Alpert, Y. Couder, J. Tuchendler, and H. Thome, *Biochim. Biophys. Acta*, **1973**, *322*, 34.
- [36] R. Aasa, *J. Chem. Phys.*, **1970**, *52*, 3919.
- [37] R. Aasa, *Biochim. Biophys. Acta*, **1963**, *75*, 203.
- [38] W.B. Lynch, R.S. Boorse, and J.H. Freed, *J. Am. Chem. Soc.*, **1993**, *115*, 10909.
- [39] M.I. Bradbury and D.J. Newman, *Chem. Phys. Lett.*, **1967**, *1*, 44.
- [40] D.J. Newman and W. Urban, *Adv. Phys.*, **1975**, *24*, 793.
- [41] D.J. Newman and E. Siegel, *J. Phys. C*, **1976**, *9*, 4285.
- [42] J.M. Baker, A.A. Jenkins, and R.C.C. Ward, *J. Phys.: Condens. Matter.*, **1991**, *3*, 8467.
- [43] Y. Cohen, J. Emery, and S. Hubert, *J. Phys. Chem. Solids*, **1996**, *11*, 1683.

- [44] Z. Wen-Chen, *Physica B*, **1998**, 245, 119.
- [45] K.A. Müller and W. Berlinger, *J.Phys. C*, **1983**, 16, 6861.
- [46] J.F. Clare and S.D. Devine, *J.Phys. C*, **1984**, 17, L581.
- [47] E.J. Bijvank, H.W. den Hartog, and J. Andriessen, *Phys. Rev. B*, **1977**, 16, 1008.
- [48] N.R. Lewis and S.K. Misra, *Phys. Rev. B*, **1982**, 25, 5421.
- [49] J.M. Gaité, *Electron paramagnetic resonance of the solid state*, (The Canadian Society for Chemistry, Ottawa, Canada), p. 151, 1987.
- [50] M. Heming and G. Lehmann, *Electron paramagnetic resonance of the solid state*, (The Canadian Society for Chemistry, Ottawa, Canada), p. 163, 1987.
- [51] D.J. Newman and B. Ng, *Rep. Prog. Phys.*, **1989**, 52, 699.
- [52] W.R. Hagen, *Adv. Inorg. Chem*, **1992**, 38, 165.
- [53] B. Guigliarelli and P. Bertrand, *Adv. Inorg. Chem*, **1999**, 47, 421.
- [54] H. Beinert, R.H. Holm, and E. Münck, *Science*, **1997**, 277, 653.
- [55] D.M. Kurtz, *Chem. Rev*, **1990**, 90, 585.
- [56] K.S. Murray, *Coord. Chem. Rev*, **1974**, 12, 1.
- [57] S.J.W. Holgate, G. Bondarenko, D. Collison, and F.E. Mabbs, *Inorg. Chem.*, **1999**, 38, 2380.
- [58] A. Ozarowski, B.R. McGarvey, and J.E. Drake, *Inorg. Chem.*, **1995**, 34, 5558.
- [59] A. Bouwen, A. Caneschi, D. Gatteschi, E. Goovaerts, D.Schoemaker, L. Sorace, and M. Stefan, *J. Phys. Chem. B*, **2001**, 105, 2658.
- [60] A.L. Barra, D. Gatteschi, and R. Sessoli, *Chemistry*, **2000**, 6, 1608.
- [61] A.A. Mukhin, V.D. Travkin, A.K. Zvezdin, A. Caneschi, D. Gatteschi, and R. Sessoli, *Physica B*, **2000**, 284, 1221.
- [62] D. Burdinski, E. Bill, F. Birkelbach, K. Wieghardt, and P. Chaudhuri, *Inorg. Chem.*, **2001**, 40, 1160.
- [63] A. Fournel, S. Gambarelli, B. Guigliarelli, C. More, M. Asso, G. Chouteau, R. Hille, and P. Bertrand, *J. Chem. Phys.*, **1998**, 109, 10905.
- [64] M.T. Hutchings, R.J. Birgenau, and W.P. Wolfe, *Phys. Rev.*, **1968**, 168, 1026.
- [65] P.W. Anderson and H. Hasegawa, *Phys. Rev.*, **1955**, 100, 675.
- [66] H.P. Moll, J. van Tol, P. Wyder, M.S. Tagirov, and D.A. Tayurskii, *Phys. Rev. Lett.*, **1996**, 77, 3459.



## Chapter 2

# Optimizing spectrometer performance in HF-EPR by matching cavity design to sample relaxation characteristics

### 2.1 Introduction

In the last decade, there has been an increasing interest in EPR at high frequencies (95 GHz and up).<sup>1-5</sup> The main reasons of this interest are the potential increase in resolution and sensitivity at higher fields, analogous to the trends observed in high frequency NMR. High-frequency EPR (HF-EPR) also offers possibilities which have no counterpart in high frequency NMR, such as the possibility of studying systems which were previously 'EPR silent': integer spin systems with a zero field splitting (ZFS) larger than the microwave quantum.<sup>6-9</sup> These systems give no EPR spectra at conventional EPR frequencies. HF-EPR can also be used to obtain more information on high spin systems with intermediate zero field splittings; EPR at conventional frequencies only yields an estimate of the ZFS, whereas HF-EPR at sufficiently high frequencies can provide all spin Hamiltonian parameters.<sup>3-5</sup>

In most conventional 9 GHz CW-EPR spectrometers, the signal is detected using magnetic field modulation.<sup>10</sup> A common problem encountered in EPR is finding the experimental conditions to obtain a spectrum with a maximal signal to noise ratio (S/N). For example, when measuring samples with large linewidths (>50 Gauss), S/N will initially increase when the modulation amplitude is increased; but above a certain (spectrometer-dependent) limit, the forces exerted by the modulation coils on the cavity will result in microphonic interference, which is visi-

ble as additional noise, resulting in a decrease in S/N. This problem occurs for both conventional and HF-EPR spectrometers, but due to increasing linewidths at higher frequencies ( $g$ -strain)<sup>11</sup> and the stronger magnetic fields used in HF-EPR, it can be more pronounced in HF-EPR.

In a similar way, the optimal measuring temperature is defined by relaxation processes and microwave power. When the measured spectrum shows signs of saturation, this can usually be solved by either lowering the amount of incident microwave power on the sample, or by increasing the sample temperature, which increases  $1/T_1$ . An overview of these effects and their interpretation has been given by Mailer and Taylor.<sup>12</sup> Conventional EPR spectrometers have a dynamic range (in incident power) of typically 60 dB. This usually leaves enough room to prevent saturation. HF-EPR spectrometers have a much smaller dynamic range, typically 20–30 dB. Additionally, the microwave power density ( $B_1$  field) in the cavity is much larger, due to the smaller size of the resonators employed in HF-EPR.

In this communication it is argued that to obtain the highest possible S/N, the resonator in which the sample is measured should be adapted to the sample's relaxation behavior and less so to its dielectric losses. In practice, S/N is strongly dependent on the relaxation behavior of the sample; resonator geometry and measuring temperature should be adapted to suit this. Samples with large  $T_1$ -values should be studied in resonators with a small power density, compensated by a large filling factor, i.e. oversized resonators. Samples with very small  $T_1$ -values should be studied in resonators with a high power density, i.e. single-mode resonators.

The notion that the choice of microwave resonator is dictated by the sample is not a new one, as this has also been proposed by Freed and others.<sup>13–15</sup> However, their line of reasoning was primarily focused on sample loss and sample size; the effects of the relaxation behavior of the sample on the S/N were ignored in their analysis. In practice, relaxation behavior is a far more limiting parameter than sample loss.

In the initial development of HF-EPR spectrometers, the standard design of the X-band EPR spectrometer (using single-mode waveguide, circulators and single-mode resonators) was 'translated' to higher frequencies. Up to 150 GHz, the scaling principle works quite satisfactory, although the mm-wave radiation already has to be propagated through oversized rectangular waveguides in order to prevent excessive losses. At frequencies higher than 150 GHz, passive waveguide components (circulators, couplers, attenuators) are no longer available, and are replaced with equivalent quasi-optical components.<sup>13</sup>

Although there is general agreement on the benefits (in terms of microwave power loss) of using 'quasi-optical' oversized circular waveguide instead of single-mode waveguide, most laboratories still use a single-mode resonator, or a Fabry-Perot resonator as a close approximation.<sup>16, 17</sup> This design choice is often motivated by

a wish to decrease sample volume, the need to concentrate microwave power as a compensation for low-power microwave sources and sometimes dictated by the available magnetic field homogeneity.

A disadvantage of single-mode and Fabry-Perot resonators is that they are delicate instruments, and require careful design and operation. Furthermore, in most cases, HF-EPR studies are preceded by measurements at 9 GHz, which means that the smaller sample volume (0.5-1  $\mu\text{L}$  vs. 100-200  $\mu\text{L}$ ) required in HF-EPR might be an irrelevant advantage from the point of view of the biologist or chemist involved. Furthermore, measurement of oxygen-sensitive samples using limited sample volumes is still a nontrivial operation at most laboratories. Oversized resonators and other non-resonant structures have less stringent spatial requirements, and their simpler design allows for a relatively easy sample handling.

However, as indicated above, there are also spectroscopical reasons to carefully choose the resonator used in the measurements. The need for this choice is demonstrated below by comparing a number of typical samples with widely differing relaxation parameters measured in three different HF-EPR setups with varying microwave power densities: a single-mode resonator, a reflection setup which focuses the microwave radiation back and forth from a circular single-mode pipe (which is called here 'the non-resonant single-mode setup'), and a non-resonant transmission setup, in which the sample is placed in the center of a quasi-optical waveguide.

Also, we would like to check whether it is possible to make a reasonable estimate in advance of the expected S/N of a given sample for the different setups given above. Expressions for S/N are given by Poole,<sup>10</sup> it would be useful to see if these expressions give correct S/N numbers for the samples used in these studies.

## 2.2 Experimental

In an ideal comparison between two resonator geometries, the only variable would be the resonator itself. Unfortunately, due to technical and practical reasons this turned out to be impossible.

A 130 GHz microwave bridge (V. N. Krymov, Donetsk) delivering 10 mW power was used as the microwave source in all setups. In the single-mode setup (which has also been described elsewhere)<sup>18, 19</sup> the microwave radiation is propagated to the cavity using oversized rectangular waveguide. The cavity is a  $\text{TE}_{011}$  cylindrical resonator, with a sample volume of approximately 0.5 mm<sup>3</sup>. The resonance frequency and microwave coupling of the cavity can be controlled externally. An InSb bolometer/mixer operating at 4.2 K is used for detection. The (absolute) sensitivity of this system is approximately 10<sup>10</sup> spins/Gauss.<sup>18</sup>

The non-resonant single-mode setup has been described in detail by van der

Horst.<sup>20</sup> Its operation can be summarized as follows: A feedhorn converts the single-mode waveguide output of the 130 GHz bridge to a Gaussian free-space beam. A mylar beam splitter mounted at a 45 degree angle, is used as a quasi-optical magic T, and splits the mm-wave radiation in two beams perpendicular to each other. The first beam is transferred using oversized circular waveguides (13 mm brass pipe) to a small brass pipe annex sample holder (dimensions 2.8x20 mm) connected at the end of the oversized circular waveguide using a 10 cm long brass taper. At the end of this pipe a small 7x7 mm Si wafer (coated with a few  $\mu\text{m}$  gold) is used as mirror. The reflected signal from the sample is passed again through the beam splitter, which couples half of the reflected microwave radiation onto the bolometer. The beam reflected by the beam splitter effectively functions as a reference arm; this radiation is reflected via an adjustable mirror back to the bolometer detector, thus enabling phase adjustment of the EPR signal.

Although this system is called a non-resonant single-mode setup, perhaps it could technically be better described as a shorted waveguide. For this frequency, the modes above cutoff are the  $\text{TE}_{01}$ ,  $\text{TE}_{11}$ ,  $\text{TE}_{21}$ ,  $\text{TM}_{01}$  and  $\text{TM}_{11}$  modes.<sup>10</sup> Due to inaccurate mode conversion, a small but nonnegligible field along the  $B_0$  field is also present. However, in the systems studied here, this field does not induce EPR transitions.

The non-resonant setup is similar to the non-resonant single-mode setup, except that the sample is contained in a Teflon sample holder (dimensions 5 x 25 mm), which is placed in the center of the oversized circular waveguide. This setup in its present form only allows measurements at room temperature, and allows the sample to be measured in either a pure transmission geometry or a reflection geometry. If the setup is used in transmission geometry, only limited phase adjustment is possible, using the phase-shift of the PIN-attenuators of the D-band bridge. In reflection geometry, the reference arm in the D-band bridge can be used to control the microwave phase, in a similar way as the beam splitter of the nonresonant single-mode setup.

Due to mixed propagation modes in the smooth oversized guides the phase of the experimental spectrum is often difficult to control, and depends, amongst other things, on the sample size and its dielectric properties. In both setups therefore, one essentially measures an arbitrary combination of absorption and dispersion.

To obtain 'correct' EPR spectra, a phase correction similar to that described by Earle *et al.*<sup>4</sup> was applied. In our procedure, a phase shift was applied to an FFT of the data, and an inverse FFT of the phase-shifted data then gave the 'correct' experimental spectrum. The correct phase shift is defined as that for which the lineshape of a reference compound with a known lineshape ( $\text{Mn}^{2+}$  in  $\text{MgO}$ ) is symmetrical around the baseline.

### 2.3 Calculation of S/N values

The average microwave power inside a rectangular single mode cavity can be calculated using<sup>10</sup>

$$\langle B_1^2 \rangle_c = (abZ_{TE})^{-1} P_w Q_L \frac{V_w}{V_c}. \quad (2.1)$$

The first factor contains the cross section dimensions  $a, b$  of the coupling waveguide as well as its characteristic impedance  $Z_{TE} \approx 533\Omega$ .  $P_w$  is the microwave power at the cavity,  $Q_L$  is the quality factor of the coupled resonator,  $V_w$  is the volume of a waveguide over one wavelength and  $V_c$  is the volume of the cavity. The  $B_1$  field at the sample however, also depends on the filling factor  $\eta$ . The filling factor can be defined as:

$$\eta = \frac{V_s \langle B_1^2 \rangle_s}{V_c \langle B_1^2 \rangle_c} \quad (2.2)$$

In general the sample volume  $V_s$  and the cavity volume  $V_c$  can be easily determined. The  $B_1$  terms however need integration of the magnetic field  $B_1$  over cavity and sample, respectively. Values for these terms have been estimated for several cavity geometries.<sup>10</sup> For cylindrical  $TE_{011}$  cavities as used in the 35 GHz and the 130 GHz single-mode setup, equation 2.2 can be written as:

$$\eta \approx 4 \frac{V_s}{V_c} \quad (2.3)$$

For the rectangular cavity used at X-band, equation 2.4 is valid:

$$\eta = 2 \frac{V_s}{V_c} \quad (2.4)$$

Combining equation 2.1 and 2.2 gives the average field at the sample:

$$\langle B_1^2 \rangle_s = (abZ_{TE})^{-1} P_w Q_L \eta \frac{V_w}{V_s} \quad (2.5)$$

The sensitivity of a setup can be expressed as the minimum number of detectable spins  $N_{min}$ .<sup>10</sup>

$$N_{min} = \frac{6V_c k T_s}{\mu_0 g^2 \beta^2 S(S+1) Q_u} \left( \frac{\Delta B_{pp}}{B_0} \right) \left( \frac{\Delta B_{pp}}{B_{mod}} \right) \left( \frac{F k T_d \Delta f}{P_w} \right)^{1/2} \quad (2.6)$$

where  $T_s$  is the temperature of the sample,  $T_d$  the operating temperature of the mm-wave detector,  $\Delta f$  represents the corresponding noise bandwidth,  $F$  is the noise factor of the detection system,  $B_0$  is the field at the sample,  $\Delta B_{pp}$  is the peak-to-peak linewidth, and  $B_{mod}$  is the field modulation amplitude. In this equation,



an erroneous factor  $\omega_0$  has been omitted (see also ref. 21 p. 500ff) Approximating the filling factor with  $\eta = V_s/V_c$  one can write for the concentration sensitivity:

$$\frac{N_{min}}{V_s} = \frac{6kT_s}{\mu_0 g^2 \beta^2 S(S+1) Q_u \eta} \left( \frac{\Delta B_{pp}}{B_0} \right) \left( \frac{\Delta B_{pp}}{B_{mod}} \right) \left( \frac{FkT_d \Delta f}{P_w} \right)^{1/2} \quad (2.7)$$

In case of a non-resonant system where the waveguide is filled over a certain length  $l$  with sample  $Q_u$  and  $\eta$  is equal to unity, and the sensitivity is given by:

$$\frac{N_{min}}{V_s} = \frac{6kT_s}{\mu_0 g^2 \beta^2 S(S+1) l / \lambda_g} \left( \frac{\Delta B_{pp}}{B_0} \right) \left( \frac{\Delta B_{pp}}{B_{mod}} \right) \left( \frac{FkT_d \Delta f}{P_w} \right)^{1/2} \quad (2.8)$$

where  $\lambda_g$  represents the wavelength of the mm-wave radiation in the waveguide. The concentration sensitivity thus depends on the sample height (in wavelengths). The actual S/N ratio  $y'_m$  in an experiment can now be obtained from:

$$y'_m = \frac{N_{spin}}{N_{min}} \quad (2.9)$$

where  $N_{spin}$  is the number of spins in the sample. Using the experimental parameters given in Table 2.1 the characteristics of each setup ( $B_1$  and sensitivity) can now be calculated.

## 2.4 Relaxation and microwave power density

Generally, measurements should be done under the condition that the signal shows no signs of saturation, i.e. equation 2.10 holds:

$$T_1 < \frac{1}{2T_2 \gamma^2 B_1^2} \quad (2.10)$$

where  $T_1$  is the electron spin-lattice relaxation time,  $\gamma$  is the electron gyromagnetic ratio,  $T_2$  is the spin-spin relaxation time, and  $B_1$  is the microwave magnetic field at the sample.

From equation 2.5, which gives the  $B_1$  field at the sample, one would like to determine the best setup and measuring conditions using graphs similar to that shown in Figure 2.1. Although plots like these can give insight in the general principles involved, they are of limited practical value for the following reasons:

- Estimation of  $T_1$  values depend on an accurate value of the microwave power density in the cavity  $P_w$  of a spectrometer operating at conventional microwave frequencies, combined with a value for  $P_w$  of the HF-EPR spectrometer. Both quantities are difficult to determine with reasonable accuracy, especially when different resonator geometries are used.

**Table 2.1:** Parameters of the different HF-EPR setups used in this study. The 9 and 35 GHz are included for comparison.  $P_w$  is the microwave power at the cavity;  $V_w$ ,  $V_c$  and  $V_s$  are the volume of a waveguide over one wavelength, the cavity volume, and the sample volume respectively.  $\eta$  is the filling factor. For all systems except the non-resonant single-mode setup, the sensitivity was measured at room temperature using a sample containing 0.003%  $\text{Mn}^{2+}$  in MgO (Baker).<sup>18</sup> The sensitivity of the non-resonant single-mode setup was estimated using a sample with approximately 0.1%  $\text{Fe}^{3+}$  in  $\alpha\text{-Al}_2\text{O}_3$ , measured at 80 K. Sensitivity values are given for a signal-to-noise ratio of 1. All measurements were performed using time constants in the range of 100–300 ms.

Frequency Resonator	9 rectangular TE <sub>102</sub>	35 cylindrical TE <sub>011</sub>	130 cylindrical TE <sub>011</sub>	130 cylindrical, non-resonant	130 non-resonant
$P_w$ (mW)	2	2	1	$\approx 1$	2
$Q_L$	5000	2000	1000	1	1
sample dimensions (height $\times$ radius, mm)	22x1.5	11x1	2.5x0.25	20x1.4	20x 2.5
$V_w$ (mm <sup>3</sup> )	9920	290	3.26	14.2	300
$V_c$ (mm <sup>3</sup> )	8800	1050	43	123	2500
$V_s$ (mm <sup>3</sup> )	155	34.6	0.48	123	390
$B_1$ (cavity, mGauss)	12.5	3.9	1.2	0.048	0.070
$B_1$ (sample, $\mu\text{T}$ )	17.8	8.0	2.5	0.048	0.14
$\eta$	0.035	0.135	0.05	1.0	0.64
sensitivity (spins g <sup>-1</sup> )	$4 \cdot 10^{12}$	$7 \cdot 10^{11}$	$1 \cdot 10^{10}$	$\approx 5 \cdot 10^{12}$	$6 \cdot 10^{13}$
concentration sensitivity (spins g <sup>-1</sup> mm <sup>-3</sup> )	$3 \cdot 10^{10}$	$2 \cdot 10^{10}$	$2 \cdot 10^{10}$	$\approx 5 \cdot 10^{10}$	$2 \cdot 10^{11}$
Typical field modulation frequency (kHz)	100	80	24	11	24
Typical field modulation amplitude (Gauss)	5	5	5	5	5

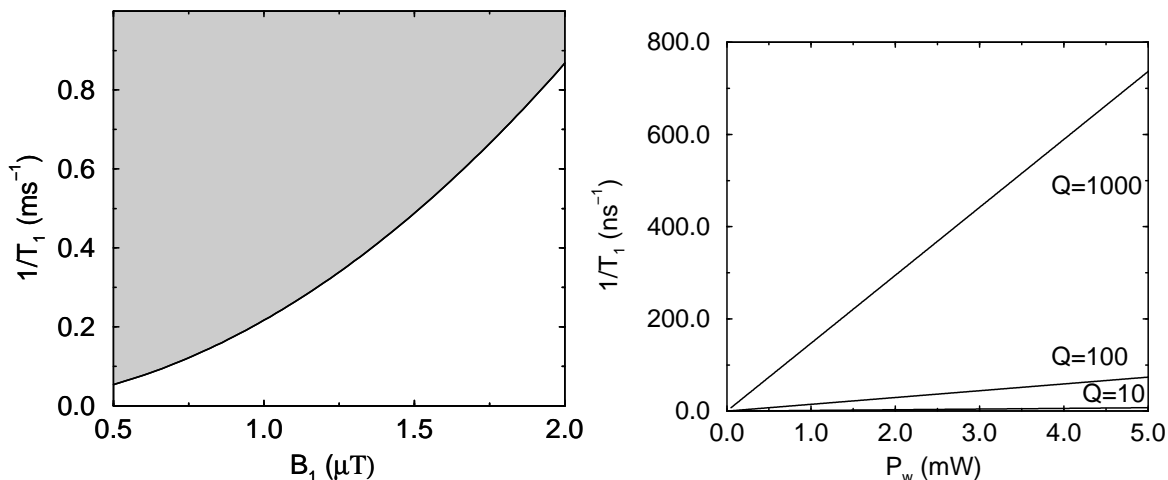


**Figure 2.1:**

**Left:** Plot of  $1/T_1$  against  $B_1$ , using equation 2.10 and a  $T_2$  value of 7 ns (which is equivalent to a linewidth of 50 Gauss). The grayed area shows the  $B_1/T_1$  combination for which the EPR signal will not be saturated.

**Right:** Plot of  $1/T_1$  against microwave power  $P_w$ , as calculated for the resonant single-mode setup using equation 2.1, for various Q-values. Measurements without saturation are possible in the area above each line.

- $T_1$  values are temperature-dependent, which means that a series of  $T_1$  measurements have to be made. In some cases, just doing the HF-EPR experiment might be a lot faster and easier than measuring the  $T_1$  values in the temperature range in which the HF-EPR experiment will be performed.
- Some samples have relaxation properties which do not allow the determination of a value for  $T_1$ , but only limiting values, since the experimental conditions (saturation, or inversion recovery) needed to determine  $T_1$  values can not always be met at all temperatures. Furthermore, high spin systems with intermediate ZFS can have different relaxation mechanisms when the microwave frequency is at or below the ZFS, compared to when the microwave frequency is far above the ZFS.
- For liquid samples it can be assumed that  $T_2 \approx T_1$ ; for solid or frozen samples  $T_2 \ll T_1$ , and can be estimated from the linewidth. Estimation of  $T_2$  is often complicated by  $g$ -strain and the presence of several  $T_2$ -mechanisms affecting spin-spin relaxation.

In short, although it is theoretically possible to determine the relaxation parameters beforehand, and thus determine the optimum conditions for the HF-EPR experiment, in practice, this method takes too much effort to be practical. However,

**Table 2.2:** EPR parameters of the samples used in this study.

Sample	HiPIP	Fe:Al <sub>2</sub> O <sub>3</sub>	Rubredoxin
concentration (mM)	10	10	10
$\Delta B_{pp}$ (Gauss) @ 9 GHz	20	25	20
$\Delta B_{pp}$ (Gauss) @ 35 GHz	35	50	50
$\Delta B_{pp}$ (Gauss) @ 130 GHz	140	50	2000
Spin	1/2	5/2	5/2

in a qualitative way it is possible to make reasonable guesses which setup (non-resonant or single-mode) will give optimal results. For example, samples with a tendency to saturate readily (i.e. below 30 K at X-band) are essentially impossible to measure at low temperatures in a single-mode resonator at 130 GHz. On the other hand, systems that show no signs of saturation at 35 GHz at 4 K are most likely good candidates for HF-EPR using a single-mode cavity.

It should be noted that saturation of the absorption (which is dependent on  $T_1$ ) is assumed to be frequency-independent. This appears to be a reasonable assumption, since for  $S = 1/2$ , only at very low temperatures (<4 K), when relaxation proceeds via direct processes, a frequency-dependent term is found.<sup>22,23</sup> For high spin systems with zero field splittings well below the measuring frequency, there is no frequency dependent relaxation at all, as has been noted by Orbach.<sup>22</sup>

## 2.5 Case studies

### Case 1: a biological $S=1/2$ system

A typical example of a biological  $S=1/2$  system is shown in Figure 2.2. The middle trace shows the  $[4Fe-4S]^{3+}$  cluster in a high potential iron sulfur protein (0.50  $\mu$ L) HiPIP measured in a single-mode resonator at 30 K. A difficulty in this experiment is that at high temperatures the lines are severely lifetime-broadened, and have low intensity due to Boltzmann statistics. At intermediate temperatures, relaxation rates decrease rapidly with temperature, which cause the absorption to be readily saturated, so that only dispersion spectra can be measured. Conventional EPR experience dictates that in such cases the power density at the sample should be decreased by attenuating the microwave power. At 9 GHz, this is often no problem, since the sensitivity of the spectrometer allows a decrease in microwave power by 20–30 dB most of the times.

At 130 GHz, this is complicated by the fact that this sample is subject to  $g$ -strain: At 9 GHz, the whole spectrum encompasses 200 Gauss, however, at 130 GHz, the spectrum is spread over 2800 Gauss, which means that the intensity of the spectrum will be 100 times (20 dB) lower relative to the 9 GHz spectrum. Since the

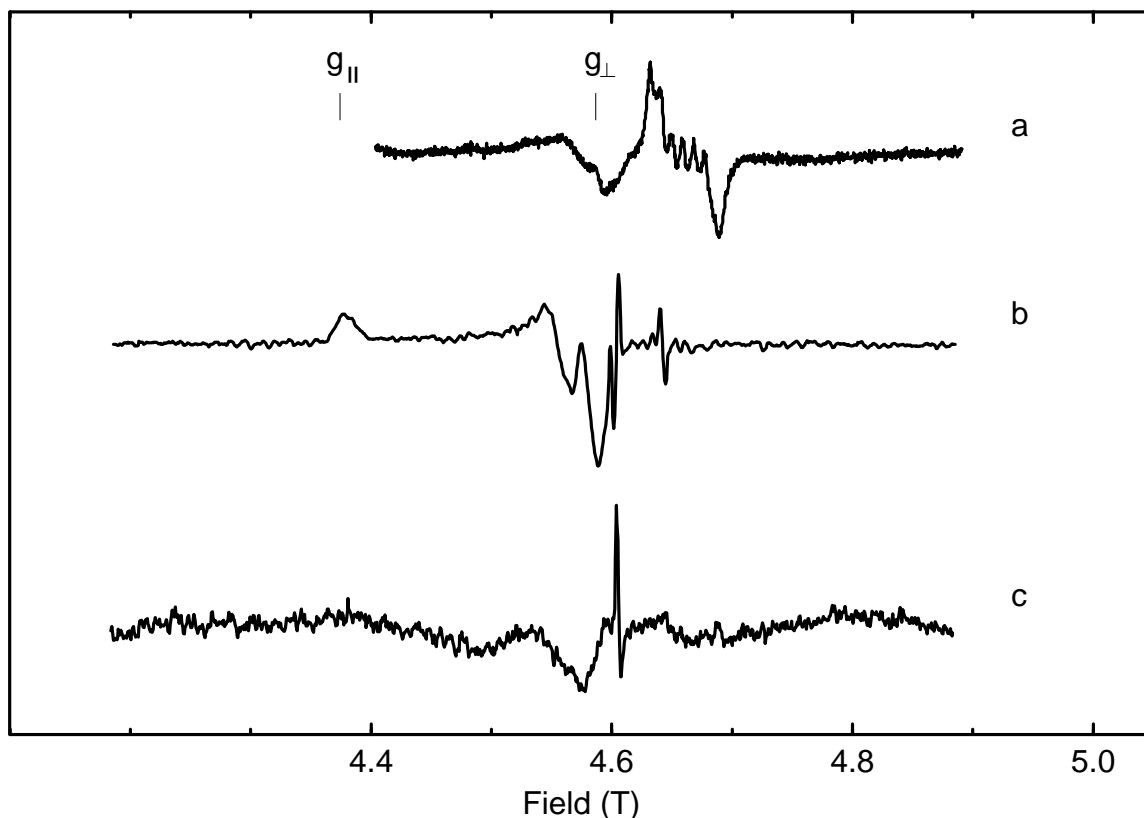


**Figure 2.2:** 130.0 GHz spectra of 10 mM HiPIP from *Chromatium vinosum*, showing the S/N of typical HF-EPR experiments on bioinorganic systems. The positions of  $g_{||}$  and  $g_{\perp}$  are indicated in this figure.

**a:** Measured in the non-resonant single-mode setup, single scan. Experimental conditions:  $T=20\text{K}$ , microwave power 4 mW, modulation frequency 11.3 kHz, modulation amplitude 3 Gauss, sample volume  $50\ \mu\text{L}$ .

**b:** Measured in a single-mode resonator. This spectrum is the result of taking the first derivative of 8 combined spectra measured in absorption. Experimental conditions:  $T=30\text{K}$ , microwave power 0.5mW, modulation frequency 24.6 kHz, modulation amplitude 5 Gauss, sample volume  $0.5\ \mu\text{L}$ .

**c:** Measured in a single-mode resonator. This is a typical spectrum obtained when trying to avoid dispersion-like conditions. Experimental conditions:  $T=45\text{K}$ , microwave power 0.1mW, modulation frequency 24.6 kHz, modulation amplitude 5 Gauss, sample volume  $0.5\ \mu\text{L}$ .

The sharp peak visible in the single-mode spectra is an unknown contamination; the series of small peaks in the non-resonant single-mode spectrum probably originate from residual coordinated  $\text{Mn}^{2+}$ .

amount of field modulation can not be increased by a similar factor, this means that to observe any signal (absorption or dispersion), almost maximum microwave power is needed, or the signal will be below the noise floor. The net effect is that the available temperature window for obtaining derivative spectra at high power densities becomes smaller at higher microwave frequencies.

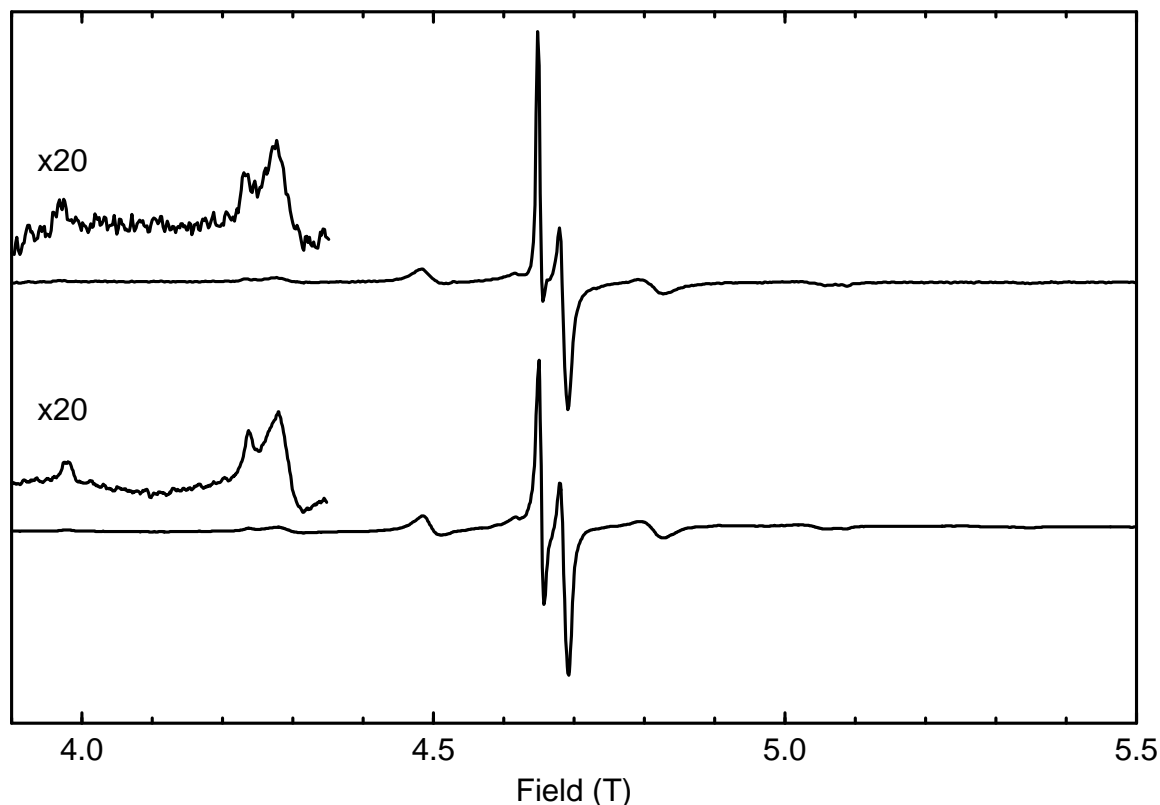


**Figure 2.3:** 130.0 GHz spectra of  $\text{Fe}^{3+}$  in  $\alpha\text{-Al}_2\text{O}_3$ , measured in the non-resonant single-mode setup at 100 K (top), and in the resonant single-mode setup at room temperature (bottom).

In this case, it means that it is nearly impossible to measure a derivative spectrum (as shown in Figure 2.2c). The only solution for this problem — if a single-mode resonator has to be used — is to design more sensitive HF-EPR spectrometers.

An alternative approach is shown in the upper trace of Figure 2.2. This is a spectrum of the same HiPIP measured in the non-resonant single-mode setup at 20 K. The loss in sensitivity is compensated by measuring at lower temperatures, which theoretically enhances the sensitivity by a factor of 15, and by using more sample to overcome the effects of the decreased power density. The amount of sample used in this experiment is approximately  $50\ \mu\text{L}$ , which is comparable to the amount used in Q-band experiments.

### Case 2: Fe(III) in $\alpha\text{-Al}_2\text{O}_3$

A different situation is shown in Figure 2.3. The upper trace shows the spectrum of 150 mg of  $\alpha\text{-Al}_2\text{O}_3$  doped with approximately 1 % Fe(III) ( $S=5/2$ ), measured in the non-resonant single-mode setup at 20 K. The lower trace shows  $\approx 0.5$  mg of the

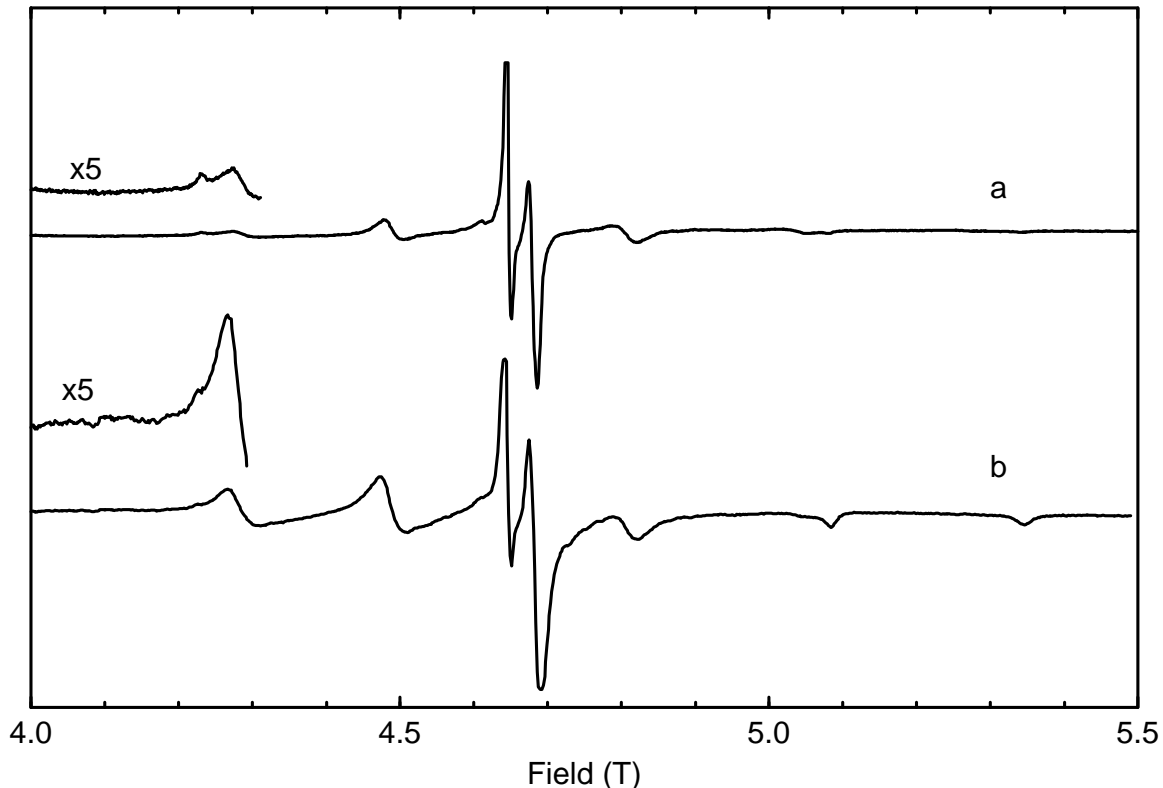


**Figure 2.4:**  $\text{Fe}^{3+}$  in  $\alpha\text{-Al}_2\text{O}_3$ , measured at 130 GHz at 60K (a) and 8 K (b) in the non-resonant single-mode setup. The inset shows the broadening of the  $\frac{3}{2} \leftrightarrow \frac{5}{2}$  transition at lower temperatures.

same sample a resonant single-mode resonator, measured at room temperature. The single-mode setup is clearly superior to the non-resonant single-mode setup here, due to the fact that this sample has a very small  $T_1$ , meaning that the single-mode case does not suffer from saturation effects. For the non-resonant single-mode setup, the gain offered by a favorable Boltzmann distribution and higher filling factor is not compensated by the losses in power density.

In fact, for high spin systems measuring exclusively at low temperatures may result in additional complications, as Figure 2.4 shows. Although the total intensity and S/N increases, lower temperatures also depopulate the upper energy levels, which means that the  $-\frac{5}{2} \leftrightarrow -\frac{3}{2}$  resp.  $\frac{3}{2} \leftrightarrow \frac{5}{2}$  transition (depending on the sign of  $D$ ) will increase in intensity relative to the other transitions. Unfortunately, as can be seen in Figure 2.4, these transitions are also relatively broad, mainly due to ZFS distribution effects. Since the distribution in ZFS parameters for  $\text{Fe}^{3+}$  in  $\alpha\text{-Al}_2\text{O}_3$  is still relatively small (approximately  $0.006 \text{ cm}^{-1}$ ; cf. chapter 3), this effect is still compensated by the increase in S/N due to Boltzmann effects; however, the

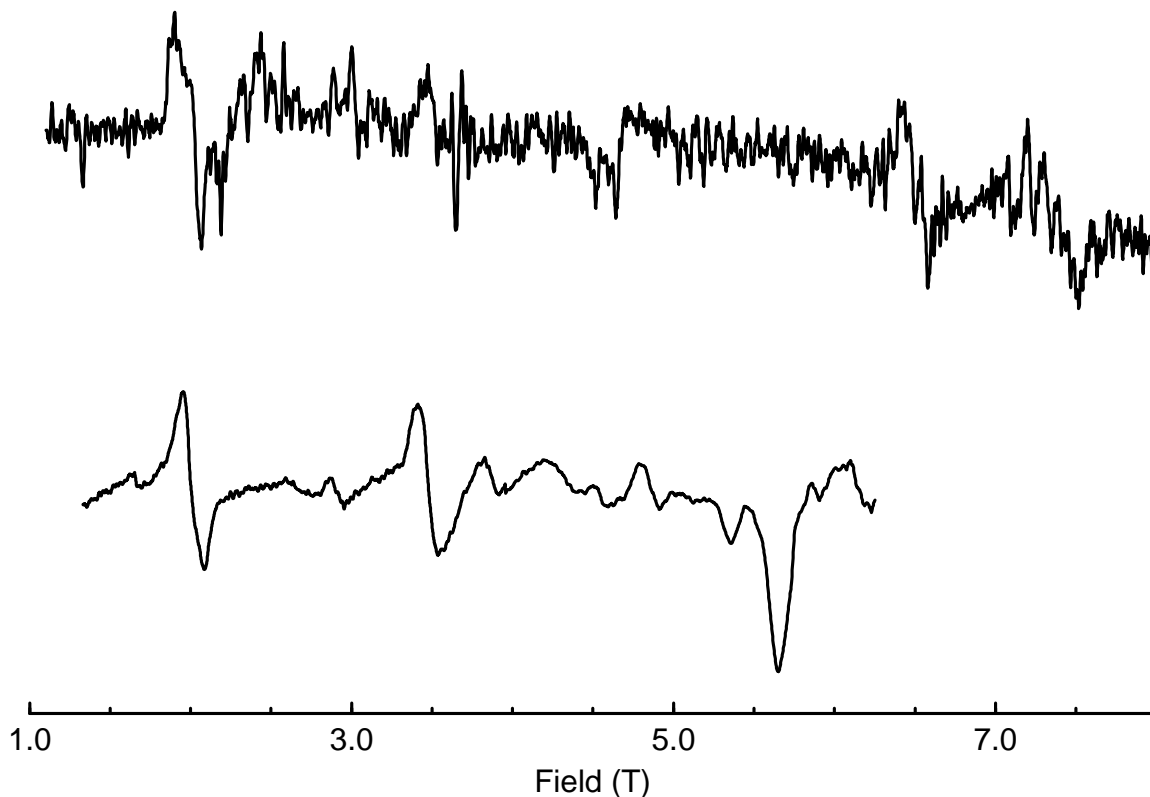


**Figure 2.5:** 130.0 GHz spectra of 10 mM rubredoxin from *Megasphaera elsdenii*, measured in the non-resonant single-mode setup at 100 K (top), and with a resonant single-mode setup at 77 K (bottom).

spectra of samples with large ZFS distributions will probably end up below the detection limit.

### Case 3: Fe(III) in rubredoxin

Some systems are difficult to measure in either resonator type. An example is high spin  $\text{Fe}^{3+}$  in the protein rubredoxin, shown in Figure 2.5. The lower trace shows rubredoxin at 77 K in a single-mode resonator; the upper trace shows the same sample at 100 K in a non-resonant single-mode setup. The resonant single-mode spectrum appears convincing, but this spectrum is a combination of two different scans, and although the general features of this spectrum can be reproduced, it was never possible to establish experimental conditions long enough to allow measurement of all features in a single sweep. It can therefore be concluded that neither of the setups give a spectrum with sufficiently good S/N; this is a sample which is at the limit of detection.

The difficulty in the single-mode case is that the optimum temperature window is



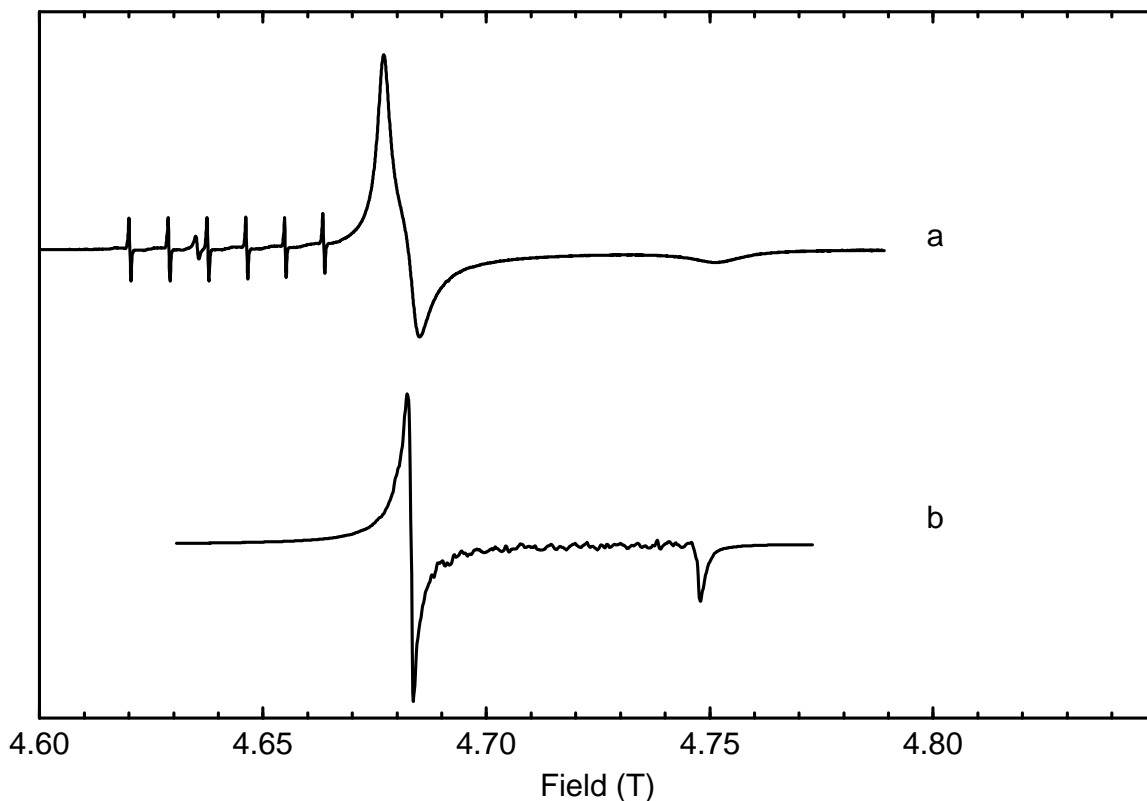


**Figure 2.6:** 130.0 GHz spectra of the  $d^1$ ,  $S = 1/2$  system Cr(V) in  $\text{Li}_3\text{CrO}_8$  measured using a non-resonant setup, (a), and in a single-mode resonator (b).

very small (approximately 5–10K). Another complicating factor is that for this sample, the ZFS is approximately equal to the measuring frequency, which means that the spectrum is spread out over 6 T. Combined with a large linewidth (originating most likely from a distribution in the ZFS parameters), this makes this sample experimentally challenging.

In the non-resonant single-mode setup, the temperature window which allows measurements without saturation is much larger, but in this case S/N suffers from a lack of power density.

#### **Case 4: Cr(V) in $\text{Li}_3\text{CrO}_8$ .**

The systems described above all have relatively broad lines; the sensitivity is limited by the maximum amount of field modulation attainable. Apart from that, these systems were also perfectly disordered. A completely different situation arises when measuring powders, obtained from ground crystals. The amount of grinding required to obtain a ‘perfect’ powder spectrum is proportional to the linewidth of the sample. Oversized resonators can hold more sample, which tends

to average out crystalline artifacts. Single mode resonators only allow a very tiny amount of sample, which requires a very extensive grinding process. This effect becomes even more noticeable when the sample is a pure compound, and has a relatively small linewidth, which is not limited by  $g$ -strain, such as DPPH or the recently suggested  $g$ -marker  $\text{K}_3\text{CrO}_8$ .<sup>1</sup>

Another issue is that since the 130 GHz microwave bridge does not employ automatic frequency control (AFC) (like most other HF-EPR spectrometers), care should be taken that the cavity frequency is not disturbed to much when sweeping the field through the EPR resonance. For pure paramagnetic powders, this means that a very small amount of sample must be used, which stresses the grinding process even more.

A way to tackle this problem is dilution of the sample; either by doping the sample in a suitable host matrix, or by physically diluting the sample with an inert diamagnetic compound like MgO. The former is not always possible, and sometimes also gives a further narrowing of the linewidth. The second option does not change the linewidth, but only prevents an accidental overloading of the cavity.

These problems are illustrated in Figure 2.6b, which shows a 130 GHz EPR spectrum of pure  $\text{Li}_3\text{CrO}_8$ , measured in a single-mode resonator. In this case, it turned out to be impossible to obtain 130 GHz spectra using a single-mode resonator in which the lineshape was not distorted by cavity overloading or powdering artifacts. Similar effects have also been observed for DPPH.<sup>24, 25</sup>

Although the non-resonant single-mode setup does suffer less from powdering artifacts, for pure paramagnets it still has the disadvantage that the cavity loading is rather large, resulting in the experimental signal being a mixture of dispersion and absorption. This can be circumvented by using an oversized non-resonant setup, and increasing the sample volume again.

The spectrum shown in Figure 2.6a is a typical result obtained in this way, after applying the phase correction using the Mn hyperfine lines as described in the experimental section. Especially here it is important to use a known symmetrical EPR signal for the phase correction; other studies have shown that  $\text{Li}_3\text{CrO}_8$  has a large exchange constant ( $J=0.27$  K),<sup>26</sup> which at 130 GHz still affects the lineshape of the powder. This also makes pure  $\text{Li}_3\text{CrO}_8$  (and related compounds) unsuitable as a  $g$ -marker.

## 2.6 Comparison with theory

If the experimental S/N values are compared with the calculated S/N values for each sample/spectrometer combination (both shown in Table 2.3), the following trends can be noted (apart from the fact that the experimental S/N are overestimated by several orders of magnitude, due to the relative large errors in most of

**Table 2.3:** Experimental and theoretical S/N values.

Setup sample	S/N exp			calculated S/N		
	HiPIP	Fe <sup>3+</sup> /Al <sub>2</sub> O <sub>3</sub>	Rb.	HiPIP	Fe <sup>3+</sup> /Al <sub>2</sub> O <sub>3</sub>	Rb.
9 GHz	2700	1800	720	26000	16000	25900
35 GHz	600	4500	3000	13000	6560	6560
130 GHz (single-mode)	18	3600	90	20000	163000	100
130 GHz (non-resonant single-mode)	90	900	18	1290	10000	6
130 GHz (non-resonant) oversized)	—	1200	—	826	6480	4

the parameters):

- HF-EPR should, according to theory, always result in an increase in S/N compared to EPR at conventional frequencies; exceptions are systems with anomalous linewidth broadening at 130 GHz (e.g. rubredoxin). This may be true for samples with a very small linewidth, which also do not suffer from  $g$ -strain; due to various reasons (linewidth broadening, field instability, mechanical noise), in practice, at best a comparable S/N is obtained.
- Single mode resonators should always outperform non-resonant setups, with at least an order of magnitude. Again, this is not in agreement with the experimental spectra, shown in the previous section; for particular samples, the S/N of a non-resonant setup can be better than that of a single-mode setup.
- S/N calculations for high spin systems are not well predicted by theory. This is not really surprising; a good parameterization of these systems is difficult, since equation 2.9 has had no rigorous checking for systems other than  $S = 1/2$ . Also, the linewidth in these systems can vary tremendously with the microwave frequency used.

There are also some general comments on the assumptions underlying equations 2.1–2.9:

- Equation 2.9 assumes only static noise sources, and only focuses on noise of the microwave components. Noise which varies as a function of field or modulation amplitude is not included. Furthermore, only noise in the  $y$ -direction is considered; Field instability, which is noise in the  $x$ -direction, is neglected, and so are mechanical noise sources.

- Values for  $P_w$  have a relatively large error; measurement of microwave power in the cavity is a nontrivial issue. Due to the small size of the 130 GHz microwave components, which need careful alignment to avoid unwanted reflections, measurement of microwave power levels at 130 GHz is also more difficult compared to measurement of 9 GHz power levels.
- It should be noted that equation 2.9 is only valid for modulation amplitudes smaller than the linewidth; according to this equation, overmodulation will result in a better S/N, which is not realistic. As can be seen from Table 2.1 and 2.2, in practice, this is not an issue, since the linewidths are usually much larger than the maximum modulation amplitude.
- Finally, sensitivity (the number of spins per Gauss at a S/N level of 1) is a number which is often determined using a well-defined sample (such as  $\text{Mn}^{2+}$  in MgO, or DPPH) which has relatively narrow, non-saturable lines at room temperature. This number has little correlation with the sensitivity at the conditions which are needed to measure bioinorganic samples, such as the HiPIP (case 1) or Fe(III) in rubredoxin (case 3) discussed in the previous section. These samples require low temperatures (4-30K) to show an EPR signal, and are characterized by relatively broad, easily saturable lines. Measurements under cryogenic conditions suffer from additional noise sources not present at room temperature (temperature instability, vibrations from the cooling system, etc).

From Table 2.3 and the comments given above, it can be concluded that determination of spectrometer parameters is only useful to gain some qualitative insight in the spectrometers operation, but it offers little possibility to calculate (or compare) S/N values for different spectrometers.

## 2.7 Prospects for very high frequency EPR

EPR at THz frequencies is a real possibility, as was already shown by Moll et al.<sup>27</sup> and Hasan et al.<sup>28</sup> It can be expected that the issues described in this paper will also be relevant at higher frequencies. Given the relatively high output power of far-infrared lasers, S/N will most likely be limited by the maximum amount of modulation amplitude attainable, if a traditional homodyne detection scheme using field modulation is employed. The Lorenz force, and microphonics, scales linearly with  $B_0$ ; samples for which the linewidth is determined by  $g$ -strain require a quadratic increase in field modulation amplitude to maintain the same signal intensity. Samples with distributions in ZFS parameters  $D$  and  $E$  also require high modulation amplitudes to compensate for the increase in linewidth, although this

linewidth should be constant in field when  $h\nu$  is much larger than the zero field splitting.

The systems described above are all examples in which the conventional field modulation based detection system used does not improve S/N at higher frequencies, but instead deteriorates S/N. At these frequencies, it might be useful to look at other detection schemes, such as heterodyne detection,<sup>29</sup> temperature modulation,<sup>30</sup> or direct detection of the absorbed microwave radiation using a bolometer.<sup>31, 32</sup>

## 2.8 Conclusion

The ideal HF-EPR setup should be flexible enough to allow differently sized resonators to be used, from single-mode to non-resonant, to match the sample's dielectric losses *and* the relaxation behavior of the sample. This also means that compromises have to be made; for easily saturable samples, some of the additional sensitivity offered by single-mode resonators may have to be traded in for the advantages offered by the lower power density of non-resonant setup. The work described in this paper also shows that fully quasi-optical techniques can also be used at 130 GHz.

## Acknowledgments:

We thank Dr. T. E. Meyer, University of Arizona, for providing the HiPIP sample.

# Bibliography

- [1] B. Cage, A.K. Hassan, L. Pardi, J. Krzystek, L.-C. Brunel, and N.S. Dalal, *J. Mag. Res.*, **1997**, 124, 495.
- [2] W.B. Lynch, K.A. Earle, and J.H. Freed, *Rev. Sci. Instrum.*, **1988**, 59, 1345.
- [3] T. Nakamura, T. Matsuzawa, C.C. Rowlands, V. Beltrán-López, G.M. Smith, and P.C. Riedi, *J. Chem. Soc. Faraday Trans*, **1998**, 94, 3009.
- [4] K.A. Earle, D.E. Budil, and J.H. Freed, *J. Phys. Chem.*, **1993**, 50, 13289.
- [5] B.J. Gaffney, B.C. Maguire, R.T. Weber, and G.G. Maresch, *Appl. Magn. Reson.*, **1999**, 207, 16.
- [6] P.J. van Dam, A.A.K. Klaassen, E.J. Reijerse, and W.R. Hagen, *J. Mag. Res.*, **1998**, 130, 140.
- [7] M.J. Knapp, J. Krzystek, L.-C. Brunel, and D.N. Hendrickson, *Inorg. Chem.*, **2000**, 39, 281.
- [8] J. Telser, L.A. Pardi, J. Krzystek, and L.-C. Brunel, *Inorg. Chem.*, **2000**, 37, 5769.
- [9] D.P. Goldberg, J. Telser, J. Krzystek, A.G. Montalban, L.-C. Brunel, A.G.M. Barrett, and B.M. Hoffman, *J. Am. Chem. Soc.*, **1997**, 119, 8722.
- [10] C.P. Poole. *Electron Spin Resonance*. J. Wiley, New York, 1967.
- [11] W.R. Hagen, *Advanced EPR; Applications in biology and biochemistry*, (Elsevier, Amsterdam), p. 785–812, 1989.
- [12] C. Mailer and C.P.S Taylor, *Biochim. Biophys. Acta*, **1973**, 322, 195.
- [13] K.A. Earle and J.H. Freed, *Appl. Magn. Reson.*, **1999**, 16, 247.
- [14] J.T. Cardin, S.V. Kolaczowski, J.R. Anderson, and D.E. Budil, *Appl. Magn. Reson.*, **1999**, 16, 273.
- [15] Y.S. Lebedev, *Modern pulsed and continuous-wave electron spin resonance*, (Wiley-Interscience, New York), p. 121ff, 1990.
- [16] D. Schmallbein, G.G. Maresch, A. Kamlowski, and P. Höfer, *Appl. Magn. Reson.*, **1999**, 16, 185.
- [17] O. Burghaus, M. Rohrer, T. Götzinger, M. Plato, and K. Möbius, *Meas. Sci. Technol.*, **1992**, 3, 765.

- 
- [18] P.J. van Dam. *Multi-Frequency EPR studies on biological systems*. PhD thesis, University of Nijmegen, The Netherlands, 1998.
- [19] E.J. Reijerse, P.J. van Dam, A.A.K. Klaassen, W.R. Hagen, P.J.M. van Bentum, and G.M. Smith, *Appl. Magn. Reson.*, **1998**, *14*, 153.
- [20] E. van der Horst. PhD thesis, University of Nijmegen, The Netherlands, in preparation.
- [21] J.A. Weil, J.R. Bolton, and J.E. Wertz. *Electron Paramagnetic Resonance: elementary theory and practical applications*. Wiley-Interscience, New York, 1994.
- [22] R. Orbach and H.J. Stapleton, *Electron Paramagnetic Resonance*, (Plenum Press, New York), p. 121ff, 1972.
- [23] K.W.H. Stevens, *Rep. Prog. Phys.*, **1975**, *30*, 189.
- [24] J. Krzystek, A. Sienkiewicz, L. Pardi, and L.C. Brunel, *J. Mag. Res.*, **1997**, *125*, 207.
- [25] S.V. Kolaczowski, J.T. Cardin, and D.E. Budil, *Appl. Magn. Reson.*, **1999**, *16*, 293.
- [26] B. Cage, K. Singh, S. Friedberg, S. Shimizu, J.S. Moodera, W.N. Lawless, and N.S. Dalal, *Solid State Comm.*, **2000**, *113*, 93.
- [27] H.P. Moll, J. van Tol, P. Wyder, M.S. Tagirov, and D.A. Tayurskii, *Phys. Rev. Lett.*, **1996**, *77*, 3459.
- [28] A.K. Hassan, L.A. Pardi, J. Krzystek, A. Sieniewicz, P. Goy, M. Rohrer, and L.-C. Brunel, *J. Mag. Res.*, **2000**, *142*, 300.
- [29] M. Boonman. *Millimeter wave spectroscopy in high magnetic fields*. PhD thesis, University of Nijmegen, The Netherlands, 1998.
- [30] G. Feher, *Rev. Sci. Instrum.*, **1969**, *40*, 1640.
- [31] Y. Alpert, Y. Couder, J. Tuchendler, and H. Thome, *Biochim. Biophys. Acta*, **1973**, *322*, 34.
- [32] G.C. Brackett, P.L. Richards, and W.S. Caughey, *J. Chem. Phys.*, **1971**, *54*, 4383.

## Chapter 3

# Multi frequency analysis of high spin powder EPR spectra of Cr(III), Fe(III) and Gd(III) doped $\alpha$ -alumina

### 3.1 Introduction

Paramagnetic high spin metal centers are of considerable interest in inorganic and bio-inorganic chemistry. EPR spectroscopy of these systems ideally reveals their magnetic spin interactions which in turn reflect the electronic structure of the metal complex. The basic spin Hamiltonian which is generally used to describe EPR spectra of high spin ( $S \geq 3/2$ ) systems is given by:

$$\mathcal{H} = \beta\mathbf{H} \cdot \mathbf{g} \cdot \mathbf{S} + \mathbf{S} \cdot \mathbf{D} \cdot \mathbf{S} = \beta\mathbf{H} \cdot \mathbf{g} \cdot \mathbf{S} + D(S_z^2 - \frac{1}{3}S(S+1)) + E(S_x^2 - S_y^2)$$

Here, the first term corresponds to the Zeeman interaction, and the second term represents the zero field interaction. The analysis of these systems in terms of the spin Hamiltonian parameters is however frequently hampered by experimental and theoretical difficulties. Ideally, the zero field splitting (ZFS) should be much smaller than the Zeeman interaction, which depends on the microwave frequency of the EPR spectrometer. In this situation the ZFS can be directly determined as a perturbation (splitting) on the regular Zeeman EPR spectrum. Unfortunately, most high spin systems have a ZFS in the order of  $0.1\text{--}10\text{ cm}^{-1}$ , which means that at conventional EPR frequencies (9.5 GHz, or  $h\nu \approx 0.3\text{ cm}^{-1}$ ) the ZFS will not be accessible in a simple manner. When the ZFS is much larger than  $h\nu$ , the size of the ZFS can only be determined indirectly from the temperature dependence of the intensity of the EPR transitions, with a relatively large error.<sup>1,2</sup> The only information



that can be extracted from a single spectrum is an estimate of the rhombicity of the D-tensor. High spin systems with a ZFS approximately equal to  $h\nu$  suffer from another problem: extraction of the spin Hamiltonian parameters is theoretically possible, but often nontrivial due to the complexity of the spectra.

With High Frequency EPR (HF-EPR) spectrometers becoming relatively common these days, one would expect that an appreciable number of high spin systems will now satisfy the condition  $D \ll h\nu$ . The aim of the present study is to investigate to what extent HF-EPR can be employed in the study of high spin systems that are problematic at X-band frequencies. We have measured and analyzed a number of well-defined high spin systems with known ZFS parameters (Cr(III),<sup>3-5</sup> Fe(III)<sup>6,7</sup> and Gd(III)<sup>8</sup> in  $\alpha$ -Al<sub>2</sub>O<sub>3</sub>,  $S=(3/2)$ ,  $(5/2)$  and  $(7/2)$  respectively) over a wide range of frequencies, starting at frequencies equal to the ZFS ( $h\nu \approx 0.1 \text{ cm}^{-1}$ ), up to frequencies well above the ZFS ( $h\nu \approx 10 \text{ cm}^{-1}$ ). An additional advantage of using doped  $\alpha$ -Al<sub>2</sub>O<sub>3</sub> as a model compound is that the structure of  $\alpha$ -Al<sub>2</sub>O<sub>3</sub> is well-defined and highly ordered (micro-crystalline), which strictly defines the spin Hamiltonian parameters. This results in relatively small linewidths, which combined with relatively high doping levels of 0.1-0.5% makes spectra of these systems relatively easy to measure.

## 3.2 Experimental

Alumina samples doped with approximately 0.1 % Cr, Fe, and Gd were prepared using sol-gel synthesis according to literature methods.<sup>9,10</sup> The xerogels formed using this procedure were heated at 1100°C for 12 h. X-ray diffraction at room temperature using a Philips PW 1820 X-ray powder diffractometer identified the powders as pure  $\alpha$ -Al<sub>2</sub>O<sub>3</sub>. The 4 GHz EPR spectrum of Fe<sup>3+</sup> in  $\alpha$ -Al<sub>2</sub>O<sub>3</sub> was measured on a S-band spectrometer, described elsewhere.<sup>11</sup> 9 GHz spectra were measured on a Bruker ER-220 spectrometer. 35 GHz spectra were measured on a homebuilt spectrometer, using a Varian E-110 Q-band bridge. 130 GHz room temperature spectra were measured in a Bitter magnet using the setup described by van Dam.<sup>12</sup> 190, 285 and 380 GHz spectra were measured in a superconducting magnet using a Millimeter Vector Network Analyzer (MVNA) from AB Millimetre (75005 Paris, France) as microwave source and detector.<sup>13,14</sup> Although this setup measures both absorption and dispersion simultaneously, here only the absorption trace is shown. Due to the cold bore design of the superconducting magnet used in this setup, spectra were measured at 60–80 K, instead of at room temperature. This may result in small deviations of the ZFS parameters and small lineshape distortions; in practice, these effects are within experimental error.

Simulations of the high spin spectra were computed using a program based on the method described by Morin *et al.*<sup>7</sup> This program calculates EPR spectra by doing a numerical diagonalization of the spin Hamiltonian, which includes second-

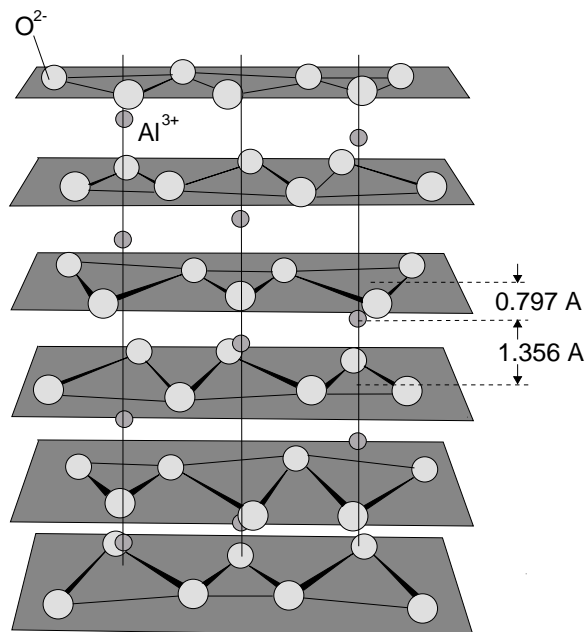


**Figure 3.1:** Structure of  $\alpha$ - $\text{Al}_2\text{O}_3$ , after Geschwind et. al.<sup>8</sup>

and fourth-order ZFS terms. Distributions in ZFS parameters were analyzed by first creating a spectral library in which the ZFS parameters of interest are varied monotonically, and creating the distribution spectrum by summing the individual spectra using a Gaussian distribution shape function. This program is described in more detail in Chapter 4.

### 3.3 Results and discussion

$\alpha$ - $\text{Al}_2\text{O}_3$  is made up of irregular octahedra piled along a  $C_3$  symmetry axis (see Figure 3.1). The aluminum atoms are found between the oxygen octahedra, with the center of each third octahedron left unoccupied. Electrostatic interactions displace the aluminum atoms from the center position between the oxygen octahedra, so that the aluminum cations are closer to neighboring vacancies, which in turn causes the unoccupied oxygen triangles to expand. This results in two differently sized oxygen triangles, as can be seen in Figure 3.1 by comparing the sizes of the triangles in a single plane. Cr, Fe and Gd all substitute for Al, but due to their different size and charge distribution, they do not occupy exactly the same position as the Al ion.

High spin systems with trigonal symmetry can be described with the spin Hamiltonian

$$\mathcal{H} = \beta \mathbf{H} \cdot \mathbf{g} \cdot \mathbf{S} + \sum_{k=2,4,6} \sum_{q=-k}^{q=k} B_k^q \mathbf{O}_k^q$$

where  $B_k^q$  are the fine-structure constants and  $\mathbf{O}_k^q$  are the normalized Stevens operators. These are related to the traditional ZFS parameters  $D$  and  $E$  by the following relations:<sup>15</sup>

$$\begin{aligned} D &= 3B_2^0 = b_2^0 & E &= B_2^2 = b_2^2/3 \\ a &= 24B_4^4 = 2b_4^4/5 & F &= 36(5B_4^0 - B_4^4) = 3(b_4^0 - b_4^4/5) \end{aligned}$$

For readability, we will use the ZFS parameters  $D$  and  $E$  (instead of  $b_2^0$  or  $B_2^0$ ) in the discussion below.

### 3.3.1 Cr(III) (S=3/2) in $\alpha$ -Al<sub>2</sub>O<sub>3</sub>

EPR spectra of Cr<sup>3+</sup> (S=3/2) in  $\alpha$ -Al<sub>2</sub>O<sub>3</sub> are shown in Figure 3.2. The best resolved EPR spectra are obtained at 35 and 130 GHz. They are characterized by a strong central line originating from the  $\frac{1}{2} \leftrightarrow -\frac{1}{2}$  transition and two sets of satellite lines at the positions of the  $\perp$  and  $\parallel$  turning points of the  $\pm\frac{3}{2} \leftrightarrow \pm\frac{1}{2}$  transitions. Figure 3.2 also shows that the relative intensity of the outer peaks compared to the central peak strongly decrease in intensity when going to a frequency far above the ZFS (i.e. 130 GHz in our case). As Figure 3.3 shows, the distance between the center of the central peaks and the satellite lines gives a direct estimate of  $D$ . This perturbation analysis will be discussed in more detail below. If the satellite lines are lost due to insufficient sensitivity, as might be the case at high millimeter wave frequencies, the only information that can be obtained from HF-EPR spectra is the  $g$ -value, which is precision limited by the linewidth and/or field accuracy. This indicates that in some cases, going to higher frequency may result in a *loss* of information.

Apart from the above described difference in intensity, the linewidths of the two spectra are comparable, which means that the linewidth  $\Lambda$  is completely determined by a distribution in the ZFS parameters, or ‘ $D$ -strain’.

Since the 35 GHz spectrum has the best combination of resolution and sensitivity, this spectrum was chosen as a starting point for the simulations. As can be seen in Figure 3.3b, a simulation using the literature values  $g_{\parallel}=1.9840$ ,  $g_{\perp}=1.9867$  and  $D=0.1908 \text{ cm}^{-1}$ ,<sup>4,5</sup> shows that all peak positions are correct, but that the intensities of the outer transitions (which originate from the  $\pm\frac{3}{2} \leftrightarrow \pm\frac{1}{2}$  transitions) are too high. The most likely cause of this effect is a small distribution in ZFS parameters.

When a small distribution in  $E$  or  $D$  is included (as shown in Figure 3.3c and Figure 3.4b), the outer peaks are widened, and the intensity of the central peak (originating from the  $\frac{1}{2} \leftrightarrow -\frac{1}{2}$  transition) increases relative to the outer peaks. This broadening effect has been noticed by several other authors, mostly for high-spin  $\text{Mn}^{2+}$ .<sup>7, 16-18</sup>

Figure 3.3c and Figure 3.4b also show that distributions in  $E$  respectively  $D$  have different effects. The reason for this difference becomes more clear when we look at the dependence on  $D$  and  $E$  of the individual transitions.

When  $D \ll h\nu$ , the resonance position of the  $\frac{1}{2} \leftrightarrow -\frac{1}{2}$  transitions are given to second order by<sup>16, 19</sup>

$$g_{x,y}\beta H_{\frac{1}{2} \leftrightarrow \frac{1}{2}(x,y)} = h\nu - \frac{3(D \pm E)^2}{4\omega_0} \quad (3.1)$$

$$g_z\beta H_{\frac{1}{2} \leftrightarrow \frac{1}{2}(z)} = h\nu - \frac{3E^2}{\omega_0} \quad (3.2)$$

$$g_{45^\circ}\beta H_{\frac{1}{2} \leftrightarrow \frac{1}{2}(45^\circ)} = h\nu + \frac{3(D \pm E)^2}{2\omega_0} - \frac{3(D \pm 3E)^2}{16\omega_0} \quad (3.3)$$

whereas the resonance positions of the  $\pm\frac{3}{2} \leftrightarrow \pm\frac{1}{2}$  transitions are given (to first order) by:

$$g_{\perp}\beta H_{\frac{3}{2} \leftrightarrow \frac{1}{2}(z)} = h\nu + 2D \quad (3.4)$$

$$g_{\parallel}\beta H_{\frac{3}{2} \leftrightarrow \frac{1}{2}(x,y)} = h\nu + D - 3/2E \quad (3.5)$$

$$g_{\parallel}\beta H_{-\frac{1}{2} \leftrightarrow -\frac{3}{2}(x,y)} = h\nu - D + 3/2E \quad (3.6)$$

$$g_{\perp}\beta H_{\frac{3}{2} \leftrightarrow \frac{1}{2}(z)} = h\nu - 2D \quad (3.7)$$

In the above equations, x,y and z represent the orientation of the field with respect to the ZFS tensor axes. For the  $\frac{1}{2} \leftrightarrow -\frac{1}{2}$  transition, a small correction resulting from second order contributions of the ZFS to the spin Hamiltonian has been included. This effectively splits the  $\frac{1}{2} \leftrightarrow -\frac{1}{2}$  lineshape into three peaks, which result from the  $\theta = 0$  (z),  $\theta = 90$  (x,y) and  $\theta = 41.8^\circ$  turning point. This splitting is commonly referred to as the 'second order splitting'. For simplicity, the position of the turning point at  $41.8^\circ$  in equation 3.3 has been calculated using  $\theta=45^\circ$ . At higher microwave frequencies these peaks will merge into an intense central lineshape.

From the above equations it can be seen that the resonance position of the  $\frac{1}{2} \leftrightarrow -\frac{1}{2}$  transition is much less influenced by changes in  $D$  or  $E$  than the other transitions are. Distributions in either  $D$  or  $E$  will thus tend to increase the relative intensity of the central  $\frac{1}{2} \leftrightarrow \frac{1}{2}$  transition. It can also be deduced that distributions in  $D$  will affect both the parallel (z) and perpendicular (xy)  $\frac{3}{2} \leftrightarrow \frac{1}{2}$  transitions, whereas distributions in  $E$  will be visible only in the perpendicular  $\frac{3}{2} \leftrightarrow \frac{1}{2}$  transition.

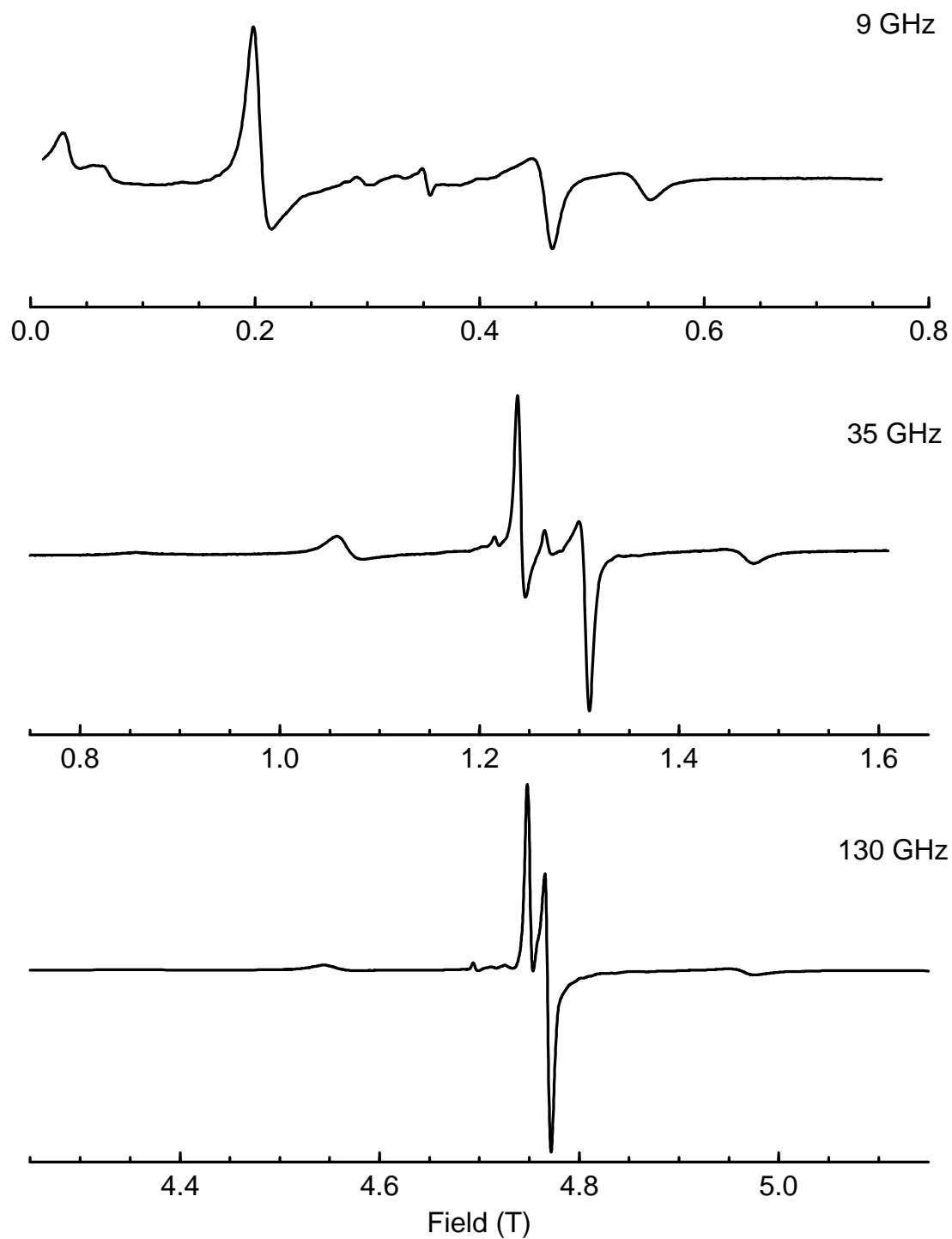


**Figure 3.2:** EPR spectra of  $\text{Cr}^{3+}$  in  $\alpha\text{-Al}_2\text{O}_3$ , measured at 9.79 GHz (top), 35.30 GHz (middle) and 130.00 GHz (bottom).

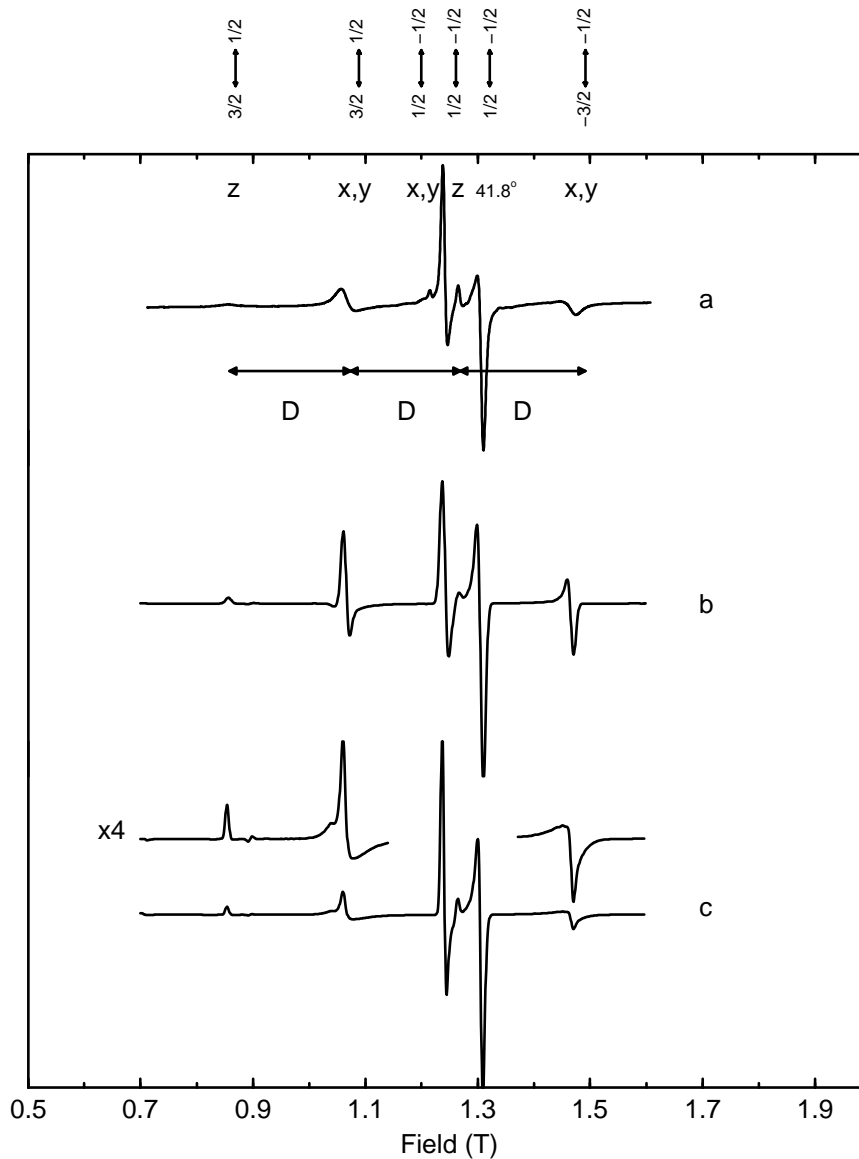


**Figure 3.3:** 35 GHz EPR spectra of  $\text{Cr}^{3+}$  in  $\alpha\text{-Al}_2\text{O}_3$ . At the top of the graph, the origin of the various resonances is shown. The letters  $x,y,z$  represent the orientation of the field with respect to the ZFS tensor axes; around  $g=2$ , the peak marked with '41.8' originates from second order effects.

**a:** Experimental spectrum of  $\text{Cr}^{3+}$  in  $\alpha\text{-Al}_2\text{O}_3$ , measured at 35.2 GHz.

**b:** Calculated spectrum without distribution in ZFS parameters. Simulation parameters:  $g_{\parallel}=1.9840$ ,  $g_{\perp}=1.9867$ ,  $D=0.1908\text{ cm}^{-1}$ ,  $\Gamma=0.01\text{ T}$ . Spin Hamiltonian parameters taken from references 4 and 5

**c:** Calculated spectrum with a Gaussian distribution in  $E$  only. ( $\sigma=0.020\text{ cm}^{-1}$  in  $E$ , using 100 spectra and  $\Gamma=0.005\text{ T}$ .)

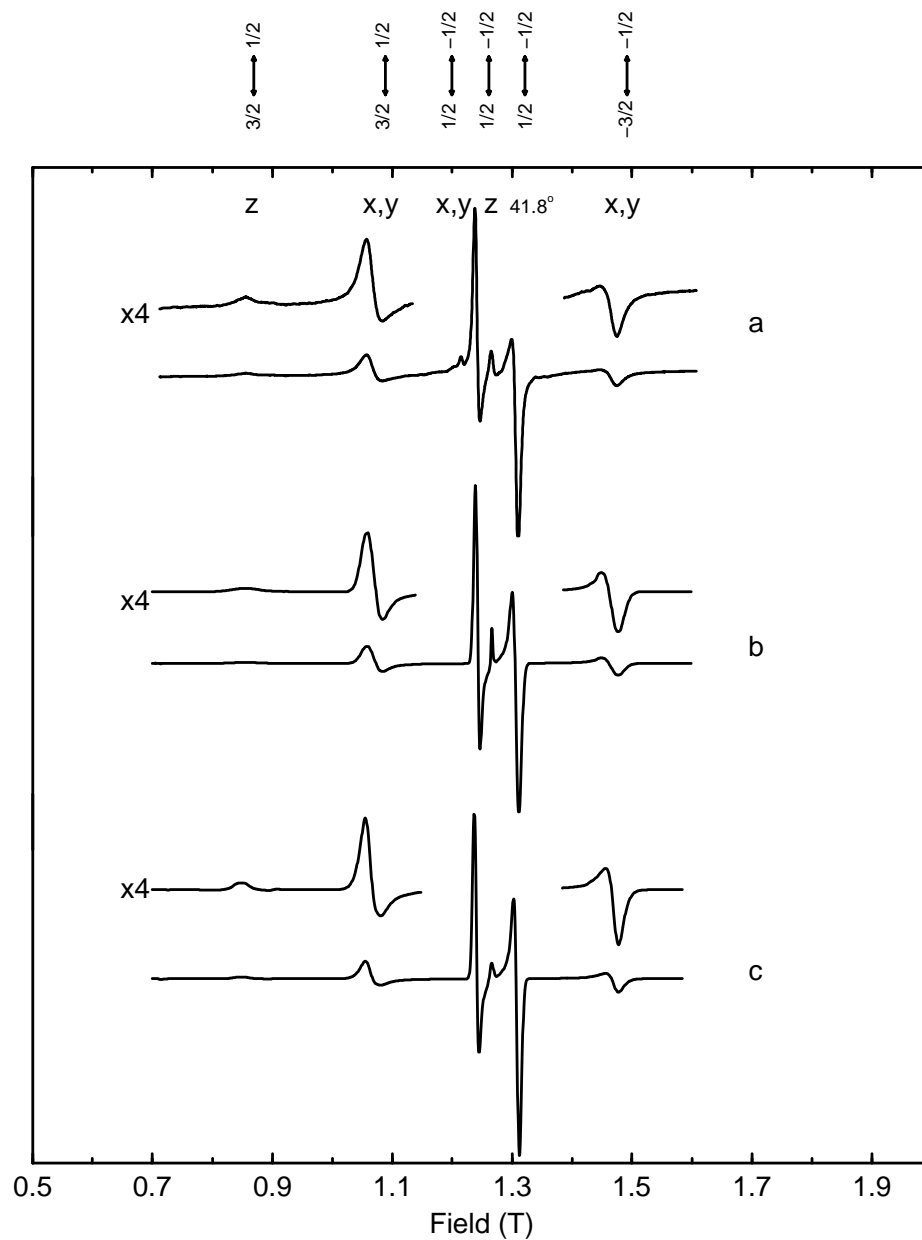


**Figure 3.4:** 35 GHz EPR spectra of  $\text{Cr}^{3+}$  in  $\alpha\text{-Al}_2\text{O}_3$ .

**a:** Experimental spectrum of  $\text{Cr}^{3+}$  in  $\alpha\text{-Al}_2\text{O}_3$ , measured at 35.2 GHz.

**b:** Calculated spectrum with a Gaussian distribution in  $D$  only. ( $\sigma=0.020\text{ cm}^{-1}$  in  $D$ , using 100 spectra and  $\Gamma=0.005\text{ T}$ .)

**c:** Calculated spectrum with a two-dimensional Lorentzian distribution ( $\sigma=0.132\text{ cm}^{-1}$  in  $D$ ,  $\sigma=0.012\text{ cm}^{-1}$  in  $E$ , using  $150\times 150$  spectra and  $\Gamma=0.006\text{ T}$ .)

If the simulations in Figure 3.3c and Figure 3.4b (which show a distribution in  $E$  and  $D$  respectively) are compared to the experimental spectrum, it appears that the experimental spectrum is dominated by a distribution in  $D$ . A distribution in just  $E$  results in a too intense parallel  $\frac{3}{2} \leftrightarrow \frac{1}{2}$  transition, and the lineshape of the perpendicular (xy)  $\frac{3}{2} \leftrightarrow \frac{1}{2}$  transition is also too narrow to match the experimental spectrum. A distribution in  $D$  gives a much better fit, but tends to broaden the parallel  $\frac{3}{2} \leftrightarrow \frac{1}{2}$  transition too much. The too sharply peaked parallel  $\frac{1}{2} \leftrightarrow -\frac{1}{2}$  transition also shows that a small distribution in  $E$  needs to be included, in addition to a relatively large  $D$  distribution.

In Figure 3.4c, the result of calculating a distribution in  $D$  and  $E$  is shown. This gives an almost complete fit; the lineshapes and intensities of the  $\frac{3}{2} \leftrightarrow \frac{1}{2}$  transitions are almost correct. The only features not simulated correctly are the intensities of the parallel  $\frac{1}{2} \leftrightarrow -\frac{1}{2}$  transition, and the  $\theta = 41.8^\circ$  second order turning point. Since both distributions contribute to the linewidth, the distribution sizes of a 2D-distribution are slightly smaller than the distribution sizes found by simulations in which only one parameter is distributed.

It should be noted that this type of simulation is relatively insensitive to the shape of the ZFS distribution used; Gaussian and Lorentzian distributions give similar results.

### 3.3.2 Fe(III) (S=5/2) in $\alpha$ -Al<sub>2</sub>O<sub>3</sub>

In Figures 3.5 to 3.9, multi-frequency EPR spectra of Fe<sup>3+</sup> in  $\alpha$ -Al<sub>2</sub>O<sub>3</sub> are shown in the range 2-380 GHz. From the constant linewidths in Figure 3.7 it can be directly concluded that the linewidth of Fe<sup>3+</sup> in  $\alpha$ -Al<sub>2</sub>O<sub>3</sub> is also limited by  $D$ -strain. Up to 380 GHz, there is no line broadening, which means that  $g$ -strain is either negligible or smaller than 0.0015 (determined from the linewidth of the center peak at 380 GHz). It also means that, for this particular system going to frequencies higher than 130 GHz would appear to yield no additional information.

Using literature values for the spin Hamiltonian parameters,<sup>6,7</sup> matching peak positions can be obtained for all spectra. As shown in Figure 3.5, estimates for  $D$  and  $E$  can be determined —as before— directly from the 130 GHz spectra, although this can be complicated by the higher order terms  $b_4^0$  and  $b_4^3$ .

Just as was the case for Cr<sup>3+</sup> in  $\alpha$ -Al<sub>2</sub>O<sub>3</sub>, a distribution in both  $D$  and  $E$  has to be included to obtain a good fit (see Figure 3.8). Figure 3.9 shows that it is much more difficult to obtain a matching fit for the 9 GHz spectra, as these are much more sensitive to changes in ZFS parameters; unfortunately, from these spectra it is not directly clear how the ZFS parameters are related to the various peaks in the spectrum. Compared to the 9 GHz spectra, analysis of the 130 GHz spectra is



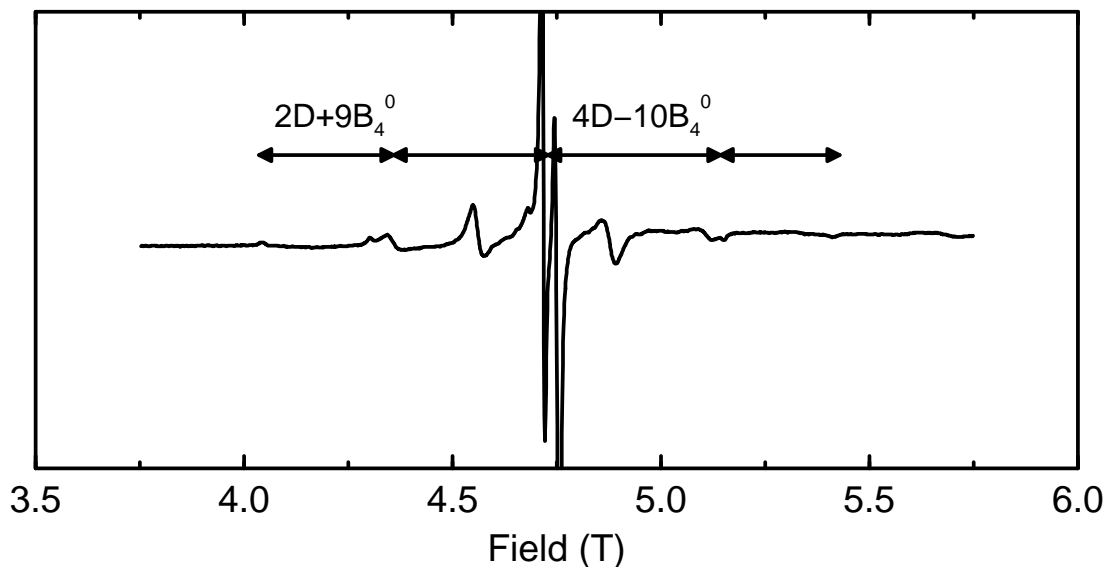


**Figure 3.5:** Experimental spectra of  $\text{Fe}^{3+}$  in  $\alpha\text{-Al}_2\text{O}_3$ , measured at 130 GHz. The arrows show how the various ZFS parameters affect the spectrum.

relatively straightforward.

The use of a distribution in both  $D$  and  $E$  is in slight contrast with the results of Morin<sup>7</sup> for  $\text{Fe}^{3+}$  in  $\alpha\text{-Al}_2\text{O}_3$ , who used a distribution in  $E$  only. It should be noted that in the simulations shown here, the distribution in  $E$  is still two times larger than the distribution in  $D$ ; also, the samples used in this study have a far higher doping level than the samples used by Morin et al. EPR spectra of aluminas with higher doping levels (not shown here) also show an increase in the ZFS distribution sizes.

Surprisingly, using the two dimensional distribution in  $D$  and  $E$  determined from the 130 GHz spectrum to simulate the 9 GHz spectrum gives a poorer fit than using a distribution in  $E$  alone. The effects of a distribution in  $D$  do not affect the overall appearance of the 9 GHz spectrum, but only changes the intensity of the peak at 0.05 T, as shown by Figure 3.9d.

Most likely, the experimental 9 GHz spectrum shows the effects of a distribution in  $D$  and  $E$ , correlated with a distribution in the higher order parameters  $b_4^0$  and  $b_4^3$ . This makes it practically impossible to estimate the size of the latter distributions. Some exploratory research using distributions in the higher order terms has shown that changes in  $b_4^0$  and  $b_4^3$  have relatively little effect on the 130 GHz EPR spectrum; a possible distribution in these parameters is completely masked by the distributions in  $D$  and  $E$ , which is in agreement with the 130 GHz simulations. At 9 GHz, distributions in  $b_4^3$  only affect the so called looping transitions.<sup>7,20</sup> Distributions

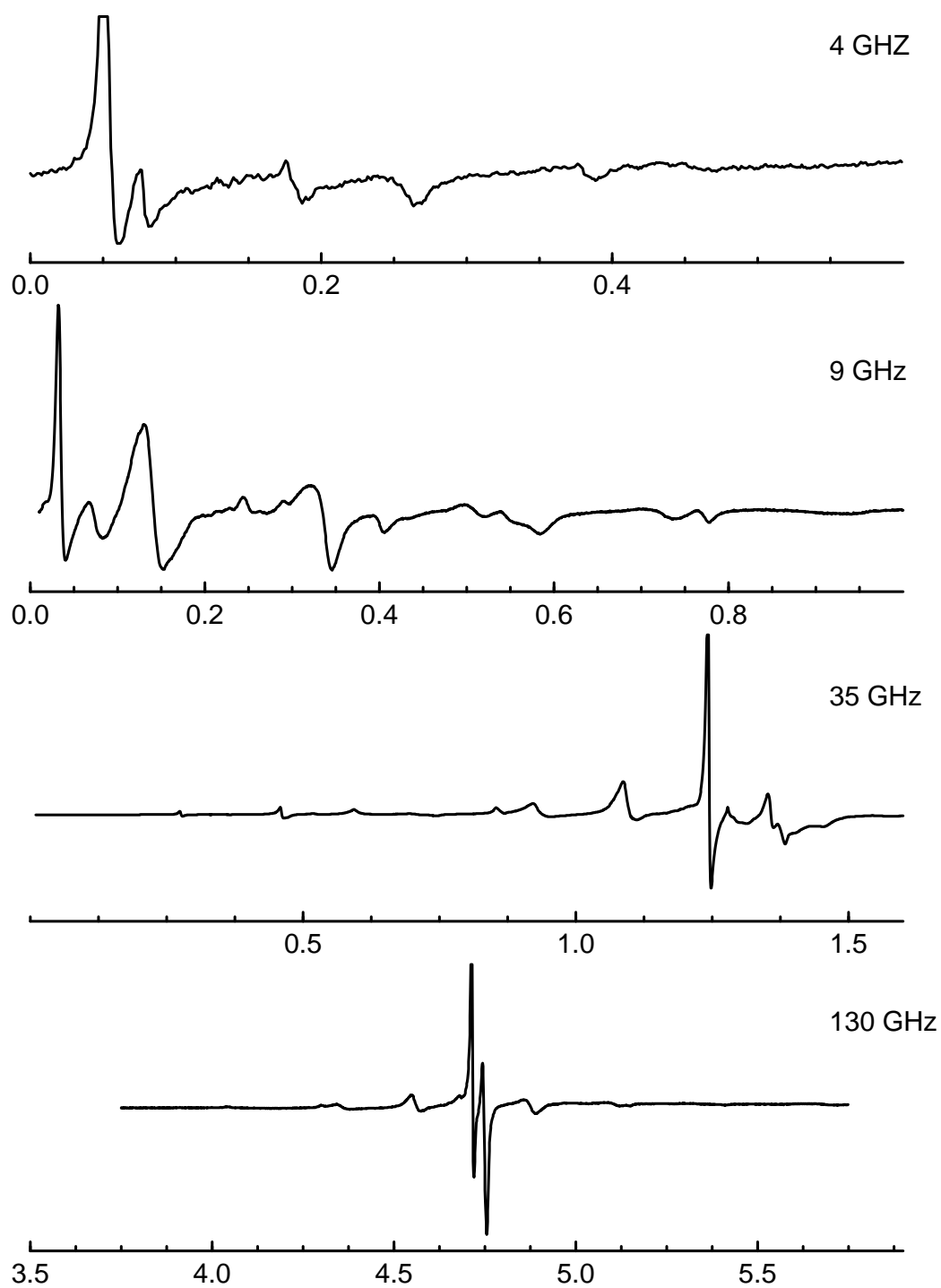


**Figure 3.6:** Experimental spectra of Fe<sup>3+</sup> in  $\alpha$ -Al<sub>2</sub>O<sub>3</sub>, measured at room temperature at 4.02 GHz (a), 9.78 GHz (b), 35.18 GHz (c) and 130.00 GHz (d).

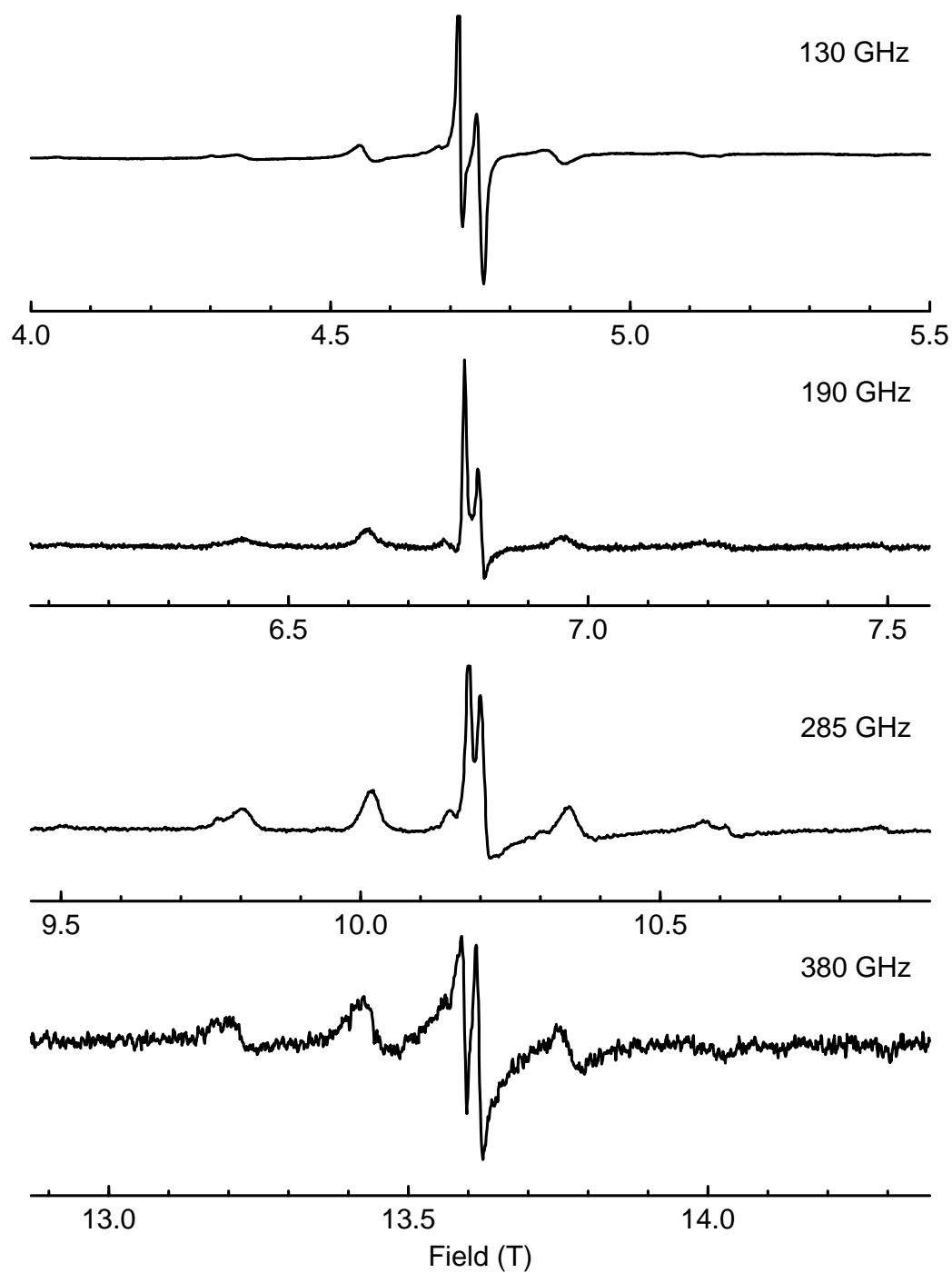


**Figure 3.7:** Experimental spectra of Fe<sup>3+</sup> in  $\alpha$ -Al<sub>2</sub>O<sub>3</sub>, measured at 130.00 GHz (a), 189.960 GHz (b), 284.771 GHz (c) and 380.318 GHz (d). The 190, 285 and 380 GHz spectra were measured at approximately 60 K; the 130 GHz spectrum was measured at room temperature.

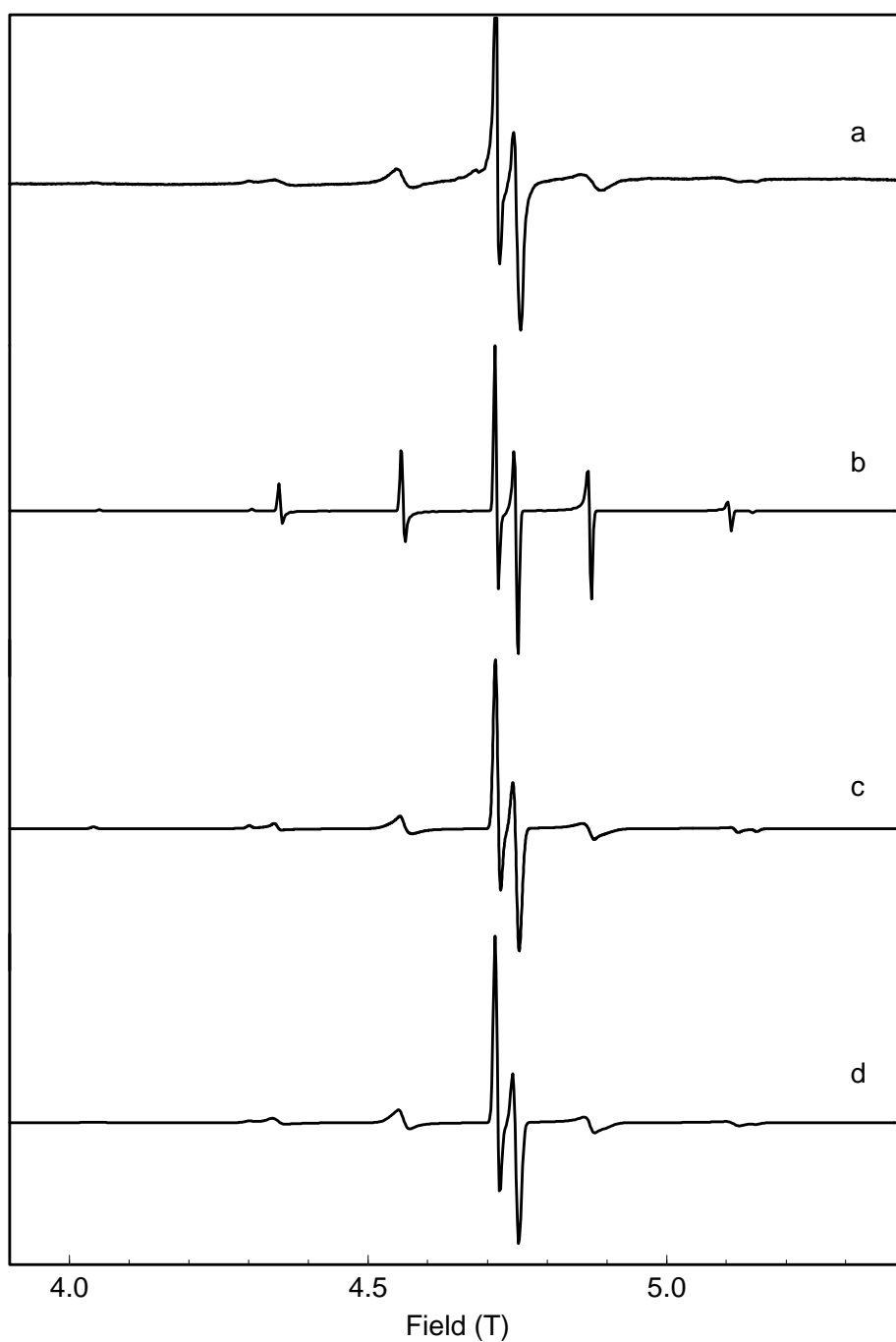


**Figure 3.8:** **a:** Experimental spectrum of  $\text{Fe}^{3+}$  in  $\alpha\text{-Al}_2\text{O}_3$ , measured at 130.00 GHz.  
**b:** Calculated spectrum with no distribution in  $E$ . Simulation parameters:  $g=2.000$ ,  $D=0.1683\text{ cm}^{-1}$ ,  $b_4^0=-0.01098\text{ cm}^{-1}$ ,  $b_4^3=0.2178\text{ cm}^{-1}$ , linewidth ( $\Gamma$ ) 0.02 T; taken from ref. 7.  
**c:** Calculated spectrum with a Gaussian distribution ( $\sigma=0.006\text{ cm}^{-1}$ ) in  $E$ , using 100 spectra and  $\Gamma=0.008\text{ T}$ .  
**d:** Calculated spectrum with a Gaussian distribution in  $D$  ( $\sigma=0.066\text{ cm}^{-1}$ ) and  $E$  ( $\sigma=0.042\text{ cm}^{-1}$ ) using  $150\times 150$  spectra and  $\Gamma=0.007\text{ T}$

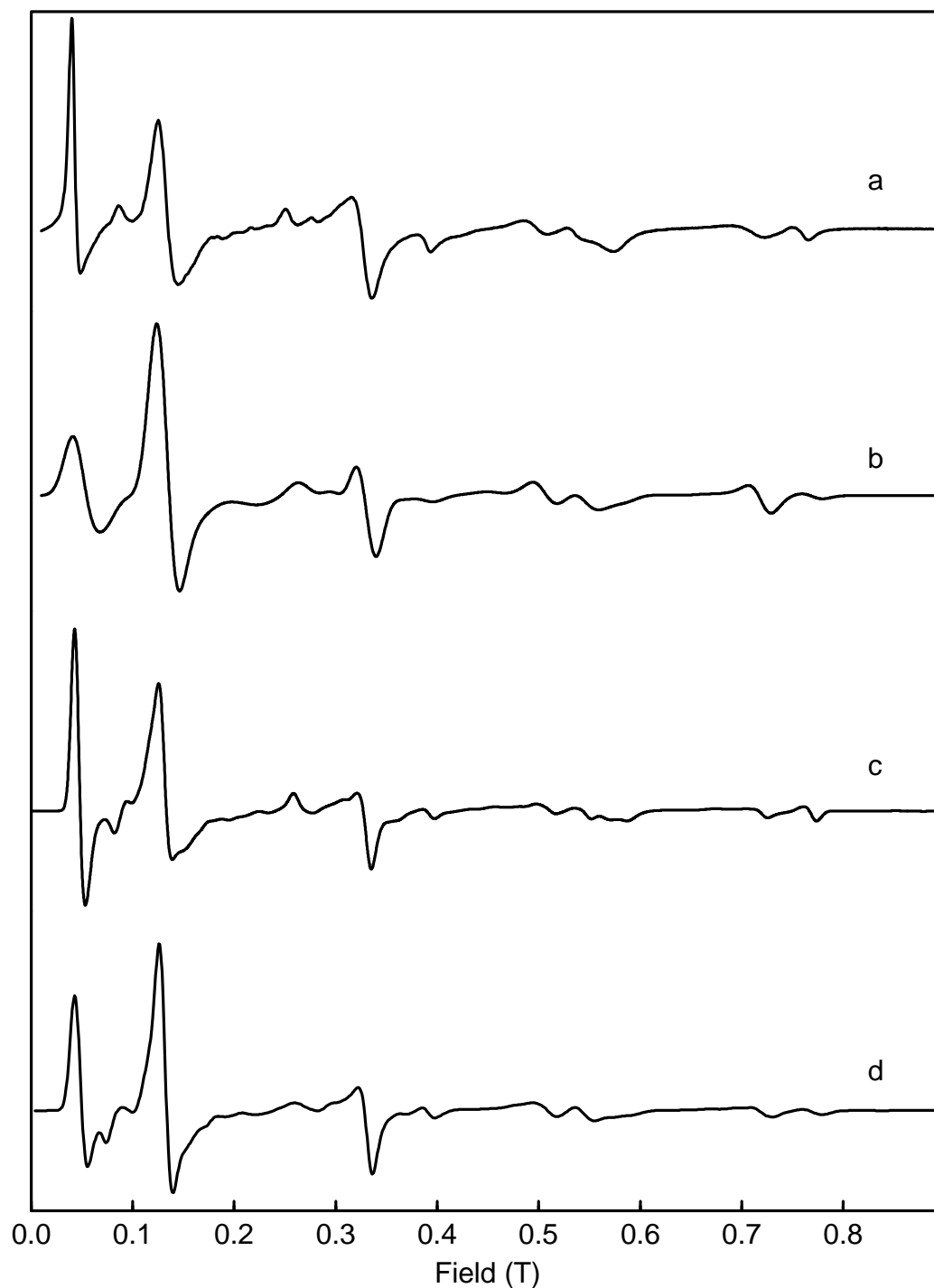


**Figure 3.9:** **a:** Experimental spectrum of  $\text{Fe}^{3+}$  in  $\alpha\text{-Al}_2\text{O}_3$ , measured at 9.78 GHz.

**b:** Calculated spectrum with no distribution in  $E$ . Simulation parameters:  $g=2.000$ ,  $D=0.1683\text{ cm}^{-1}$ ,  $b_4^0=-0.01098\text{ cm}^{-1}$ ,  $b_4^3=0.2178\text{ cm}^{-1}$ ,  $\Gamma=0.02\text{ T}$ .

**c:** Calculated spectrum with a Gaussian distribution ( $\sigma = 0.006\text{ cm}^{-1}$ ) in  $E$ , using 100 spectra and  $\Gamma=0.008\text{ T}$ .

**d:** Calculated spectrum with a Gaussian distribution in  $D$  ( $\sigma=0.066\text{ cm}^{-1}$ ) and  $E$  ( $\sigma=0.042\text{ cm}^{-1}$ ) using  $150 \times 150$  spectra and  $\Gamma=0.007\text{ T}$

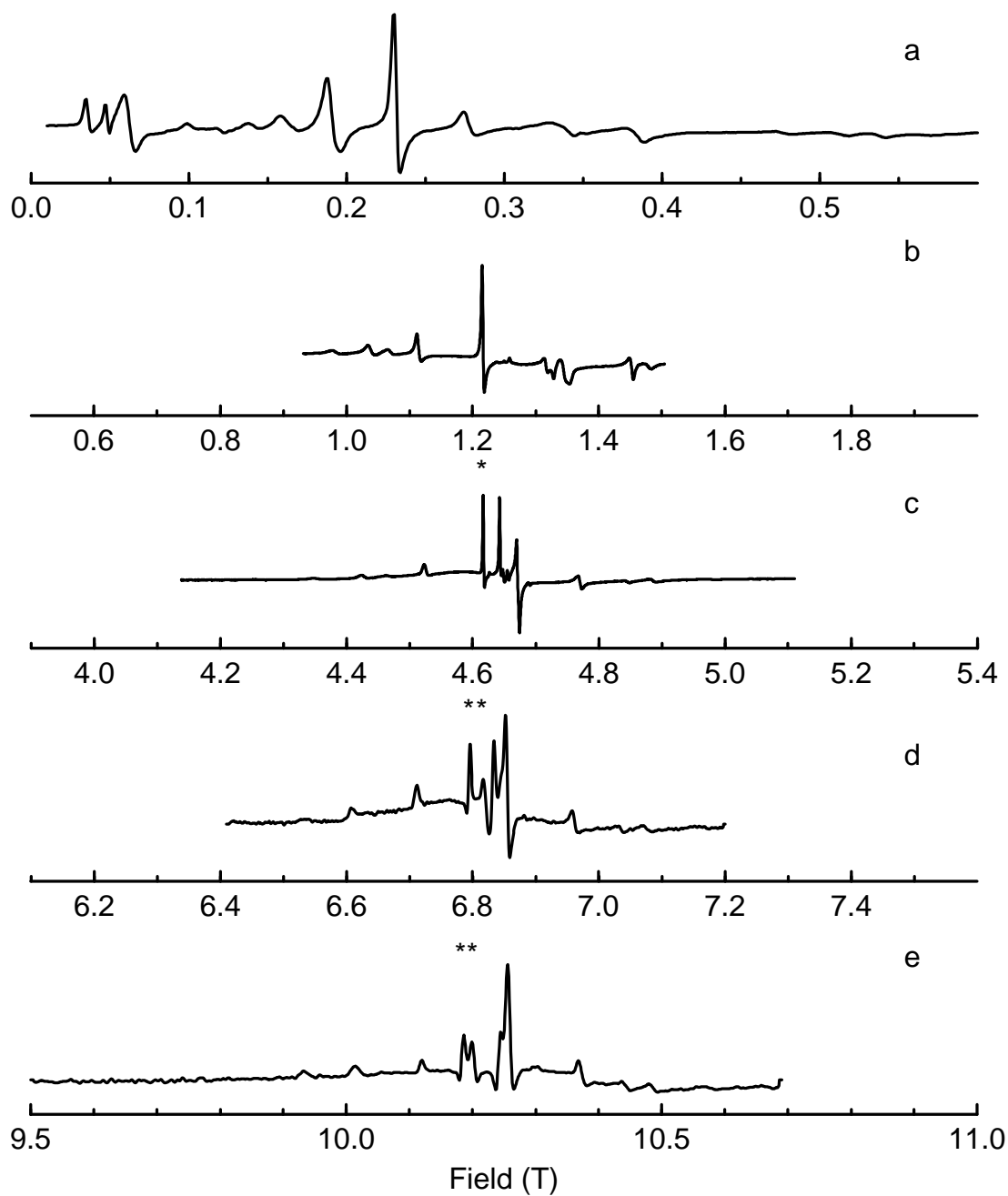


**Figure 3.10:** Experimental spectra of  $\text{Gd}^{3+}$  in  $\alpha\text{-Al}_2\text{O}_3$ , measured at 9.78 GHz (a), 35.275 GHz (b), 130.00 GHz (c), 190.004 GHz (d) and 285.012 GHz (e). The 190 and 285 GHz spectra were measured at  $\approx 70$  K; all other spectra were measured at room temperature. The asterisks in the 130, 190 and 285 GHz spectra indicate peaks originating from a second  $\text{Gd}^{3+}$  species (as described in the text).

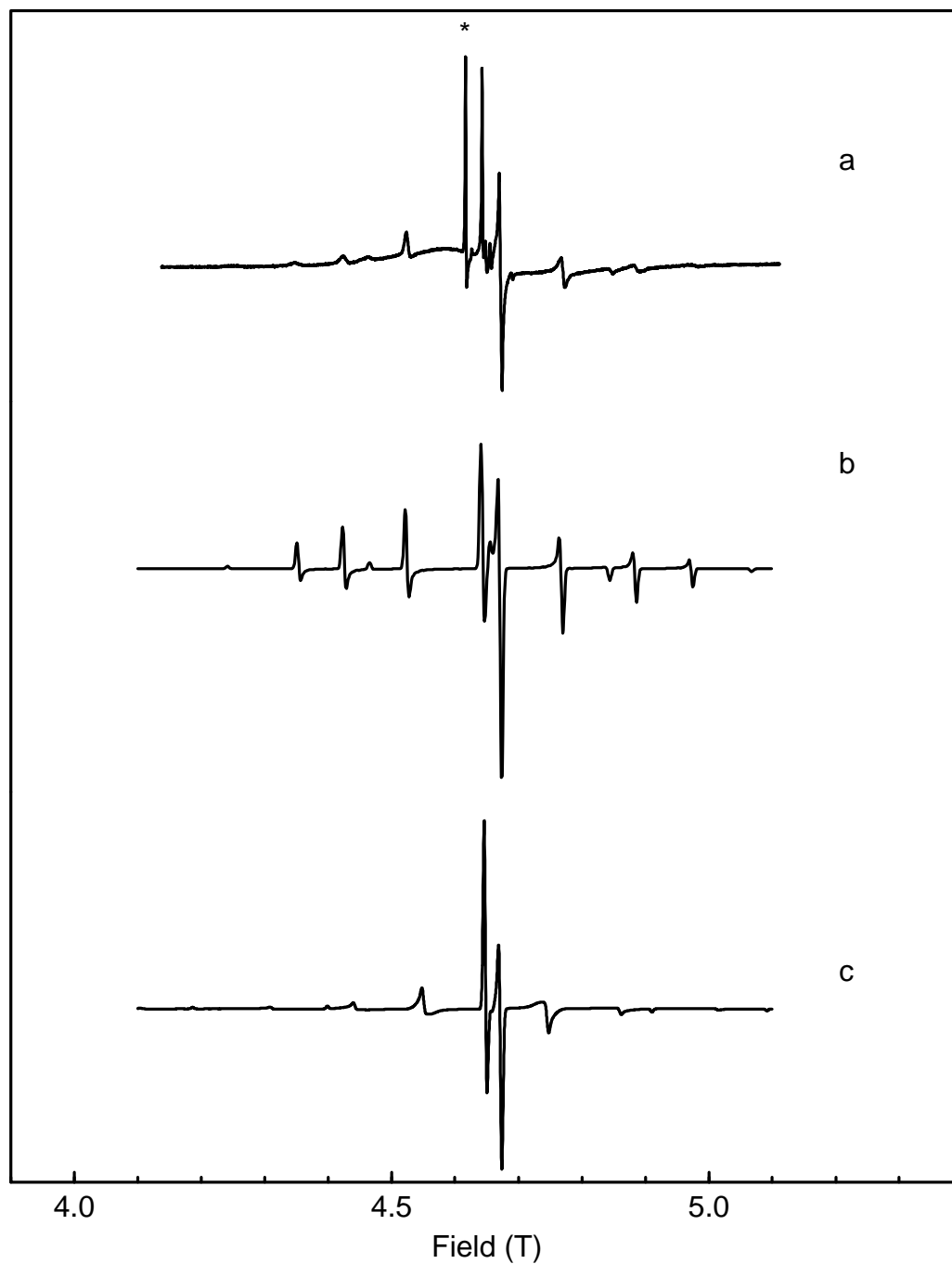


**Figure 3.11:** **a:** Experimental spectrum of  $\text{Gd}^{3+}$  in  $\alpha\text{-Al}_2\text{O}_3$ , measured at 130.00 GHz. The asterisk indicates a peak originating from a second  $\text{Gd}^{3+}$  species (as described in the text).

**b:** Calculated spectrum with no distribution in  $E$ . Simulation parameters:  $g=2.000$ ,  $D=0.30987$   $\text{cm}^{-1}$ ,  $b_4^0=-0.01098$   $\text{cm}^{-1}$ ,  $b_4^3=0.2178$   $\text{cm}^{-1}$ ,  $b_6^0=0.0001$   $\text{cm}^{-1}$ ,  $b_6^6=0.0005$   $\text{cm}^{-1}$ .<sup>8</sup>

**c:** Calculated spectrum with a distribution of  $0.007$   $\text{cm}^{-1}$  in  $E$ .

in  $b_4^0$  affect the whole spectrum. Effects of these distributions are only visible if the distribution sizes are in the order of the value of the higher order parameters themselves.

Although distributions in  $b_4^0$  and  $b_4^3$  are not easily identifiable,  $b_4^0$  and  $b_4^3$  need to be included to obtain good fits at 9 and 35 GHz. Combined with the above discussion, this indicates that for determination of all ZFS parameters, spectra have to be obtained at frequencies well above the ZFS to obtain values for  $D$ ,  $E$ ,  $b_4^0$  and  $g$ , and at frequencies comparable to the ZFS to determine the higher order term  $b_4^3$ . HF EPR therefore does not exclude the need for conventional EPR.

The 130 GHz spectra can be fitted with an isotropic  $g$ -value of 2.00. Within the uncertainty of the field axis calibration, combined with the effects of the ZFS distribution on the lineshape, it is not possible to determine from these spectra whether the  $g$ -values differ more than 0.01 from the free electron value.

### 3.3.3 Gd(III) (S=7/2) in $\alpha$ -Al<sub>2</sub>O<sub>3</sub>

The spectra of Gd<sup>3+</sup> (S=7/2) in  $\alpha$ -Al<sub>2</sub>O<sub>3</sub> (Figure 3.10) were analyzed in a similar way. At first sight, this system appears to show an increase in resolution at frequencies up to 285 GHz, in contrast to the S=5/2 case. As can be seen in Figure 3.11, the 130 GHz EPR spectra contain an additional peak (indicated with an asterisk in Figure 3.11). The 190 and 285 GHz measurements (Figure 3.10) show that this is not an S=1/2 signal, but instead a second S=7/2 species with a relatively large distribution in  $D$ , so that the  $\frac{1}{2} \leftrightarrow -\frac{1}{2}$  transition is the only visible feature of this species. At 9.5 and 35 GHz, this species completely overlaps with the 'normal' spectrum, aside from a distinct baseline drop at  $g=2$ .

Earlier reports in the literature already mentioned that Gd<sup>3+</sup> doped in glassy or ceramic materials has a tendency to be very disordered. X-band EPR spectra of lanthanide compounds often share similar features: an intense peak at  $g \approx 5.9$ , and relatively broad peaks at  $g \approx 2.8$  and  $g \approx 2.0$ . Because this type of spectrum is seen so often for lanthanide compounds, it is also referred to as the 'U-spectrum', after its ubiquity.<sup>18,21</sup> Simulations by Brodbeck<sup>18</sup> and Legein<sup>22,23</sup> have shown that such spectra originate from S=7/2 species with a relatively broad distribution in  $D$  values, and a distribution in  $E/D$  ranging from 0 to 1/3. In our case, it can be inferred from the sharp  $\frac{1}{2} \leftrightarrow -\frac{1}{2}$  transition that the distribution in  $D$  is relatively small, whereas the distribution in  $E$  is covering the whole range of rhombicities. From the large  $E$  distribution, it can be deduced that there is a large amount of disorder present in this system, but the relatively small  $D$  distribution suggests that this disorder has little energetic effects. The second species has a  $g$ -value of 2.01, vs 2.00 for the first species.

At 130 GHz and up, the spectrum of each single species is completely resolved,



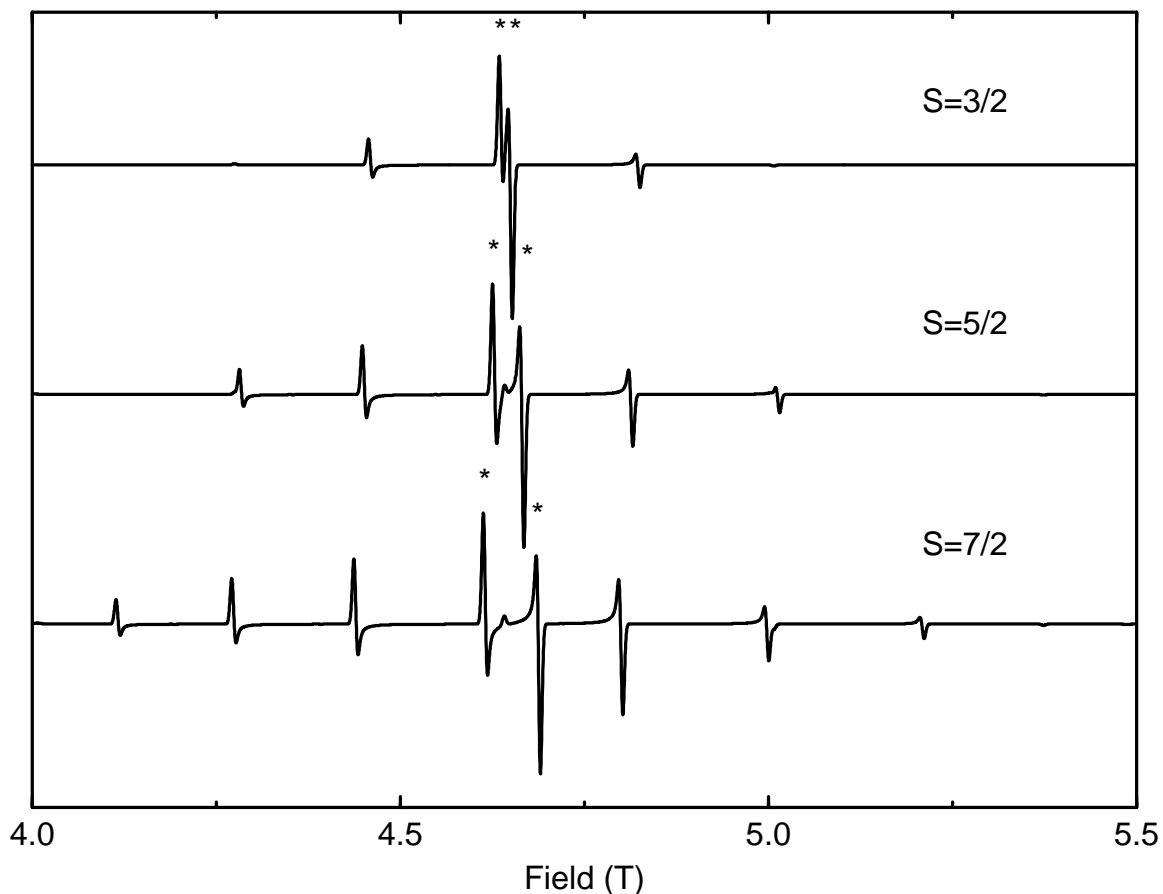


**Figure 3.12:** Simulations of  $S=3/2$ ,  $S=5/2$  and  $S=7/2$  spectra at 130 GHz. All systems were simulated with  $g=2.000$ ,  $D=0.0570 \text{ cm}^{-1}$ ,  $E=0 \text{ cm}^{-1}$ . The peaks of the  $\frac{1}{2} \leftrightarrow -\frac{1}{2}$  transition are indicated by asterisks; the second order splitting is defined as the distance between the two peaks of the  $\frac{1}{2} \leftrightarrow -\frac{1}{2}$  transition. The spectra have been scaled to equal height of the  $\frac{1}{2} \leftrightarrow -\frac{1}{2}$  transition.

but the increase in  $g$ -resolution still simplifies the combined spectrum at higher frequencies. The simulations shown in Figure 3.11 show that also for this species, to obtain reasonably matching spectra, a distribution in  $E$  has to be taken into account.

### 3.3.4 Comparison between different spin states

In figure 3.12 a series of basic simulations (i.e. no distribution effects) for various spin states is presented using a typical value for the ZFS parameter  $D$ . When comparing these spectra as a function of spin state, the following effects are noted: For the higher spin spectra, the intensity of the outer transitions appears to decrease less in intensity as the frequency increases. Closer inspection shows that the

intensity of the  $S=3/2 \frac{3}{2} \leftrightarrow \frac{1}{2}$  transition, relative to the central  $\frac{1}{2} \leftrightarrow -\frac{1}{2}$  transition is equal to the  $S=5/2 \frac{5}{2} \leftrightarrow \frac{3}{2}$ , and  $S=7/2 \frac{7}{2} \leftrightarrow \frac{5}{2}$  transitions. The intensity of the *outermost* transition relative to the central peak is approximately the same for all three species.

Another trend visible in Figure 3.12 is that the second order splitting of the  $\frac{1}{2} \leftrightarrow -\frac{1}{2}$  transition (as described on page 51) increases with increasing spin multiplicity, and that the second order splitting of species with higher multiplicities is still visible at higher frequencies. Expressions for the second order splitting in high field including hyperfine effects, but neglecting higher order terms in the ZFS have been derived by Meirovitch,<sup>16</sup> and are reproduced here without hyperfine interaction:

$$E_{\frac{1}{2},m} - E_{-\frac{1}{2},m} = h\nu = g\beta H - \frac{2B_+B_-G}{g\beta H_0} + \frac{C_+C_-G}{g\beta H_0} \quad (3.8)$$

$$\begin{aligned} B_{\pm} &= \frac{D}{4}(-\sin 2\theta + \eta \sin 2\theta \cos 2\phi \pm i2\eta \sin \theta \cos 2\phi) \\ C_{\pm} &= \frac{D}{4}(\sin^2 \theta + \eta(\cos^2 \theta + 1) \pm i2\eta \cos \theta \sin 2\phi) \\ G &= 4S(S+1) - 3 \\ \eta &= E/D \end{aligned}$$

In the above equation,  $\theta$  and  $\phi$  are the polar and azimuthal angles between the magnetic field and the coordinate system of the ZFS-tensor. As shown by Lynch,<sup>17</sup> the size of the second order splitting is obtained by calculating the resonance fields of the  $\frac{1}{2} \leftrightarrow -\frac{1}{2}$  transition at the turning points of this transition (which are  $\theta = 90^\circ$  and  $\theta = 41.8^\circ$ )<sup>17, 24, 25</sup> As can be seen in Figure 3.13, equation 3.8 gives a good estimate of the second order splitting, for all spin species. Figure 3.13 is also consistent with the experimental findings: for an equal ZFS, the second order splitting increases with spin state.

As was already noticed by Meirovitch<sup>16</sup> and Lynch,<sup>17</sup> equation 3.8 could be used to obtain a good estimate of the zero field splitting, even for systems for which the outer transitions are too weak to be detectable. As an example, the second order splitting of  $\text{Cr}^{3+}$ ,  $\text{Fe}^{3+}$ , and  $\text{Gd}^{3+}$  in  $\alpha\text{-Al}_2\text{O}_3$  is plotted in Figure 3.14 as a function of frequency. The room temperature data for  $\text{Cr}^{3+}$ ,  $\text{Fe}^{3+}$  and  $\text{Gd}^{3+}$  (35 and 130 GHz) show a reasonable match with the theoretical estimates; at higher frequencies there are some deviations. Since these spectra were measured at 60–80 K, the ZFS could be slightly different (up to 5%) from the room temperature value.<sup>5, 26–28</sup>

This could explain the deviation seen in the  $\text{Gd}^{3+}$  second order splitting, which (as can be seen in Figure 3.14) is consistently too high. The more or less constant second order splitting of  $\text{Fe}^{3+}$  above 190 GHz might be attributed to a second site,

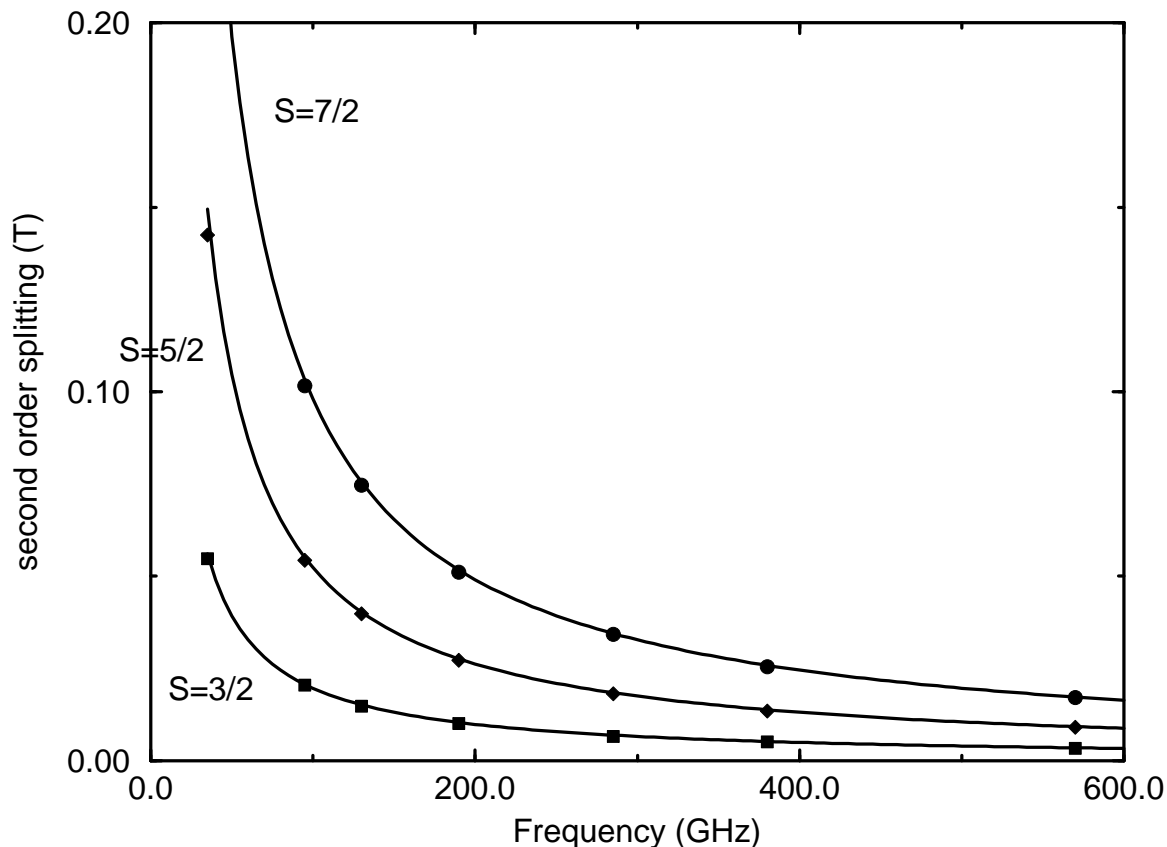


**Figure 3.13:** Size of the second orders splitting as a function of frequency and spin state. The solid line is the splitting as given by equation 3.8; the dots give the size of the splitting as estimated from calculated powder spectra. These data were calculated using  $g=2.000$ ,  $D=0.0570 \text{ cm}^{-1}$ ,  $E=0 \text{ cm}^{-1}$ .

similar to that found for  $\text{Gd}^{3+}$ . Measurements at higher frequency on a sample with less dopant (resulting in smaller linewidths) might give more information on this subject.

### 3.4 Structural interpretation of ZFS parameters

Analysis of ZFS distribution data should give information on the structural variability of the impurity atom with a precision comparable to X-ray crystallography ( $\approx 0.03 \text{ \AA}$ ).

If it is assumed that the impurity atom moves along the  $C_3$  axis (as shown in Figure 3.15, the displacement  $\Delta Z$  can be calculated from the ZFS parameters using Newman's superposition model.<sup>29</sup>

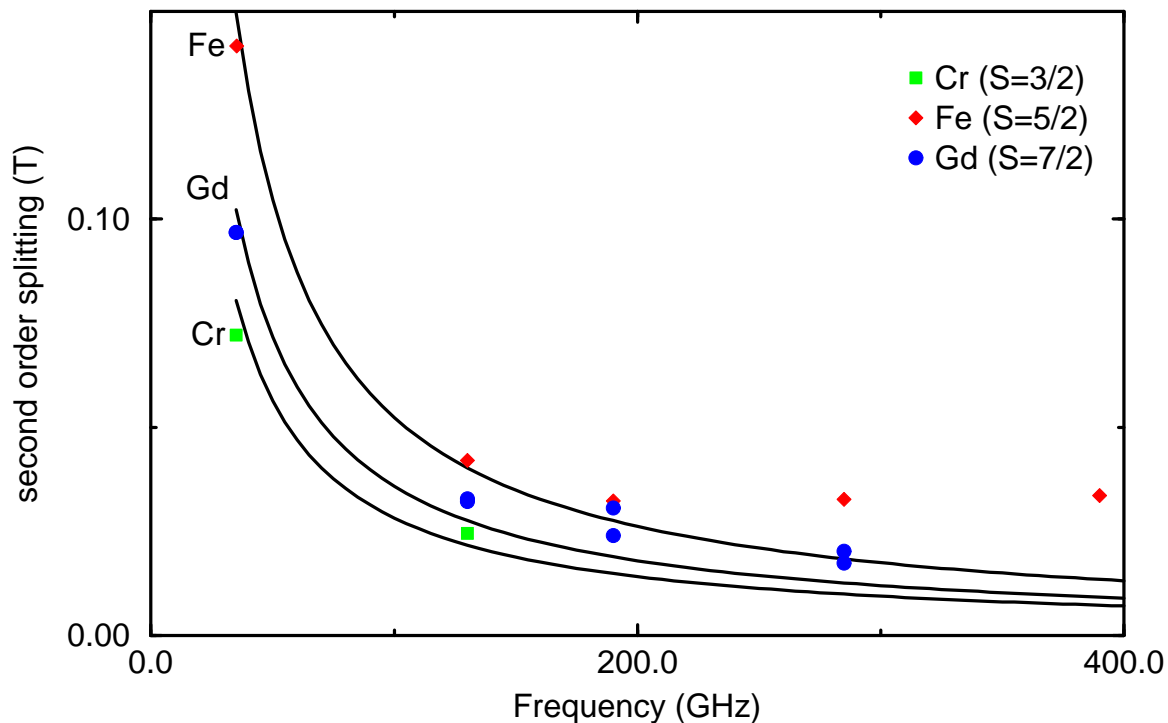


**Figure 3.14:** Second order splitting as measured for  $\text{Cr}^{3+}$ ,  $\text{Fe}^{3+}$  and  $\text{Gd}^{3+}$  as a function of frequency. The solid line is the second order splitting as calculated by equation 3.8, using literature values for the ZFS. Since the  $\text{Gd}^{3+}$  spectra show two  $\text{Gd}^{3+}$ -species, the second order splitting of these species are shown separately.

This model postulates that ZFS parameters can be described in terms of additive uniaxial crystal-field contributions from nearest-neighbor ions. For  $D$  and  $E$ , the following expressions are given:<sup>15</sup>

$$D = b_0^2 = \frac{1}{2} \bar{b}_2(R_0) \sum (3 \cos^2 \theta - 1) \left( \frac{R_0}{R_i} \right)^{t_2} \quad (3.9)$$

$$3E = b_2^2 = \frac{3}{2} \bar{b}_2(R_0) \sum \sin^2 \theta \cos 2\phi \left( \frac{R_0}{R_i} \right)^{t_2} \quad (3.10)$$

in which  $R_i$  is the distance between the metal ion and ligand  $i$ ,  $\theta$  is the angle between the ligand and the  $z$ -axis of a Cartesian set fixed at the metal ion, and  $\phi$  is the angle in the  $xy$ -plane.  $\bar{b}_2(R_0)$ ,  $R_0$  and  $t_2$  are empirically determined parameters, and are dependent on the metal ion and ligands.

Using  $\bar{b}_2(R_0) = -0.26 \pm 0.1 \text{ cm}^{-1}$ ,  $t_2 = 7$  and  $R_0 = 2.019 \text{ \AA}$  from ref. 30, Wen-Chen calculated that the  $\text{Fe}^{3+}$  atom has to move  $0.05_{-0.03}^{+0.06} \text{ \AA}$  towards the larger oxygen triangle to match the experimental  $D$  value.<sup>31</sup> As can be seen in Figure 3.16,  $D$  is very sensitive to changes in the position of the iron atom. Using Figure 3.16, the distribution

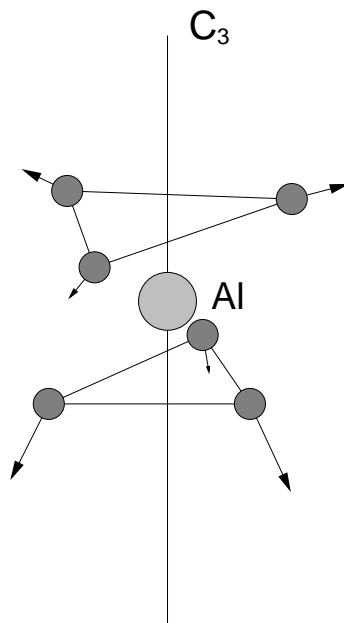


**Figure 3.15:**  $\text{AlO}_6$  octahedron showing the shifts of the oxygen atoms used

in  $D$  can be transformed to a distribution in  $\text{Fe}^{3+}$  displacements; a distribution of  $0.044 \text{ cm}^{-1}$  (as found from the 130 GHz spectra) translates to a distribution in  $\text{Fe}^{3+}$  displacements of  $0.04 \text{ \AA}$ .

The  $\text{Fe}^{3+}$  displacement given above does not explain the distribution in  $E$  found for  $\text{Fe}^{3+}$ ; movement of the iron atom along the  $C_3$  axis keeps axial symmetry preserved, whereas the distribution in  $E$  can only be explained by a small fluctuation in axial symmetry. Assuming that the structure around the iron atom can be regarded as an annealing defect, in which the ‘high temperature’ geometry is still preserved, does not give an immediate solution to this problem. Calculating  $D$  and  $E$  for the structure of  $\alpha\text{-Al}_2\text{O}_3$  at 2170 K (as determined by X-ray crystallography)<sup>32</sup> gives a slightly smaller  $D$  value, but  $E$  still equals to zero, because trigonal symmetry is still maintained in both structures. The only way to obtain a non-zero value for  $E$ , is to either shift the  $\text{Fe}^{3+}$  atom out of the center of the  $\text{AlO}_6$  octahedron, or to expand or shrink only one of the two oxygen triangles, using the displacement vector from the difference between the 2170 K structure and the 300 K structure, as shown in Figure 3.15. An additional constraint is that the  $D$  value should be restricted to the values allowed by the distribution in  $D$ . Since  $D$  is extremely sensitive to changes in the distance between the oxygen atoms, this effectively fixes the position of the iron atom. It also means that an out of plane-shift is unlikely, and that in our model we have to adjust the Fe displacement to match the experimental  $D$  value. The results of the latter approach are shown in Figure 3.16. From

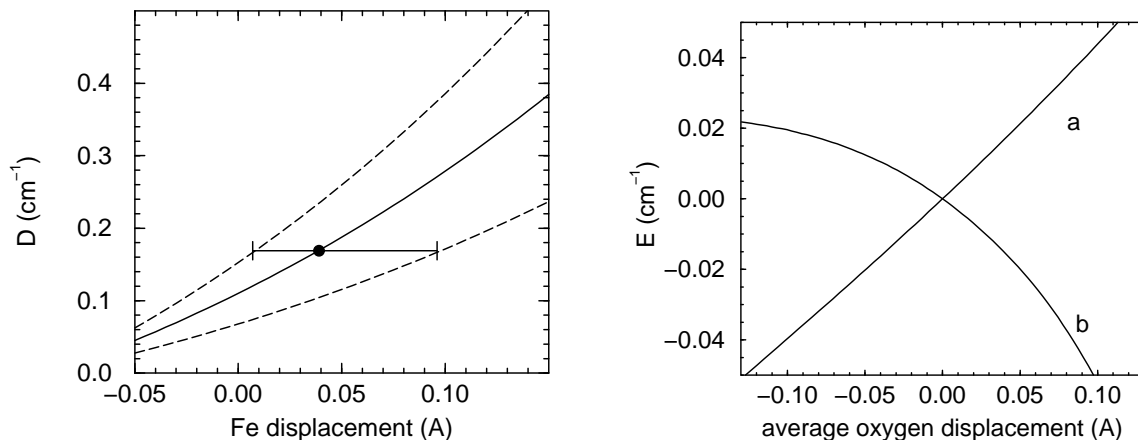


**Figure 3.16:**

**Left:** Effect of displacement of the Fe<sup>3+</sup> ion (relative to the aluminum position) on  $D$ , as calculated by Newman's superposition model. The dashed lines indicate the error in the calculated  $D$  value, using the error in  $\bar{b}_2(R_0)$  ( $=-0.26 \pm 0.1$  cm<sup>-1</sup>). The dot indicates the experimental value of  $D$ ; the error bar is a guide to the eye.

**Right:** Effect of expanding or shrinking only the smaller (a) or larger (b) oxygen triangle on the rhombic ZFS parameter  $E$ , as calculated by Newman's superposition model.

these figures, it can also be derived that the experimentally found distribution in  $E$  of  $0.022$  cm<sup>-1</sup> can be explained by an average oxygen displacement of  $0.06$  Å for both oxygen triangles. It can also be seen that displacements of each triangle affects  $E$  in a different way; when the size of the larger triangle is altered, the effects on  $E$  are linear for both negative and positive  $E$  values. Changes in the smaller oxygen triangle will result in nonlinear distributions of  $E$  much earlier. In our simulations, we have used a Gaussian distribution, symmetrical around  $E=0$ ; if a non-symmetrical distribution was found, this could indicate preferential distortions of the smaller oxygen triangles.

Using the data given by Müller<sup>33</sup> a similar calculation for the Cr<sup>3+</sup> atom can be made. Using  $\bar{b}_2(R_0)=-2.36 \pm 0.12$  cm<sup>-1</sup>,  $t_2=-0.24 \pm 0.06$  and  $R_0=2.027$  Å the displacement of the Cr<sup>3+</sup> atom using  $D=+0.1908$  cm<sup>-1</sup> is calculated as  $0.017$  Å.<sup>4,5</sup> Crystal structure data indicates a shift of  $0.03$  Å, which seems to match reasonably well with the latter value.<sup>34</sup> It should be noted that although there has been some controversy whether the superposition model is valid for Cr<sup>3+</sup>,<sup>35,36</sup> it appears that the model holds for Cr<sup>3+</sup> in trigonal symmetry (as in  $\alpha$ -Al<sub>2</sub>O<sub>3</sub> and LaAlO<sub>3</sub>).<sup>33</sup>

## 3.5 Conclusion

We have demonstrated the application of HF-EPR to amorphous high spin systems, in this case  $\text{Cr}^{3+}$ ,  $\text{Fe}^{3+}$ , and  $\text{Gd}^{3+}$  in  $\alpha\text{-Al}_2\text{O}_3$ . At high frequency, the resulting EPR spectra are easier to interpret, and estimates for the main ZFS parameters can be obtained more or less directly from the spectra. For a complete evaluation of all ZFS parameters, a multifrequency approach employing EPR at conventional frequencies remains a necessity. Together with the simplification of the EPR spectra also the interpretation of a linewidth effect in terms of distributions in ZFS parameters becomes much easier at high frequency.

It was also found that HF-EPR can distinguish between distributions in different ZFS parameters, as was shown for  $\text{Cr}^{3+}$  and  $\text{Fe}^{3+}$  in  $\alpha\text{-Al}_2\text{O}_3$ . For  $\text{Cr}^{3+}$  in  $\alpha\text{-Al}_2\text{O}_3$ , the distribution in  $D$  is larger than that in  $E$ , whereas for  $\text{Fe}^{3+}$  in  $\alpha\text{-Al}_2\text{O}_3$ , the opposite holds.

We have also shown that the second order splitting can be a good alternative for estimating the value of  $D$ , when the other transitions are too much broadened by ZFS distributions. Also, in agreement with theory, the second order splitting remains longer noticeable for spin systems with higher multiplicities.

## 3.6 Acknowledgments

We thank Dr. S.P.J. Albracht, Department of Biochemistry, University of Amsterdam, for measuring the 4 GHz spectrum of  $\text{Fe}^{3+}$  in  $\alpha\text{-Al}_2\text{O}_3$ . We thank Dr. R. de Gelder, Crystallography Department, University of Nijmegen, for powder diffraction measurements of the  $\alpha\text{-Al}_2\text{O}_3$  samples.

# Bibliography

- [1] J. Peisach, W.E. Blumberg, S. Ogawa, E.A. Rachmilewitz, and R.Oltzik, *J. Biol. Chem.*, **1971**, 246, 3342.
- [2] W.E. Blumberg and J. Peisach, *Ann. New York Acad. Sci.*, **1973**, 222, 539.
- [3] D.S. McClure, *J. Chem. Phys.*, **1963**, 38, 2289.
- [4] E.O. Schulz-DuBois, *Bell Systems Techn. J.*, **1959**, 38, 271.
- [5] H. Klein, U. Scherz, M. Schulz, H. Setyono, and K. Wisznewski, *Z. Physik. B*, **1977**, 28, 149.
- [6] G.S. Bogle and H.F. Symmons, *Proc. Phys. Soc.*, **1959**, 73, 531.
- [7] G. Morin and D. Bonnin, *J. Mag. Res.*, **1999**, 136, 176.
- [8] S. Geschwind and J.P. Remeika, *Phys. Rev.*, **1961**, 122, 757.
- [9] F. Abbatista, A. Delmastro, G. Gozzelino, D. Mazza, M. Vallino, G. Busca, and V. Lorenzelli, *J. Chem. Soc. Faraday Trans*, **1990**, 86, 3653.
- [10] S. Simon, A. van der Pol, E.J. Reijerse, A.P.M. Kentgens, G.-J.M.P. van Moorsel, and E. de Boer, *J. Chem. Soc. Faraday Trans*, **1995**, 91, 1519.
- [11] S.P.J. Albracht, J.W. van der Zwaan, and R.D. Fontijn, *Biochim. Biophys. Acta*, **1984**, 766, 254.
- [12] P.J. van Dam. *Multi-Frequency EPR studies on biological systems*. PhD thesis, University of Nijmegen, The Netherlands, 1998.
- [13] M. Boonman. *Millimeter wave spectroscopy in high magnetic fields*. PhD thesis, University of Nijmegen, The Netherlands, 1998.
- [14] E. van der Horst. PhD thesis, University of Nijmegen, The Netherlands, in preparation.
- [15] D.J. Newman and B. Ng, *Rep. Prog. Phys.*, **1989**, 52, 699.
- [16] E. Meirovitch and R. Poupko, *J. Phys. Chem.*, **1978**, 82, 1920.
- [17] W.B. Lynch, R.S. Boorse, and J.H. Freed, *J. Am. Chem. Soc.*, **1993**, 115, 10909.
- [18] C.M. Brodbeck and L.E. Iton, *J. Chem. Phys.*, **1985**, 83, 4285.



- 
- [19] H.W. de Wijn and R.F. van Balderen, *J. Phys. Chem.*, **1967**, *46*, 1381.
- [20] G. van Veen, *J. Mag. Res.*, **1978**, *30*, 91.
- [21] L.E. Iton and J. Turkevitch, *J. Phys. Chem.*, **1977**, *81*, 435.
- [22] C. Legein, J.Y. Buzaré, G. Silly, and C. Jacoboni, *J.Phys.:Condens. Matter.*, **1996**, *8*, 4339.
- [23] C. Legein, J.Y. Buzaré, G. Silly, and C. Jacoboni, *J.Phys.:Condens. Matter.*, **1995**, *7*, 3853.
- [24] Y. Xu, Y. Chen, K. Ishizu, and Y. Li, *Appl. Magn. Reson.*, **1990**, *1*, 283.
- [25] R.A. Shepherd and W.R.M. Graham, *J. Chem. Phys.*, **1984**, *81*, 6080.
- [26] Z. Wen-Chen, *Phys. Rev. B*, **1996**, *54*, 1117.
- [27] I.N. Geifman and M.D. Glinchuk, *Soviet Physics–Solid State*, **1971**, *13*, 872.
- [28] Z. Wen-Chen, *J.Phys.:Condens. Matter.*, **1997**, *9*, 5081.
- [29] D.J. Newman and W. Urban, *Adv. Phys.*, **1975**, *24*, 793.
- [30] M. Heming and G. Lehmann, *Electron paramagnetic resonance of the solid state*, (The Canadian Society for Chemisty, Ottawa, Canada), p. 163, 1987.
- [31] Z. Wen-Chen, *Physica B*, **1998**, *245*, 119.
- [32] N. Ishiwaze, T. Miyata, I. Minato, F. Marúmo, and S. Iwai, *Acta. Cryst. B*, **1980**, *B36*, 228.
- [33] K.A. Müller and W. Berlinger, *J.Phys. C*, **1983**, *16*, 6861.
- [34] J.W. McCauley and G.V. Gibbs, *Z. Krist*, **1972**, *135*, 453.
- [35] J.F. Clare and S.D. Devine, *J.Phys. C*, **1984**, *17*, L581.
- [36] D.J. Newman, *J.Phys. C*, **1982**, *15*, 6627.

# Chapter 4

## Effects of a distribution in Zero Field Splitting parameters on the EPR lineshape for Fe(III) in rhombic systems

### 4.1 Introduction

EPR is an often used technique to determine the coordination of transition metal ions. For  $S = 1/2$  systems, this is accomplished by analysis of the  $g$ -values using ligand field theory; for high spin systems ( $S > 1/2$ ), this is possible by evaluating the zero field splitting tensor  $\mathbf{D}$  in the spin Hamiltonian

$$\mathcal{H} = \beta\mathbf{H} \cdot \mathbf{g} \cdot \mathbf{S} + \mathbf{S} \cdot \mathbf{D} \cdot \mathbf{S} = \beta\mathbf{H} \cdot \mathbf{g} \cdot \mathbf{S} + D(S_z^2 - \frac{1}{3}S(S+1)) + E(S_x^2 - S_y^2) \quad (4.1)$$

in which the ratio  $E/D$  is a measure for the rhombicity of the high spin complex. Although the basic ideas of determining the coordination geometry of a high spin complex from its effective  $g$ -values originate from the early 60s,<sup>1-4</sup> it still is not possible to compute a completely matching X-band EPR spectrum for relatively simple model compounds, such as Fe(III)-EDTA. It has been pointed out that these typical lineshapes might originate from a distribution in Zero Field Splitting (ZFS) parameters.<sup>5,6</sup>

In this work the effect of distributions in various ZFS parameters for systems with ZFS values above or equal to the excitation frequency will be discussed. We do this by measuring two different Fe(III) complexes with typical lineshapes, Fe(III)EDTA in water/glycerol and Fe(III) in the protein rubredoxin, at microwave frequencies at and above the ZFS, and explore the possibilities to simulate the experimental spectra using distributions in the ZFS parameters.

EPR spectra with a resonance at  $g=4.3$  are observed very frequently for  $S=5/2$  systems. This resonance is often interpreted as a signature for a rhombic crystal field.<sup>1,3,7</sup> The  $g=4.3$  signal was first observed for  $\text{Fe}^{3+}$  in glass,<sup>8</sup> but has since then been observed in numerous systems, varying from ceramic materials,<sup>9</sup> simple complexes with EDTA or other ligands,<sup>4</sup> and various biological systems such as transferrin or ferrichrome-A.<sup>4,10</sup>

It has been noted before that it is unusual that the  $g=4.3$  resonance is so predominant.<sup>5</sup> In fact, most EPR spectra of  $S=5/2$  compounds appear to be either rhombic ( $g=4.3$ ,  $g=9$ ) or axial ( $g=6$ ,  $g=2$ ) with relatively small deviations; other geometries are rarely observed.

This finding has drawn relatively little attention, which may be due to the fact that the interpretation of the ZFS parameters  $D$  and  $E$  took a relatively long time, using a variety of models. For example, the first interpretation of the  $g=4.3$  signal by Castner *et al.*<sup>3</sup> used a spin Hamiltonian in which  $D = 0$  and  $E \gg h\nu$ , representing extreme rhombicity of the D-tensor.

Wickman *et al.*<sup>10</sup> and Blumberg<sup>2</sup> showed that after rotation of the ZFS tensor axes, this description is equivalent to  $|E/D| = \frac{1}{3}$ , with both  $E$  and  $D$  large with respect to  $g\beta H$ . This explanation seems more reasonable, since it is expected that there will be an axial crystal field (D) contribution along the direction of the greatest (or smallest) metal-ligand interaction.

Several authors have noted that any complex with spin-Hamiltonian parameters for which the higher order term  $a$  (see equation 4.4, below) fits the equality  $4a = 3D - 9E$ , will give an isotropic line at  $g=4.3$ .<sup>9,11-13</sup> The notion expressed here is that symmetry determinations used in EPR are usually limited to the direct coordination sphere of the metal atom, whereas the point group symmetry of the crystal (and thus the point symmetries of the metal ion site) could be considerably lower.

These interpretations only tried to explain the position of the resonance peaks, not the typical 'spiked' lineshape seen for many biological  $g=4.3$  signals. Even for effective  $g$ -values, it should be possible to describe the EPR spectrum with a Gaussian or Lorentzian lineshape. Typical  $g=4.3$  signals however, such as the Fe(III)-EDTA spectrum shown in Figure 4.1a, look far from a simple Gaussian lineshape. The main difficulty in simulating this kind of spectra is getting the linewidth right, without losing the sharp feature at  $g=4.3$ . An early solution was to use different linewidths for the  $g_x, g_y$  and  $g_z$  effective  $g$ -values,<sup>14,15</sup> but this approach fails when the resulting parameter set is used to simulate the more complex spectra at 35 or 130 GHz.

A first attempt to explain the typical lineshape of these spectra was made by Petersson,<sup>5</sup> who argued that when spectra with a broad distribution in effective  $g$ -values are computed, it might be possible to obtain sharp features on top of a broad line, due to an 'overexpression' of certain  $g$  values. However, this approach

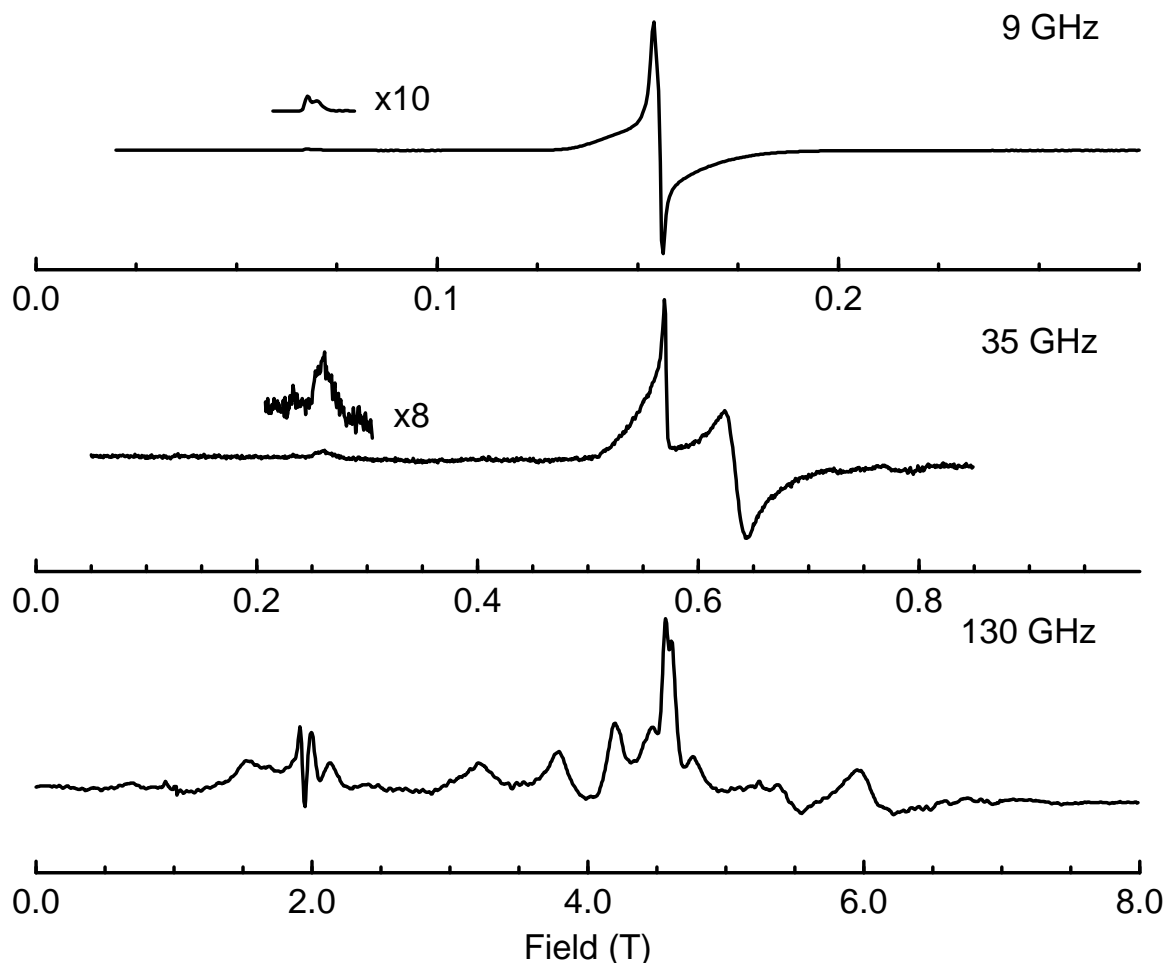


**Figure 4.1:** EPR spectra of 10 mM Fe(III)EDTA in H<sub>2</sub>O/glycerol at 9.3245 GHz (a), 35.01 GHz (b) and 130.00 GHz (c). Experimental conditions (9, 35 and 130 GHz): microwave power 1, 2, 2 mW, modulation amplitude 2, 1, 3 Gauss, modulation frequency 100, 80, 11 kHz, temperature 6, 45, 20 K.

was only applied to effective  $g$ -values; a connection with a distribution in the ZFS parameters was not worked out in more detail. Distributions in effective  $g$ -values have also been used to determine the positional variation of the iron atom in myoglobin,<sup>16,17</sup> but this work did not include a powder lineshape analysis.

Distributions in zero field splittings have been used by several authors to model EPR spectra.<sup>18–25</sup> Due to computational constraints, most authors have limited the amount of spectra used in the final calculations to at most a few dozen, or used a distribution in only one ZFS parameter. Another difficulty is that calculating spectra in the regime where the ZFS becomes comparable to the microwave frequency is non-trivial. Most authors either use an effective  $g$ -value approach (when

$D \gg h\nu$ ),<sup>18,19</sup> or use third order perturbation theory to calculate spectra, which gives only valid results when  $D \ll h\nu$ .<sup>21,22</sup>

Gaffney simulated the predicted EPR spectrum of lipoxygenase (using exact diagonalization) at various frequencies (9-250 GHz),<sup>23,24</sup> but has since then not applied this technique to other systems. Morin used a more sophisticated method to calculate distributions in ZFS parameters for  $\text{Fe}^{3+}$  in  $\alpha\text{-Al}_2\text{O}_3$  and gibbsite.<sup>25</sup>

A different approach to the lineshape problem was used by Stößer *et al.*<sup>26</sup> Using a large Gaussian distribution in the higher order terms  $a$  and  $F$ , they were able to reproduce the typical lineshapes of X-band spectra of  $\text{Fe}^{3+}$  ions in oxide and fluoride glasses.

All the above authors use a Gaussian distribution in the ZFS parameter to calculate EPR spectra. Although this turns out to give relatively good results, it should be noted that the experimental EPR spectra show the local structure of the high spin system, which is a distribution in various bond angles and distances. The shape of this distribution is unknown; it is also not directly clear how the shape of this local symmetry distribution translates to a ZFS distribution shape.

## 4.2 Method

EPR spectra of high-spin systems (with  $S > 3/2$ ) can be described by a spin Hamiltonian of the form:

$$\mathcal{H} = \beta\mathbf{H} \cdot \mathbf{g} \cdot \mathbf{S} + \sum_{k=2,4,6} \sum_{q=-k}^{q=k} B_k^q \mathbf{O}_k^q \quad (4.2)$$

where  $\mathbf{O}_k^q$  are the normalized Stevens operators, and the  $B_k^q$  coefficients are related to the traditional ZFS parameters by

$$\begin{aligned} B_2^0 &= b_2^0/3 = D/3 & B_2^2 &= b_2^2/3 = E \\ B_4^0 &= b_4^0/60 = (a/120 + F/180) & B_4^2 &= b_4^2/60 = H/3 & B_4^4 &= b_4^4/60 = (a/24 + 2G) \end{aligned} \quad (4.3)$$

For  $S=5/2$ , this expression can be written as<sup>27,28</sup>

$$\mathcal{H} = \beta\mathbf{H} \cdot \mathbf{g} \cdot \mathbf{S} + \frac{D}{3}\mathbf{O}_2^0 + E\mathbf{O}_2^2 + \left(\frac{a}{120} + \frac{F}{180}\right)\mathbf{O}_4^0 + \frac{H}{3}\mathbf{O}_4^2 + \left(\frac{a}{24} + 2G\right)\mathbf{O}_4^4 \quad (4.4)$$

The  $G$  and  $H$  terms are so small that they are usually ignored. Calculation of the resulting EPR powder spectrum for given spin Hamiltonian parameters at microwave frequency  $\nu$  is done by numerical diagonalization of the spin Hamiltonian at several field positions to determine the EPR transitions and transition probabilities, followed by integration over the unit sphere. The method for simulating individual high-spin powder spectra has been described elsewhere in more detail.<sup>25</sup>

The simplest, but also computationally most expensive way of calculating ZFS distributions is by numerically integrating EPR spectra over a suitable range of ZFS parameters, i.e.

$$\sum_{D=\bar{D}-\Delta D}^{D=\bar{D}+\Delta D} \sum_{E=\bar{E}-\Delta E}^{E=\bar{E}+\Delta E} \sum_{a=\bar{a}-\Delta a}^{a=\bar{a}+\Delta a} \sum_{F=\bar{F}-\Delta F}^{F=\bar{F}+\Delta F} \mathbf{D}(D, E, a, F) SL(D, E, a, F) \Gamma \quad (4.5)$$

where  $\mathbf{D}$  is the (unknown) ZFS distribution shape function,  $SL$  is the spectral library, and  $\Gamma$  is a Gaussian or Lorentzian lineshape function. While the calculation of a single spectrum can be done relatively quickly (in the order of seconds using currently available personal computers), when the size and shape of the distribution is unknown, a single simulation could take up to several hours, or even days. This is especially true when  $D \approx h\nu$ . Since the individual spectra are not interdependent, it makes sense to store the unconvoluted spectra on disk. This splits the simulation process in two steps: first a spectral library is calculated for a particular range of ZFS parameters, which is then used by a separate program to generate the final distribution, using a user-defined distribution shape function and linewidth. This reduces the time needed for distribution simulations to sub-second calculation times, meaning that distribution shapes can be fitted interactively, if desired. The only limiting factor in this simulation step is the size and loading time of the spectral database. On personal workstations, the loading time of the spectral database can be further reduced (by a factor of 2 to 10) if the size of the database is slightly less than the amount of memory available, to prevent unnecessary swapping. Although equation 4.5 describes a four-dimensional distribution, in the simulations shown here, distributions in only one or two parameters were used, to simplify fitting and also reduce memory pressure and computation time. For the relatively broad distributions used here, distributions containing 75x75 spectra were typically fine-grained enough to prevent numerical artifacts. When combining distributions in  $D$  or  $E$  with the higher order parameters  $B_4^0$  or  $B_4^4$ , the number of calculated spectra in the higher order parameter direction had to be increased to 150 to avoid jagged lineshapes.

Interactively finding a ‘matching’ shape function can be a tedious process (or even impossible). Finding arbitrary distribution functions is a complicated problem, as has been noted by Schaefer.<sup>29</sup>

In the following discussion, two methods are used to find matching distributions: In the first method we try out some simple distribution shapes (Gaussian or rectangular distributions) using distributions in one or two ZFS parameters; the other method uses a genetic algorithm to fit a random distribution (in one or two ZFS parameters) by minimizing the sum of the squares of the difference between the fitted spectrum and the experimental spectrum. The latter method is used to find

suitable starting points for distribution shapes, or to check whether the parameters of a calculated spectral library are close to a possible solution.

In both cases, the distribution shape is determined by a spline fit through 20 points (or 10x10 points, in case of a distribution in two parameters), from which the weight of each individual spectrum is then calculated.<sup>30</sup> Apart from reducing the number of independent variables, this also standardizes the input and output files used in the fitting process.

The reason for choosing a genetic algorithm (or GA) to fit random distributions, is that GAs are robust, easily adjustable, and have no limitations on the amount of parameters that can be fitted. Furthermore, given enough time, and a correct error function, they will always find the global minimum of a minimization problem. More information on GAs is given in references 31–34. The simulations shown here were calculated using PGAPack,<sup>35</sup> using default values, with a population size of 500, a mutation probability of 0.001, random initialization of the starting genes, and 8 bits for each variable (which gives a resolution of 0.04 on a range of 0 to 10). As noted earlier, the error function used is the sum of the squares of the differences between the simulation and the experimental spectrum.

## 4.3 Experimental

### Sample preparation

The Fe(III)EDTA complex was prepared by adding a 15 mM solution of Fe(NO<sub>3</sub>)<sub>3</sub>·9H<sub>2</sub>O to an equal volume of a 50 mM Na<sub>2</sub>EDTA solution. 0.5 ml of this solution was then mixed with 0.5 ml 86% glycerol. 50–200 μL of the complex solution was then transferred into a quartz tube and frozen in liquid nitrogen.

### Spectroscopy

9 GHz EPR was done on a Bruker ER 220 spectrometer. A homebuilt 35 GHz spectrometer has been constructed from a Varian E-110 Q-band bridge, a Varian 60 MHz NMR magnet connected to a Varian EPR power supply, a PAR 117 lock-in amplifier and a home built cryo-insert plus modulation unit. The 130 GHz spectrometer has been described previously in ref. 36.

## 4.4 Results

The best way to determine distributions in ZFS parameters would be to measure at frequencies far above the ZFS, so that the EPR spectrum is completely resolved. When measuring at sufficiently high frequencies, it should be possible to determine ZFS parameters and distributions more or less directly from these spectra.

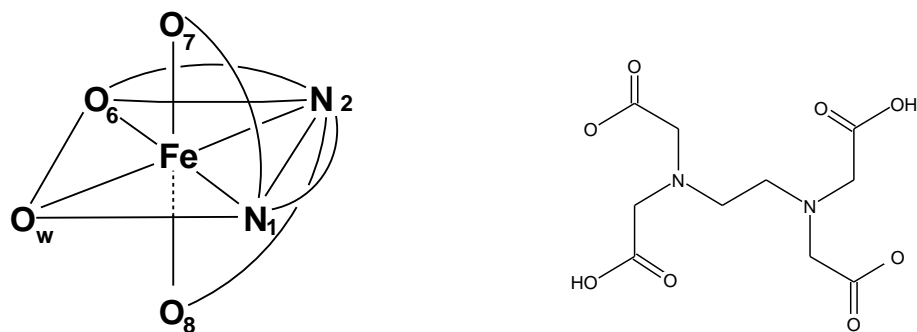


**Figure 4.2:** Left: Schematic structure of the Fe(III)EDTA complex at pH=7.  $O_w$  represents a coordinated water molecule.

**Right:** The chemical structure of the EDTA ligand.

For the Fe(III) complexes studied here, which are expected to have  $D$ -values of about  $0.7\text{--}1.6\text{ cm}^{-1}$ ,<sup>4</sup> this would mean that EPR spectra should be measured at at least 200 GHz, preferably 300 GHz. Unfortunately, current technology still does not allow the measurement of (for example) 10 mM Fe(III)EDTA spectra at these frequencies with a reasonable S/N level, which is mainly due to lack of microwave power.

An alternative would be to use an intermediate frequency, such as 95 or 130 GHz. However, as Figure 4.1c shows, although these spectra do contain the same information as their 200 or 300 GHz equivalents, these spectra are much more complicated, and a proper analysis is practically impossible. The 130 GHz spectrum of Fe(III)EDTA also suffers from the problem that the microwave phase is unknown, which is due to way this spectrum has been measured (see chapter 2 for more discussion on this topic). To simplify the analysis, we therefore start with analyzing the 9 and 35 GHz EPR spectra, and we then check the obtained distributions at 130 GHz.

#### 4.4.1 EPR of Fe(III)EDTA in water/glycerol

Iron(III) in aqueous solution has been known to form octahedral complexes with ethylenediaminetetraacetate (EDTA), which is visible in 9 GHz EPR as a  $g=4.3$  signal.<sup>4,37-39</sup> X-ray crystallography shows that EDTA act as a pentadentate ligand, with a water molecule as a sixth ligand (see Figure 4.2).<sup>40</sup> In the crystalline form, the Fe-O bonds *trans* to the Fe-N bonds (Fe- $O_w$ , Fe- $O_6$ ) are longer on average than the axial Fe-O bonds (Fe- $O_7$ , Fe- $O_8$ ).<sup>40</sup> In a basic environment, Fe(III)EDTA forms a dimer, in which the iron atoms are linked together via oxo or hydroxo bridging.<sup>41,42</sup> At neutral pH, the monomer is the only species present.

Since  $D \gg h\nu$  at X-band, these spectra should be relatively insensitive to changes in the magnitude of the ZFS, as long as the rhombicity ( $E/D$ ) remains the same.



**Table 4.1:** Axis transformations to rotate system  $b - f$  to the standard axis system  $a$ , and the respective values of  $E, D$  and  $\lambda = E/D$  in the standard system  $a$  in terms of their values in each axis system; taken from ref. 43.

System	Transformation	E	D	$\lambda$
$a$	$x_1 \rightarrow x_1; y_1 \rightarrow y_1; z_1 \rightarrow z_1$	$E_1$	$D_1$	$\lambda_1$
$b$	$x_2 \rightarrow x_1; y_2 \rightarrow z_1; z_2 \rightarrow y_1$	$-\frac{1}{2}(D_2 - E_2)$	$-\frac{1}{2}(D_2 + E_2)$	$\frac{1-\lambda_2}{1+3\lambda_2}$
$c$	$x_3 \rightarrow y_1; y_3 \rightarrow x_1; z_3 \rightarrow z_1$	$E_3$	$D_3$	$-\lambda_3$
$d$	$x_4 \rightarrow y_1; y_4 \rightarrow z_1; z_4 \rightarrow x_1$	$-\frac{1}{2}(D_4 - E_4)$	$-\frac{1}{2}(D_4 + E_4)$	$\frac{1-\lambda_4}{1+3\lambda_4}$
$e$	$x_5 \rightarrow z_1; y_5 \rightarrow x_1; z_5 \rightarrow y_1$	$-\frac{1}{2}(D_5 - E_5)$	$-\frac{1}{2}(D_5 + E_5)$	$\frac{1-\lambda_5}{1+3\lambda_5}$
$f$	$x_6 \rightarrow z_1; y_6 \rightarrow y_1; z_6 \rightarrow x_1$	$-\frac{1}{2}(D_6 - E_6)$	$-\frac{1}{2}(D_6 + E_6)$	$\frac{1-\lambda_6}{1+3\lambda_6}$

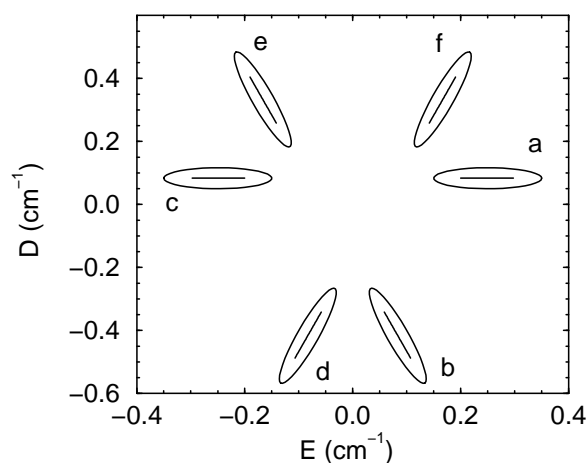


**Figure 4.3:** Effect of the axis transformations given in Table 4.1 on  $E/D$  distributions.

The linewidth effects at X-band should be completely accounted for using a distribution in rhombicity, i.e. a distribution in  $D$  or  $E$  only.

35 GHz simulations using the initial parameter set found at 9.5 GHz (which has a distribution in  $E$  only) showed no resemblance to the experimental spectrum at all. This is to be expected, since at 35 GHz the microwave frequency becomes comparable to  $2D$ , and the  $g=4.3$  signal begins to split up. This means that for an accurate simulation, distributions in both  $D$  and  $E$  should be included. This makes the 35 GHz spectra more informative, but also complicates the simulation of these spectra.

When spectra are simulated with a constant  $D$  and a relatively large distribution in  $E$  around  $E/D=1/3$ , ranging from  $E/D=0.2$  to  $E/D=0.46$ , some of the typical features of the experimental spectrum (Figure 4.1) show up, as can be seen in Figure 4.5. It should be noted that a distribution *around*  $E/D=1/3$  is necessary to

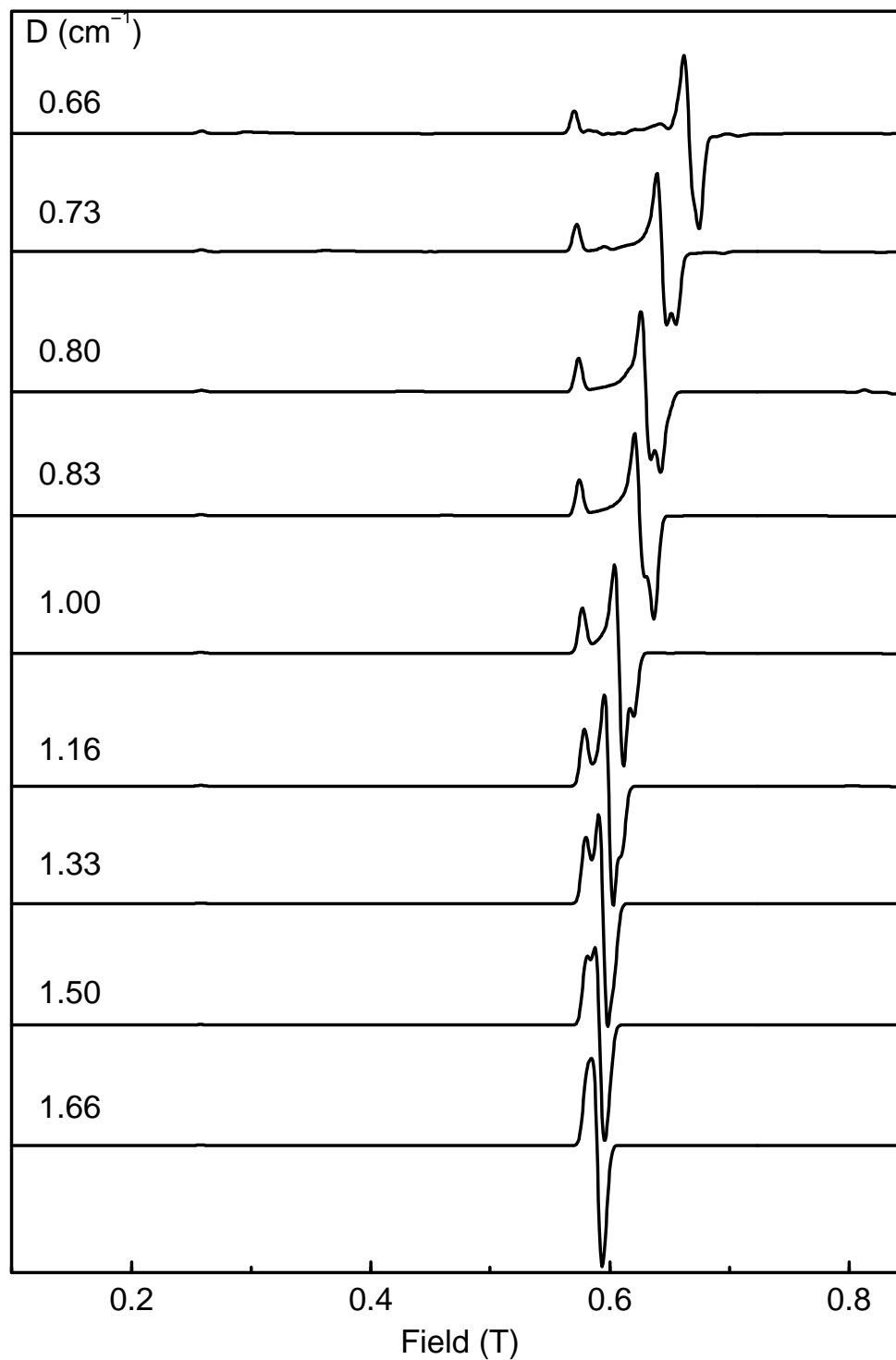


**Figure 4.4:** Effect of zero field splitting (without distribution in ZFS parameters) at 35 GHz EPR spectra of an  $S=5/2$  system.  $D=0.66 \cdots 1.66 \text{ cm}^{-1}$ ,  $E/D=1/3$ .

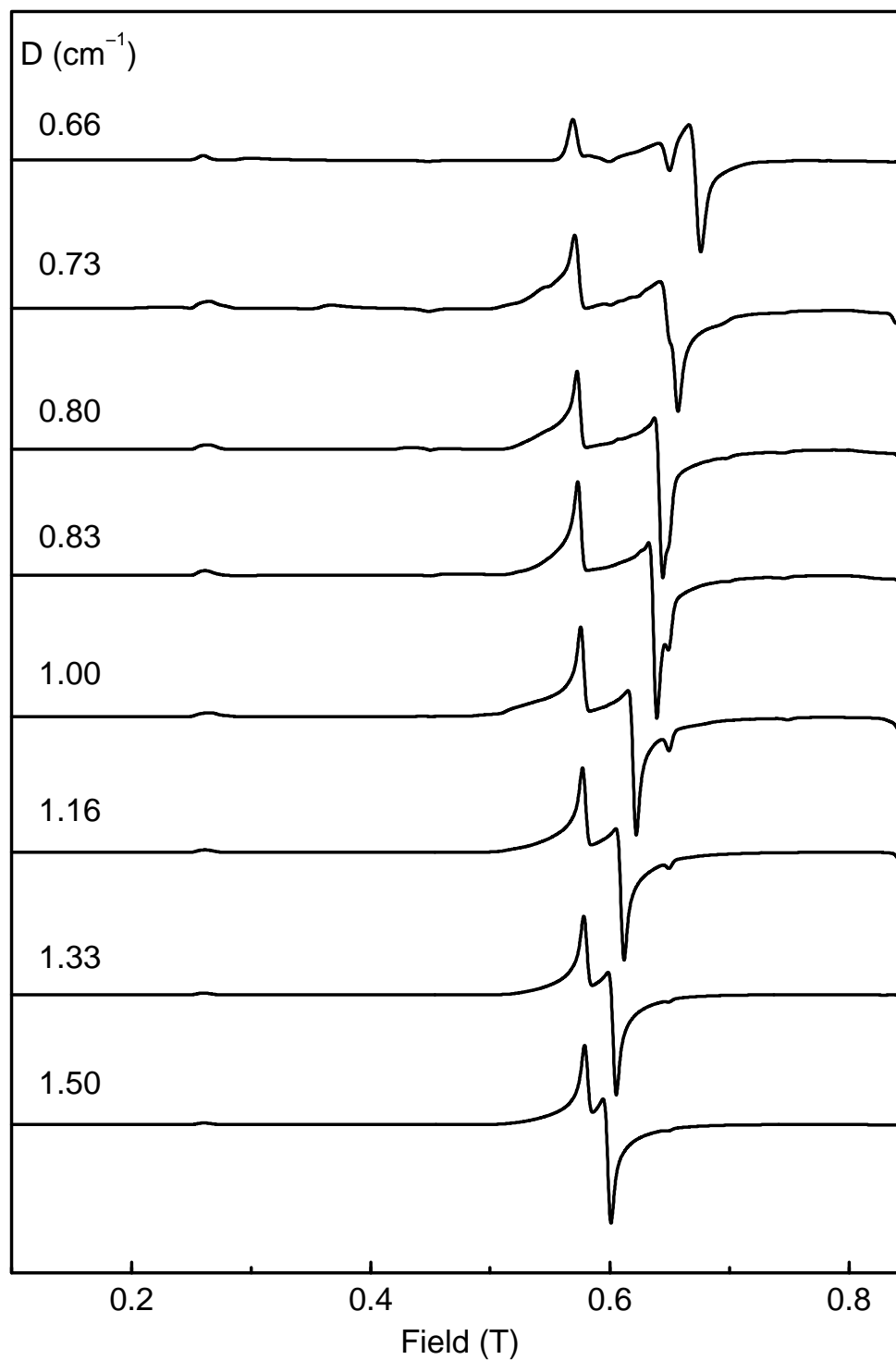


**Figure 4.5:** Effect of a block-shaped distribution in the ZFS parameter  $E$  at 35 GHz EPR spectra of Fe(III) EDTA.  $D=0.66 \dots 1.66 \text{ cm}^{-1}$ ,  $E/D=1/3$ ; the distribution in  $E$  is 5% of the  $D$  value.

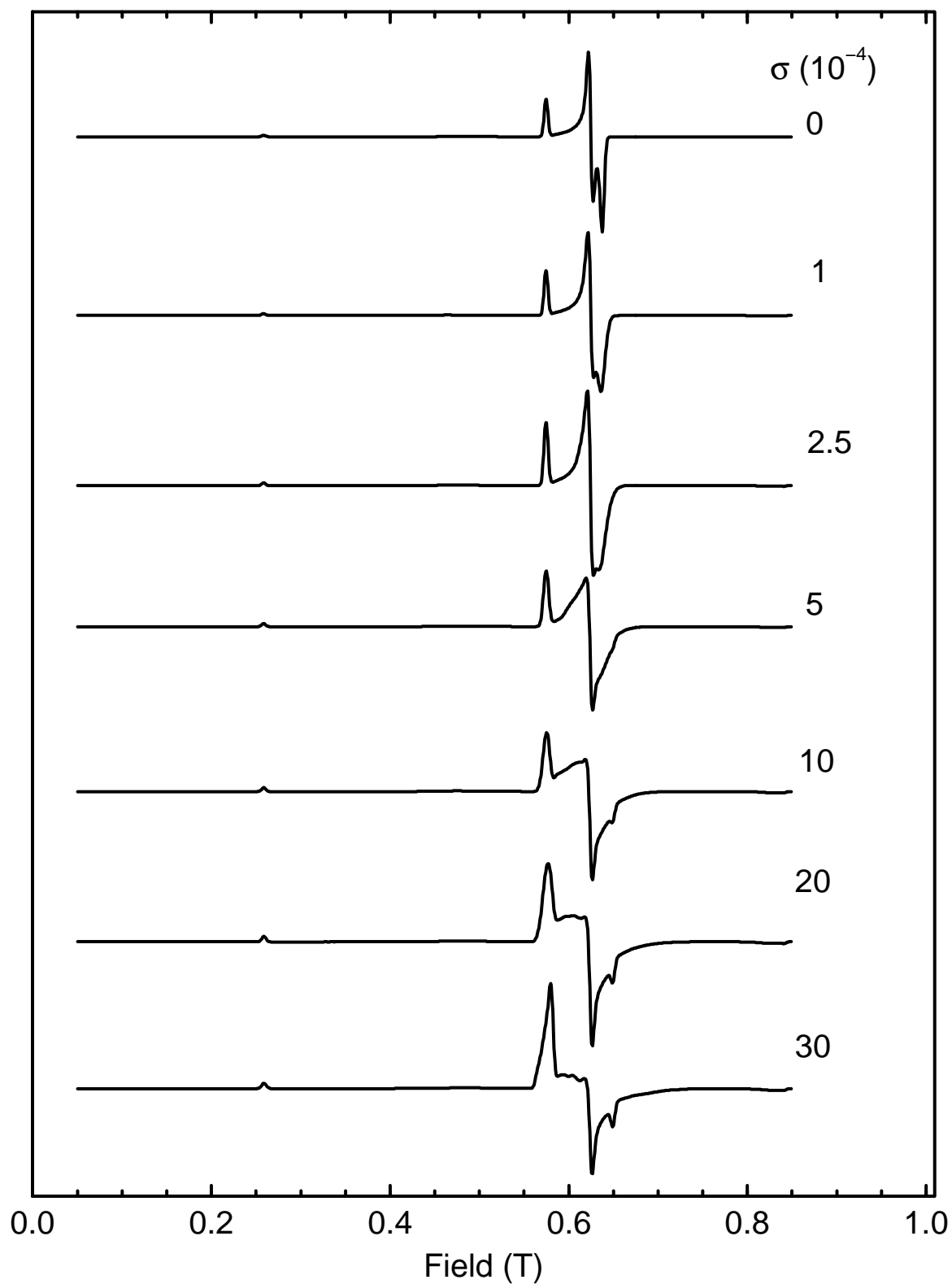


**Figure 4.6:** Effect of a Gaussian distribution in the higher order zero field splitting parameter  $a$  at 35 GHz EPR spectra of Fe(III) EDTA. Simulation parameters:  $D=0.833 \text{ cm}^{-1}$ ,  $E/D=1/3$ ; the distribution width  $\sigma$  used for  $a$  varies from 0 ...  $30 \cdot 10^{-4} \text{ cm}^{-1}$ .

obtain this lineshape; distributions ranging from  $E/D=0.2$  to  $1/3$ , or  $1/3$  to  $0.46$  show a significantly poorer match. This effect is less noticeable when  $D/\nu > 2/3$ , ie  $D > 0.9 \text{ cm}^{-1}$  at  $35 \text{ GHz}$ .

An explanation for the finding that such distributions in  $E$  give a good fit is that  $E/D$  values larger than  $1/3$  can be expressed in a 'normal'  $E/D$  value between  $0$  and  $1/3$ , and a larger (or negative)  $D$  value by changing the ZFS tensor axes.<sup>43</sup> As can be seen in Figure 4.3, which shows the effect of such transformations, a distribution which exceeds  $E/D=1/3$  (such as plot 'a' in Figure 4.3) can also be regarded as a distribution in which rhombicity changes in combination with an varying  $D$  value (plots 'b','d','e' and 'f'), instead of a distribution in rhombicity only. In other words, Figure 4.5 shows a correlated distribution in  $E$  and  $D$ .

When Figure 4.5 is compared to Figure 4.4, it appears that ZFS values are perceptibly lower. For the series of spectra simulated with ZFS distribution, the splitting in the  $g=4.3$  resonance is observable even for relatively large ZFS values. If one would try to fit ZFS parameters from these spectra without including distribution effects, one would tend to underestimate the ZFS values.

Although the simulations shown in Figure 4.5 look quite reasonable, a further improvement might be obtained by including a distribution in the higher order parameters  $a$  and/or  $F$ . In the simulations shown here, the distributions in  $E$  and  $D$  are quite large, with rhombicity values ranging from  $0.2$  to  $0.45$ . This suggests a relatively large mobility of the ligand atoms. It can therefore be expected that a distribution in the higher order terms  $a$  and  $F$  is also present, since these parameters are also sensitive to changes in local symmetry.<sup>44</sup> In combination with the distribution in  $E$  used above, they could serve as another mechanism for linewidth broadening.

However, there are several complications involved when including higher order distributions.

- It is not known how changes in the higher order parameters  $a$  and  $F$  affect the effective  $g$ -values. Furthermore, the lineshape is now affected by three or four different parameters simultaneously. Although it is possible to calculate spectra for every possible combination of ZFS parameters, analytical expressions for peak shifts or splittings as a function of all terms have not been given in the literature, even though this might be possible when  $D \gg h\nu$ . When  $D \approx h\nu$ , which is the case here, a perturbation treatment is no longer allowed, and the spin Hamiltonian has to be solved by exact diagonalization. This also means that analytical expressions for the field positions can not be given at all.

- We look at the accumulated lineshape, e.g. we are interested in the equivalent of ‘turning points’ in ZFS parameters. This also means that analytical expressions for peaks or linewidths of the distributed spectrum are impossible to derive.
- Although approximate values for  $D$  and  $E$  for Fe(III)EDTA and other complexes are known, values for the higher order terms  $a$  and  $F$  are unknown; we assume that distributions in these terms are centered around zero. Furthermore, it can be expected that these distributions are correlated in some way with the distributions in  $D$  and  $E$ ; it could be possible that only a small ridge in a four-dimensional parameter-space is responsible for the resulting lineshape.

As noted before, HF-EPR might be able to solve some of these problems, since when  $D \ll h\nu$ , expressions for the individual transitions (and how they are affected by changes in ZFS parameters) are easy to derive.

In spite of all these complications, it would still be useful to see if it is possible to obtain better fits using a distribution in  $a$  or  $F$  and a  $E/D$  distribution. As a first guess for the size of these distributions, we calculate the ‘boundary values’ at which both parameters still have peaks at field positions in the range of the experimental spectrum. Approximate maximum values for the distributions widths in  $a$  and  $F$  are  $\pm 0.01 \text{ cm}^{-1}$  and  $\pm 0.04 \text{ cm}^{-1}$  respectively.

Using a 2D-distribution in  $E$  and  $F$ , the spectra in Figure 4.7–4.8 are obtained. Although these spectra are by no means perfect fits, they indicate that the spectrum of Fe(III)EDTA in water/glycerol can be adequately explained using a correlated distribution in both  $D, E$  and the higher order parameter  $F$ . These Figures also show that there are (at least) three different distributions which all give reasonable fits. Although the size and shape of the distribution does matter, EPR at or below the ZFS is not sufficient to distinguish between distributions. Furthermore, distributions in  $a$  or  $F$  have approximately the same effects, and can both be used to give similarly good matching fits.

Calculating 9 GHz spectra using the distributions found at 35 GHz shows that the distribution shown in Figure 4.7a gives the best match at both frequencies. This distribution also yields a reasonable 130 GHz spectrum (Figure 4.10). Figures 4.7 and 4.9 also show that using the 9 and 35 GHz spectra alone, it is difficult to indicate which distribution is the ‘correct’ distribution, since the differences between the various distributions are relatively small at these frequencies.

At frequencies far above the ZFS, it is much easier to distinguish between different distributions, as illustrated in Figure 4.11. 285 GHz EPR might also be useful for other EDTA complexes, such as the peroxo Fe(III)EDTA complex.<sup>38, 45</sup> These com-

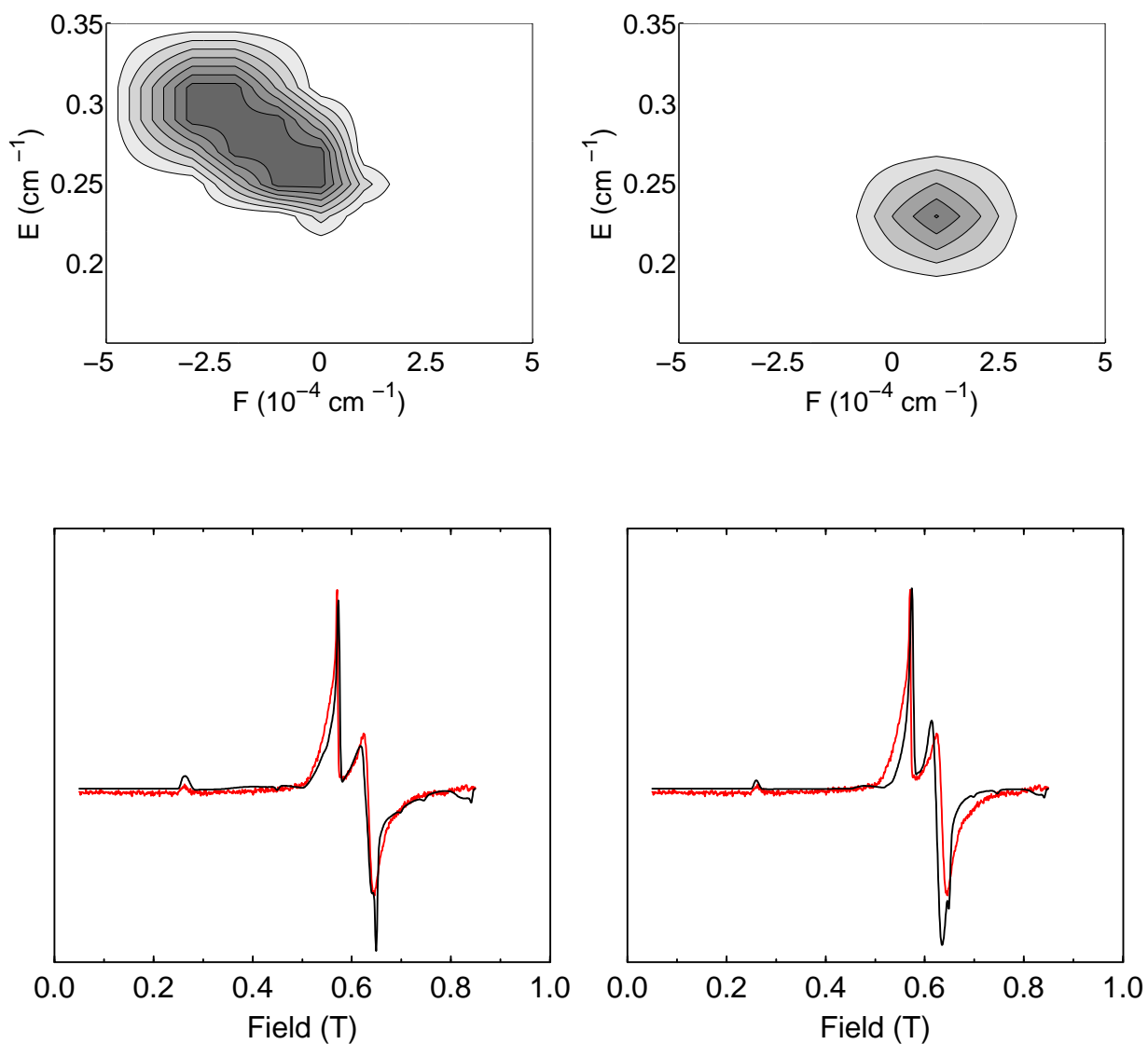


**Figure 4.7:** Different distributions (in  $E$  and  $F$ ), using a  $D$  value of  $0.83 \text{ cm}^{-1}$ , all giving reasonable matches with the spectrum of Fe(III) EDTA at 35 GHz. Experimental spectra are shown in grey, simulations in black.

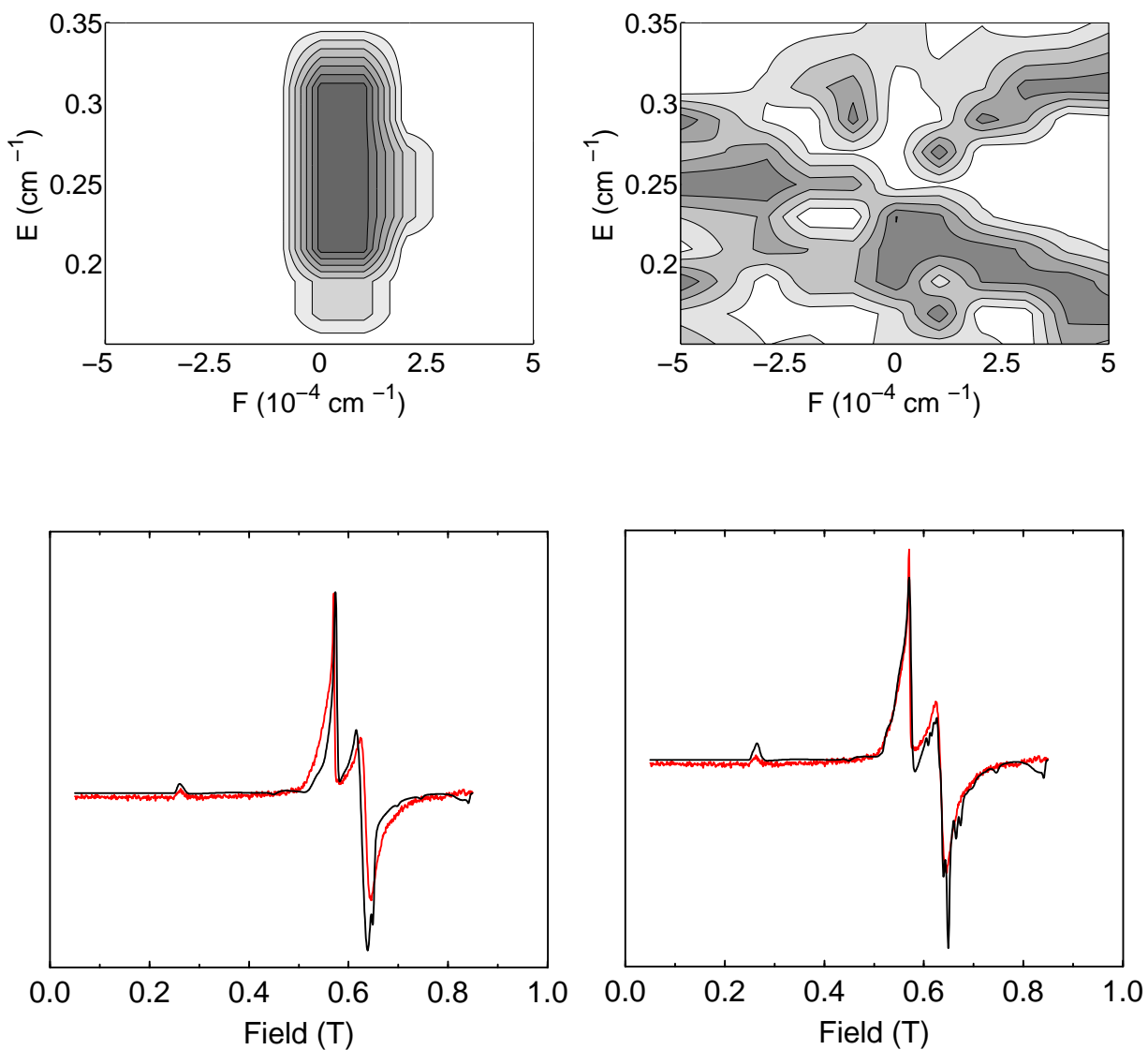


**Figure 4.8:** Different distributions (in  $E$  and  $F$ ), using a  $D$  value of  $0.83 \text{ cm}^{-1}$ , all giving reasonable matches with the spectrum of Fe(III) EDTA at 35 GHz. The distribution at the right is a typical solution found by the genetic algorithm. Experimental spectra are shown in grey, simulations in black.



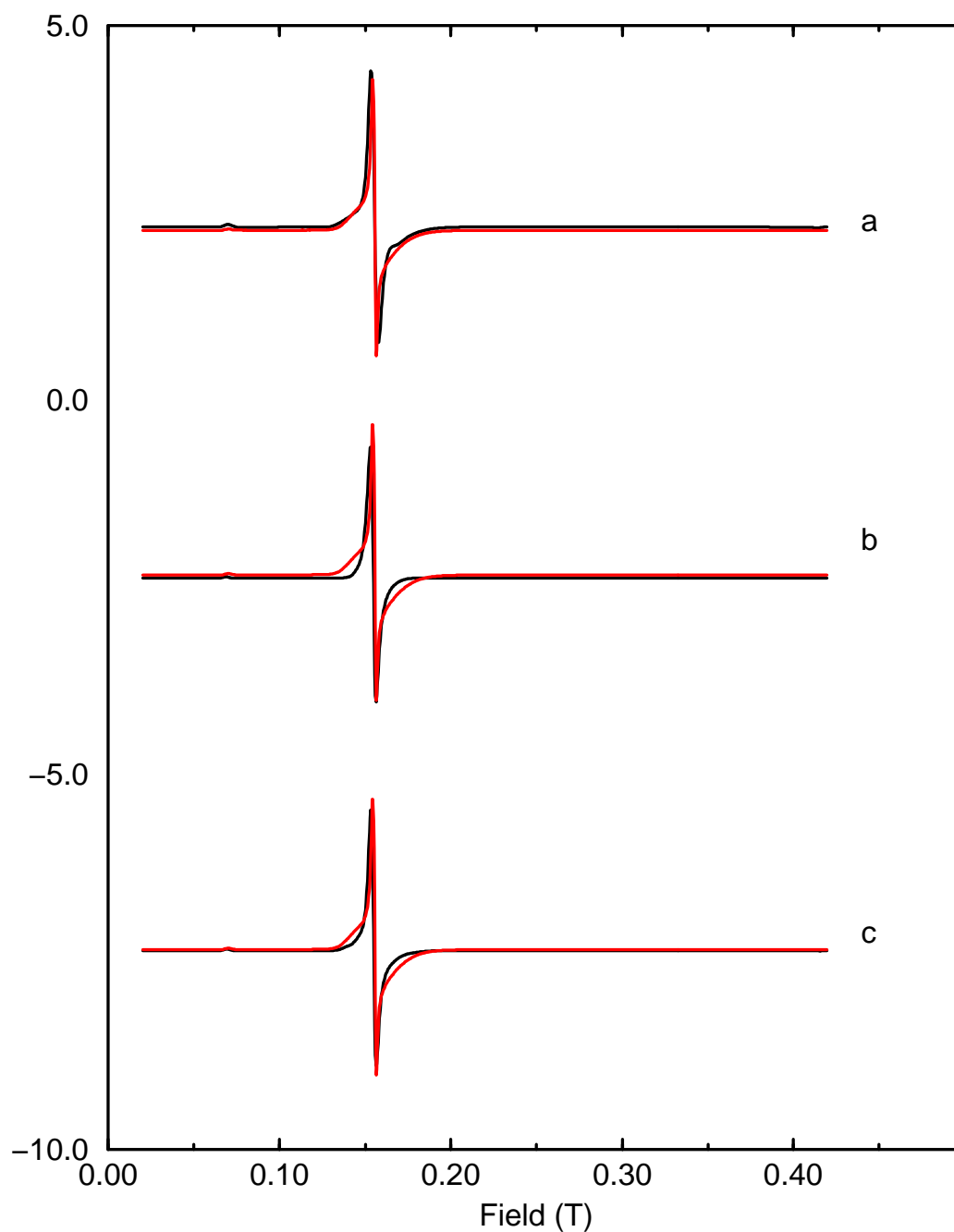


**Figure 4.9:** 9 GHz EPR spectra of Fe(III)EDTA.

**a:** Simulation using the distribution shown at the left of Figure 4.7.

**b:** Simulation using the distribution shown at the right of Figure 4.7.

**c:** Simulation using the distribution shown at the left of Figure 4.8.

Experimental spectrum is shown in grey. All simulations were convoluted with a Gaussian line-shape, using a linewidth of 30 Gauss.

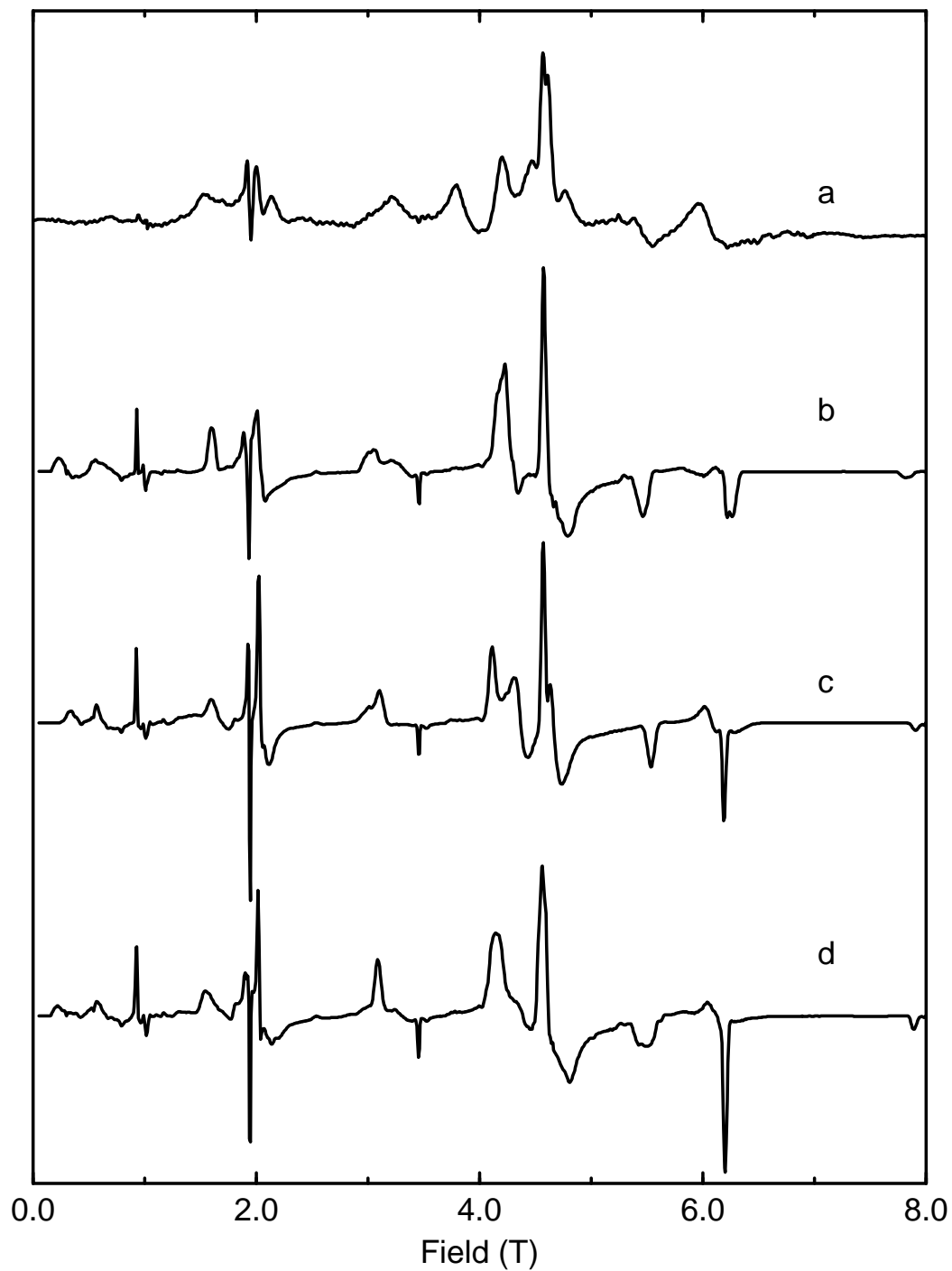


**Figure 4.10:** 130 GHz EPR spectra of Fe(III)EDTA.

**a:** Experimental spectrum.

**b:** Simulation using the distribution shown at the left of Figure 4.7.

**c:** Simulation using the distribution shown at the right of Figure 4.7.

**d:** Simulation using the distribution shown at the left of Figure 4.8.

All simulations were convoluted with a Gaussian lineshape, using a linewidth of 40 Gauss.

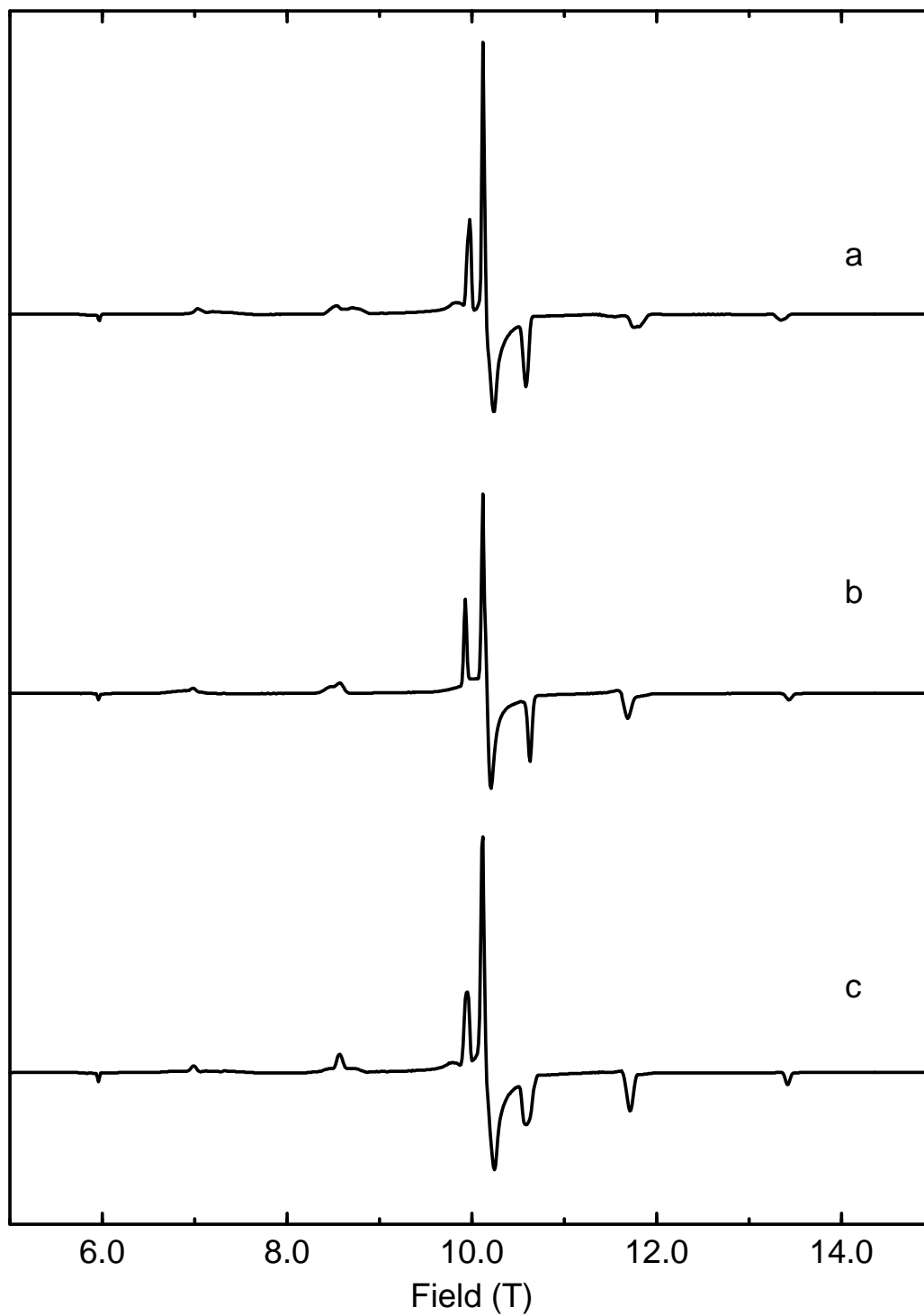


**Figure 4.11:** Predicted 285 GHz EPR spectra of Fe(III)EDTA.

**a:** Simulation using the distribution shown at the left of Figure 4.7.

**b:** Simulation using the distribution shown at the right of Figure 4.7.

**c:** Simulation using the distribution shown at the left of Figure 4.8.

All simulations were convoluted with a Gaussian lineshape, using a linewidth of 40 Gauss.

plexes are expected to have similar ZFS values as Fe(III)EDTA; a HF-EPR study might give more insight in the structural dynamics of this species.

In contrast to the proposal of Stößer *et al.*,<sup>26</sup> a distribution in higher order parameters alone is not sufficient to explain the experimental spectrum. The main problem with this approach is a too small linewidth of the low-field peak in the Q-band spectrum, as can be seen in Figure 4.6.

Fitting the spectrum using a genetic algorithm turns out to be not a very good method to find matching distributions, or even as a tool to find good initial starting points for distributions. This is mainly caused by the fact that a least-squares minimization is a poor choice for the error function, and that a different error function should be used. We are interested to find a reasonable lineshape in the first place, and a good matching spectrum as a second criterium. A least-squares minimization strategy focusses especially on the latter. Unfortunately, it is quite difficult to express a lineshape in analytical functions.

Furthermore, as can be seen in the plot at the right in Figure 4.8, genetic algorithm fitting shows that there are several distributions which match the experimental spectrum, which all appear equally valid to the genetic algorithm. However, a distribution such as shown in Figure 4.8 can not have any physical meaning; distributions such as those in Figure 4.7 make more sense. This becomes clear when these solutions are translated to other frequencies: The distributions shown in Figure 4.7 also give reasonably matching X-band spectra, whereas the physically unrealistic solution found by the genetic algorithm does not match at all.

#### 4.4.2 Fe(III) in rubredoxin.

To explore the possibilities of deriving similar ZFS distributions for other high spin Fe(III) complexes, we have measured EPR spectra of Fe(III) in the protein rubredoxin. The analysis of the Fe(III)EDTA spectra was found to be relatively straightforward; it would be interesting to see if the lineshape of the rubredoxin spectra can also be explained using a ZFS distribution effect, especially since these spectra have a lineshape which differs significantly from the Fe(III)EDTA spectra.

Rubredoxins are relatively small metalloproteins in which the active site consists of one iron coordinated to four cysteinyl sulfurs. The coordination of the iron atom in rubredoxins is approximately tetrahedral (see Figure 4.12).

An examination of the Fe(S-cys)<sub>4</sub> units of these proteins leads to two remarkable observations:<sup>46-49</sup> (1) the [Fe(S-cys)<sub>4</sub>] units are very symmetric and (2) this geometry is highly conserved in most rubredoxins. It is surprising to see that this structure approaches  $D_{2d}$  symmetry, which is the highest possible symmetry for the Fe(SCH<sub>2</sub>)<sub>4</sub> unit, considering the non-linearity of the Fe-S-C linkage. Since proteins

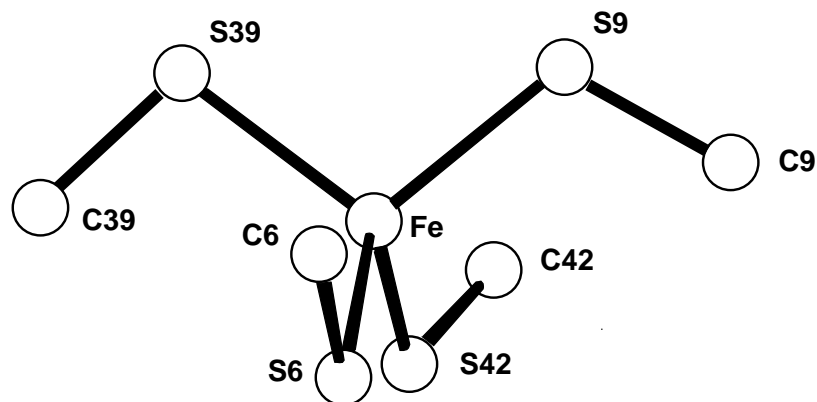


**Figure 4.12:** Diagram of the structure of the  $[\text{Fe}(\text{S-CH})_2]_4$  unit of rubredoxin in its oxidized form, as taken from the crystallographic coordinates from *Desulfovibrio vulgaris*.<sup>48</sup>

are inherently asymmetrical molecules, the highly symmetric and conserved geometry of the  $\text{Fe}(\text{S-cys})_4$  unit is significant.

The electronic spectra of most rubredoxins are very similar to each other; EPR<sup>50–52</sup> and Raman<sup>53,54</sup> spectra each show similar features for these proteins. EPR studies also indicate that the size of the ZFS for these complexes is approximately  $1\text{--}2\text{ cm}^{-1}$ .<sup>55</sup> EXAFS studies show that the Fe-S bonds do not differ by more than  $0.04\text{ \AA}$ ,<sup>56,57</sup> which is also in agreement with X-ray crystallography studies.<sup>46–49,58</sup>

All these data suggest a relatively rigid  $\text{Fe}(\text{S-cys})_4$  core. However, the 9 and 35 GHz EPR (Figure 4.13) hint at a relatively broad distribution in ZFS parameters, which in turn indicates a relative mobile electronic environment. To see if it is possible to obtain distribution sets for this Fe(III) species, 9, 35 and 130 GHz spectra of Fe(III) in *Megasphaera elsdenii* rubredoxin were measured and analyzed, using the same approach as used for the EDTA spectra.

As can be seen in Figure 4.13, the 9 and 35 GHz spectra show considerable similarity; apart from a small splitting around the center peak, and a broadening of the overall spectrum, the lineshape is the same. This is in agreement with a ZFS above  $1.0\text{ cm}^{-1}$ ; distribution simulations with a ZFS below  $1.0\text{ cm}^{-1}$  are always too narrow to match the experimental spectra. If the distribution size is increased, these specific features get lost, and the end result is a spectrum which has too little intensity in the shoulders.

The 9 and 35 GHz spectra of rubredoxin can be adequately simulated using an relatively flat,  $0.4\text{ cm}^{-1}$  wide distribution in  $E$  and  $D$  centered around  $D=1.9\text{ cm}^{-1}$ . In this case, a distribution in the higher order parameters was not necessary. A possible explanation could be that the magnitude of higher order effects might be smaller for the (soft) sulphur ligands than for the relatively hard oxygen and nitrogen ligands in EDTA.

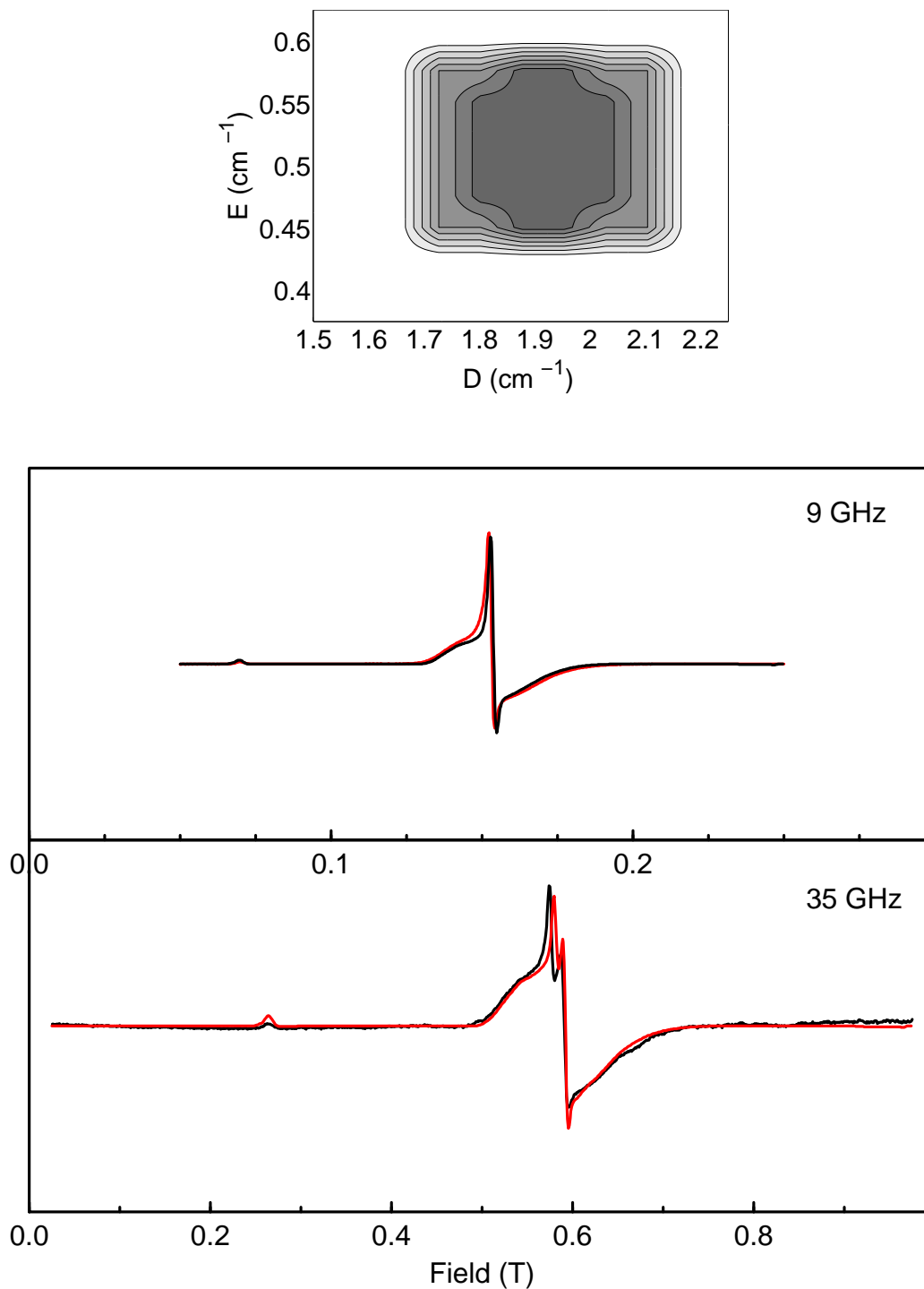


**Figure 4.13:** Experimental (grey) and simulated (black) EPR spectra of *Megasphaera elsdenii* rubredoxin.

Experimental conditions (9 resp. 35 GHz spectra): microwave frequency 9.2272 GHz, 34.96 GHz, microwave power 1, 2 mW, modulation amplitude 8, 8 Gauss, modulation frequency 100, 70 kHz, temperature 16, 40 K.

For the simulations, a distribution in  $D$  and  $E$  (shown in the figure at the top of the page) was used for both frequencies.

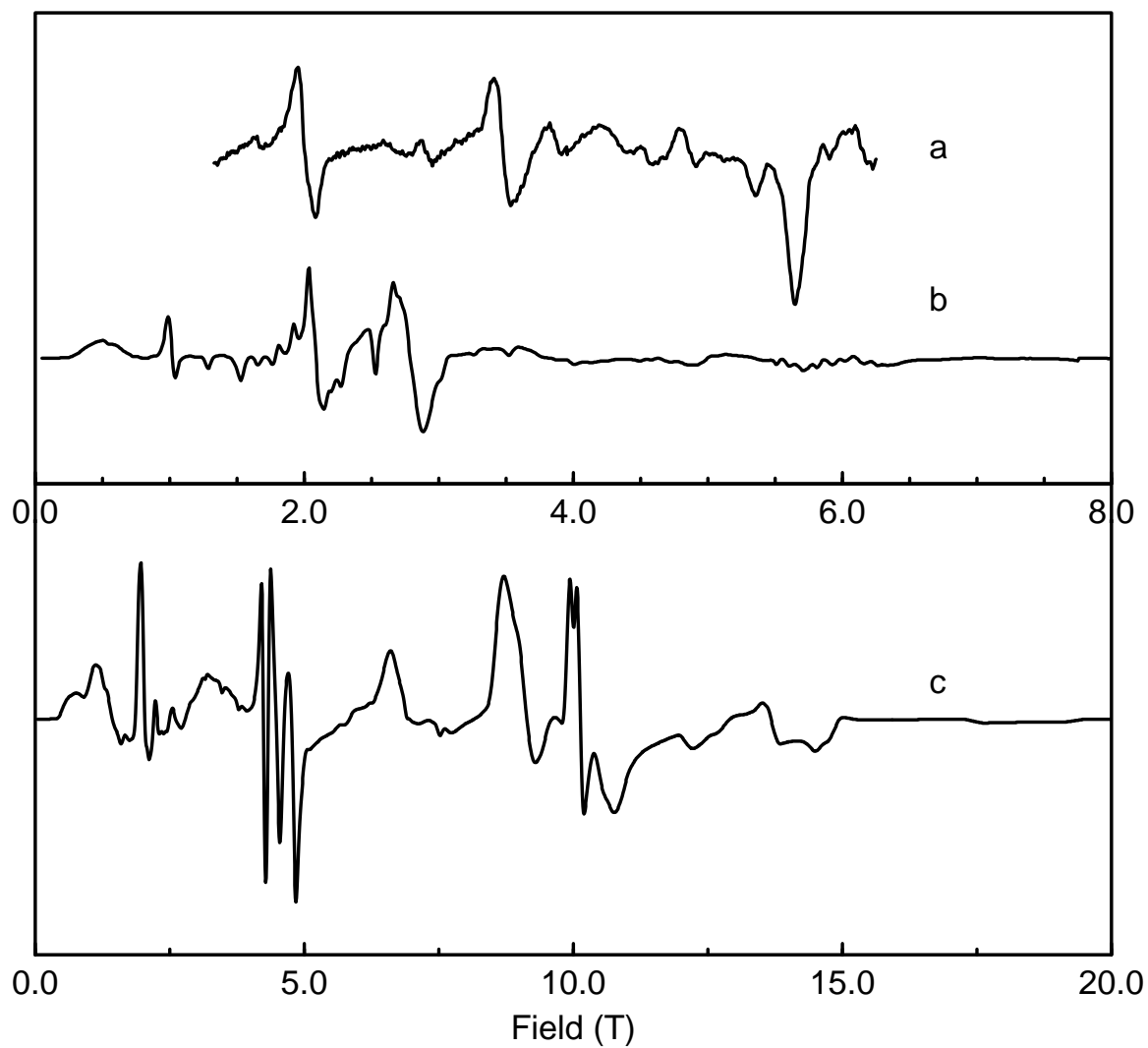


**Figure 4.14:** HF-EPR spectra of rubredoxin from *Megasphaera elsdenii*.

**a:** Experimental spectrum, measured at 130.00 GHz, microwave power 2 mW, modulation amplitude 5 Gauss, modulation frequency 11 kHz, temperature 80 K.

**b,c:** 130 resp. 285 GHz simulation using the ZFS distribution shown in Figure 4.13.

An interesting fact is that the distribution used here is centered around  $E/D=0.26 \pm 0.04$ , which deviates significantly from the typical  $E/D$  value of  $1/3$  usually assigned to 'rhombic' systems with an EPR signal at  $g=4.3$ .

The apparently poorer fit of the 130 GHz spectrum (Figure 4.14) is most likely the result of an error in the estimation of the magnitude of  $D$ . The 9 and 35 GHz spectra are not sensitive to the absolute value of  $D$ , only to distributions in  $D$  and  $E$ . Although the 130 GHz spectrum is sensitive to both terms, it is not straightforward to determine values for  $E$  and  $D$  from this spectrum. For the simulations at 9 and 35 GHz, an eventual increase (or decrease) in  $D$  should also be accompanied with an increase (or decrease) in the ZFS-distribution.

It should be noted that due to the very broad nature of the spectrum at 130 GHz, detection of 10 mM rubredoxin at this frequency is presently at the technical limit of HF-EPR, and the quality of the experimental spectrum is difficult to assess.

A hypothetical 285 GHz spectrum of rubredoxin (using the distribution shown in Figure 4.13) is also drawn in Figure 4.14. Due to the fact that the ZFS of rubredoxin is 3 times larger than Fe(III)EDTA, this spectrum is comparable to the 130 GHz EDTA spectrum. To obtain a spectrum in which the ZFS is resolved, the microwave frequency needs to be increased to 500 GHz or more.

## 4.5 Conclusion

We have shown that the typical lineshapes of bioinorganic Fe(III) complexes are the result of distributions in ZFS parameters. For an adequate simulation of these spectra at 9 and 35 GHz, distributions in  $D$ ,  $E$  and the higher order parameters  $a$  and/or  $F$  have to be taken into account. Although distributions in  $D$  or  $E$  alone already generate relatively good fits, for a complete description of the spectrum, distributions in all ZFS parameters have to be used for Fe(III)EDTA. Surprisingly, the typical lineshape of 9 and 35 GHz spectra of rubredoxins can be explained using a distribution in  $D$  and  $E$  only.

Determination of the shape of these distributions is a difficult problem, and EPR data at microwave frequencies below the ZFS is not really suited for this particular problem. For example, it is not possible to distinguish between different distributions, and the fitting process can be tedious. It can be expected that EPR at frequencies far above the ZFS (200-300 GHz, resp. 500-600 GHz for the systems studied here) will solve these problems, or at least make them more manageable.

Ultimately, one would like to be able to connect the distribution in ZFS to structural changes, using for example Newman's superposition model, in combination with molecular modelling studies.<sup>59, 60</sup> However, due to a lack of suitable data for Fe-N and Fe-S ligands,<sup>61</sup> estimated from model compounds with similar symmetry, calculation of ZFS values is not possible. Clearly, there is room for improvement in technological development and fundamental understanding.





# Bibliography

- [1] R. Aasa, *Biochim. Biophys. Acta*, **1963**, 75, 203.
- [2] W.E. Blumberg, *Magnetic Resonance in Biological systems*, (Pergamon Press, Elmsford, N.Y.), p. 119, 1967.
- [3] T. Castner, G.S. Newell, W.C. Holton, and C.P. Slichter, *J. Chem. Phys.*, **1960**, 32, 668.
- [4] R. Aasa, *J. Chem. Phys.*, **1970**, 52, 3919.
- [5] G.E. Petersson, C.R. Kurkjian, and A. Carnevale, *Phys. Chem. of Glasses*, **1974**, 15, 52.
- [6] J.F. Gibson, *ESR and NMR of paramagnetic species in biological and related systems*, (D. Reidel Publishing Company, Dordrecht, Holland), p. 225, 1979.
- [7] R. Aasa and T. Vänngård, *Arkiv Kemi*, **1965**, 25, 285.
- [8] R.H. Sands, *Phys. Rev.*, **1955**, 99, 1222.
- [9] R.W. Kedzie, D.H. Lyons, and M. Kestigian, *Phys. Rev.*, **1965**, 138, A918.
- [10] H.H. Wickman, M.P. Klein, and D.A. Shirley, *J. Chem. Phys.*, **1965**, 42, 2113.
- [11] K. Spartalian, W.T. Oosterhuis, and J.B. Neilands, *J. Chem. Phys.*, **1975**, 62, 3538.
- [12] N.S. VanderVen, K. Spartalian, W.T. Oosterhuis, and J. Ashkin, *Bull. Am. Phys. Soc.*, **1974**, 19, 373.
- [13] D.G. McGavin and W.C. Tennant, *Mol. Phys.*, **1982**, 45, 77.
- [14] W.E. Blumberg and J. Peisach, *Ann. New York Acad. Sci.*, **1973**, 222, 539.
- [15] M.I. Scullane, L.K. White, and N.D. Chasteen, *Ann. New York Acad. Sci.*, **1982**, 47, 383.
- [16] R. Calvo and G. Bemski, *J. Chem. Phys.*, **1976**, 64, 2264.
- [17] F.G. Fiamingo, A.S. Brill, D.A. Hampton, and R. Thorkildsen, *Biophys. J.*, **1989**, 55, 67.
- [18] C.M. Brodbeck and L.E. Iton, *J. Chem. Phys.*, **1985**, 83, 4285.
- [19] C. Legein, J.Y. Buzaré, G. Silly, and C. Jacoboni, *J. Phys.: Condens. Matter.*, **1996**, 8, 4339.

- [20] C. Legein, J.Y. Buzaré, G. Silly, and C. Jacoboni, *J.Phys.:Condens. Matter.*, **1995**, 7, 3853.
- [21] E. Meirovitch and R. Poupko, *J. Phys. Chem.*, **1978**, 82, 1920.
- [22] G.D. Markham, B.D. Nageswara, and G.H. Reed, *J. Mag. Res.*, **1979**, 33, 595.
- [23] B.J. Gaffney, D.V. Mavrophilipos, and K.S. Doctor, *Biophys. J.*, **1993**, 64, 773.
- [24] A.-S. Yang and B.J. Gaffney, *Biophys. J.*, **1989**, 55, 67.
- [25] G. Morin and D. Bonnin, *J. Mag. Res.*, **1999**, 136, 176.
- [26] R. Stößer, G. Scholz, M. Nofz, , T. Grande, and S. Aasland, *Ber. Bunsenges. Phys. Chem*, **1996**, 100, 1588.
- [27] R.M. Golding, M. Kestigian, and W.C. Tennant, *J. Phys. C.: Solid State Phys.*, **1978**, 11, 5041.
- [28] V.K. Jain and G. Lehmann, *Phys. Stat. Sol. B*, **1990**, 159, 495.
- [29] H. Schäfer and E. Sternin, *La Physique au Canada*, **1997**, 3/4, 77.
- [30] B-Spline library version 2.2, based on the book by Carl de Boor: A practical guide to Splines (Springer, New-York 1978)  
<http://www.triumf.ca/people/schadow/software/index.html>.
- [31] L. Davis. *Handbook of Genetic Algorithms*. Van Nostrand Reinhold, New York, 1991.
- [32] D.E. Goldberg. *Genetic Algorithms in Search, Optimization and Machine Learning*. Addison-Wesley, Reading, 1989.
- [33] M Mitchell. *An introduction to Genetic Algorithms*. The MIT Press, Cambridge, 1996.
- [34] T. Baeck. *Genetic Algorithms in Theory and Practice*. The Oxford University Press, Oxford, 1996.
- [35] PGAPack, Mathematics and Computer Science Division Argonne National Laboratory,  
<http://www.mcs.anl.gov/pgapack.html>.
- [36] P.J. van Dam, A.A.K. Klaassen, E.J. Reijerse, and W.R. Hagen, *J. Mag. Res.*, **1998**, 130, 140.
- [37] C.T. Migita, K. Ogura, and T. Yoshino, *J. Chem. Soc. Dalton Trans*, **1985**, 1077.
- [38] S. Fujii, H. Ohya-Nishiguchi, and N. Hirota, *Inorg. Chim. Acta*, **1990**, 175, 27.
- [39] J. Oakes and C.G. van Kralingen, *J. Chem. Soc. Dalton Trans*, **1984**, 1133.
- [40] T. Mizuta, T. Yamamoto, K. Miyoshi, and Y. Kushi, **1990**, 175, 1133.
- [41] H. Schugar, C. Walling, R.B. Jones, and H.B Gray, *J. Am. Chem. Soc*, **1967**, 89, 3712.
- [42] G. Wilkinson, R. D. Gillard, and J. A. McCleverty, editors, *Comprehensive coordination chemistry: the synthesis, reactions, properties and applications of coordination compounds*, (Pergamon Press, Oxford, N.Y.), p. 777ff, 1987.

- [43] P.L. Hall, B.R. Angel, and J.P.E. Jones, *J. Mag. Res.*, **1974**, 15, 64.
- [44] J.M. Gaité, *Electron paramagnetic resonance of the solid state*, (The Canadian Society for Chemistry, Ottawa, Canada), p. 151, 1987.
- [45] F. Neese and E.I. Solomon, *JACS*, **1998**, 120, 12829.
- [46] K.D. Watenpaugh, L.C. Sieker, and L.H. Jensen, *J. Mol. Biol.*, **1980**, 138, 615.
- [47] Z. Dauter, L.C. Sieker, and K.S Wilson, *Acta Crystallogr.*, **1992**, B48, 42.
- [48] L.C. Sieker, R.E. Stenkamp, L.H. Jensen, B. Prickril, and J. LeGall, *FEBS Lett.*, **1986**, 208, 73.
- [49] M. Frey, L. Sieker, F. Payan, R. Haser, M. Bruschi, G. Pepe, and J. LeGall, *J. Mol. Biol.*, **1987**, 197, 525.
- [50] J.C. Rivoal, B. Briat, R. Cammack, D.O. Hall, K.K. Rao, I.N. Douglas, and A.J. Thompson, *Biochim. Biophys. Acta*, **1977**, 493, 122.
- [51] D.E. Bennet and M.K. Johnson, *Biochim. Biophys. Acta*, **1987**, 71, 911.
- [52] L.E. Maelia and S.A. Koch, *Inorg. Chem.*, **1986**, 25, 1896.
- [53] R.S. Czernuszewicz, L.K. Kilpatrick, S.A. Koch, and T.G. Spiro, *J. Am. Chem. Soc.*, **1994**, 116, 7134.
- [54] V.K. Yachandra, J. Hare, I. Moura, and T.G. Spiro, *J. Am. Chem. Soc.*, **1983**, 105, 6455.
- [55] J. Peisach, W.E. Blumberg, E.T. Lode, and M.J. Coon, *J. Biol. Chem.*, **1971**, 246, 5877.
- [56] M.W. Day, B.T. Hsu, L. Joshua-Tor, J.-B. Park, Z.H. Zhou, M.W.W. Adams, and D.C. Rees, *Protein Sci.*, **1992**, 1, 1494.
- [57] B. Bunker and E.A. Stern, *Biophys. J.*, **1977**, 19, 253.
- [58] R. Bau, D.C. Rees, D.M. Kurtz Jr, R.A. Scott, H. Huang, M.W.W. Adams, and M.K. Eidsness, *JBIC*, **1998**, 3, 484.
- [59] D.J. Newman and W. Urban, *Adv. Phys.*, **1975**, 24, 793.
- [60] D.J. Newman and B. Ng, *Rep. Prog. Phys.*, **1989**, 52, 699.
- [61] M. Heming and G. Lehmann, *Electron paramagnetic resonance of the solid state*, (The Canadian Society for Chemistry, Ottawa, Canada), p. 163, 1987.



# Chapter 5

## Analysis of $^{53}\text{Cr}(\text{V})$ hyperfine interaction in $\text{M}_3\text{CrO}_8$ (M=Li, Na, K, Rb, Cs) compounds.

### 5.1 Introduction

The alkali peroxychromates  $\text{M}_3\text{CrO}_8$  (M=Li, Na, K, Rb, Cs) form a small, but interesting group of compounds, in which chromium exhibits the relatively rare pentavalent oxidation state, with one unpaired electron ( $3d^1$ ). Although these compounds have a relatively simple tetragonal lattice structure, they appear to be low-dimensional antiferromagnets, with unexpected magnetic behavior.<sup>1,2</sup> Recently, they have attracted attention as possible standards for field calibration in high-field EPR, and as magnetic refrigerants in the 1–4 K temperature region.<sup>3–6</sup>

The peroxychromates are also interesting as model compounds for dioxygen coordination in mononuclear transition metal complexes.<sup>7–10</sup> Although recent research on these compounds has yielded significant insights in the electronic and magnetic structure,<sup>2,11</sup> details still remain unclear. For example, the localization of the unpaired electron (which could be localized mainly on the Cr ion or on the peroxo ligands) has been disputed,<sup>9,10,12</sup> although the current view is that the unpaired electron resides mainly on the metal ion, aided with significant backdonation from the peroxo ligands.<sup>9</sup> Beside their role in the stabilization of the unpaired electron, the peroxo ligands also modulate the magnetic behavior of these compounds by forming a pathway for electron-electron superexchange. An EPR analysis of the  $g$ -values and hyperfine splittings of the unpaired electron, combined with X-ray diffraction structures of various peroxychromates should be able to give more insight in the electronic structure of these compounds.

The X-ray structure of  $\text{K}_3\text{CrO}_8$  (Figure 5.1) shows that the chromium atom is surrounded by 4 peroxide ions in an 8-coordinated dodecahedral environment, with  $D_{2d}$  symmetry. In early crystallographic analysis by Stomberg,<sup>13</sup> the oxygen atoms were assumed equidistant from the chromium atom; later studies by Swalen and Ibers indicated that the  $\text{Cr-O}_a$  distance is significantly shorter than the  $\text{Cr-O}_b$  distance (see also Table 5.1).<sup>12</sup> The  $\text{O}_a\text{-O}_b$  distance is slightly shorter than the 1.49 Å typically found for a peroxide ion.<sup>14</sup>

Earlier studies of the peroxychromates have shown that  $\text{Na}_3\text{CrO}_8$ ,  $\text{K}_3\text{CrO}_8$  and  $\text{Rb}_3\text{CrO}_8$  are isomorphous,<sup>2, 11</sup>  $\text{Li}_3\text{CrO}_8$  and  $\text{Cs}_3\text{CrO}_8$  have 10 respectively 3 water molecules per chromium ion in the unit cell.  $\text{Na}_3\text{CrO}_8$  also exists in a multiple hydrates; a hydrate with has 14 water molecules per chromium ion in the unit cell has been reported,<sup>11</sup> whereas in this study, a hydrate with 4 water molecules has been found. The  $\text{Cr}_8$  units of the hydrated compounds are more irregular, as was demonstrated by Dalal.<sup>2, 11</sup>

An initial description of the electronic structure of the  $\text{Cr}_8$  unit starts from a relatively simple electrostatic model.<sup>12, 15</sup> In this model, the oxygen atoms are viewed as point charges. Since the point symmetry of the  $\text{Cr}_8$  structure is  $D_{2d}$ , the chromium  $d$  orbitals are split in four: A1 ( $d_{z^2}$ ), B1 ( $d_{x^2-y^2}$ ), B2 ( $d_{xy}$ ) and E ( $d_{xz}$ ,  $d_{yz}$ ). This puts the unpaired electron in the  $d_{x^2-y^2}$  orbital.

The spin Hamiltonian of the chromium atom is given by

$$H = g_{\parallel}\beta H_z S_z + g_{\perp}\beta(H_x S_x + H_y S_y) + A_{\parallel}S_z I_z + A_{\perp}(S_x I_x + S_y I_y) \quad (5.1)$$

Using the purely ionic model described above, the spin Hamiltonian parameters also satisfy equations 5.2–5.5.

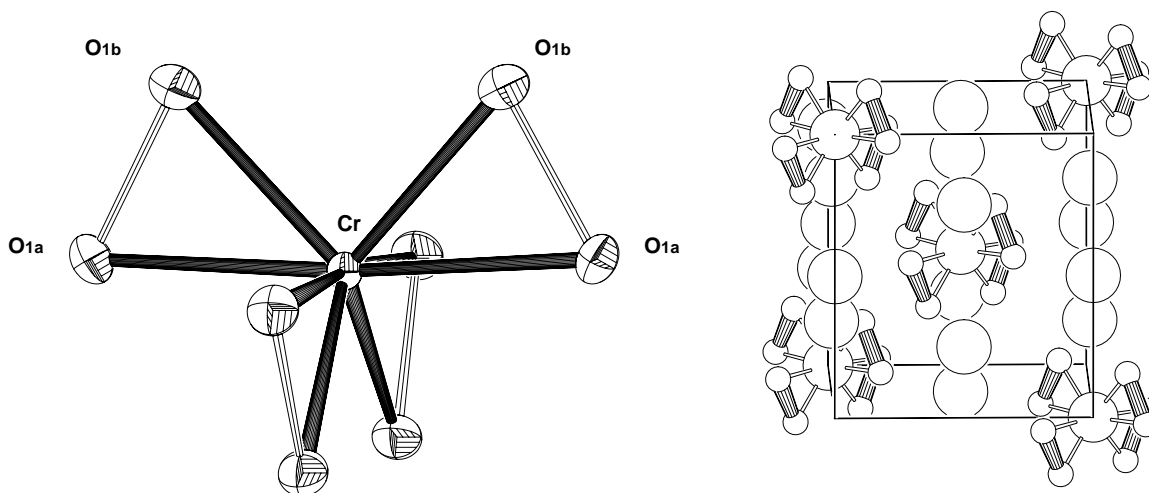
$$g_{\parallel} = g_e - \frac{8\lambda}{\Delta E_{xy}} \quad (5.2)$$

$$g_{\perp} = g_e - \frac{2\lambda}{\Delta E_{xz}} \quad (5.3)$$

$$A_{\parallel} = -\kappa + P \left( -\frac{4}{7} + (g_{\parallel} - g_e) + \frac{3}{7}(g_{\perp} - g_e) \right) \quad (5.4)$$

$$A_{\perp} = -\kappa + P \left( \frac{2}{7} + \frac{11}{14}(g_{\perp} - g_e) \right) \quad (5.5)$$

where  $g_e$  is the free electron  $g$  value (2.0023),  $\lambda$  is the spin-orbit coupling constant,  $\kappa$  is the isotropic hyperfine contact term arising from the polarization of inner  $s$  electrons by the unpaired spin in the  $d$ -orbital, and  $P = g_e g_n \beta_e \beta_N \langle r^{-3} \rangle_{av}$ .  $\Delta E_{xy}$  and  $\Delta E_{xz}$  represent the energy differences between the  $d_{x^2-y^2}$  and  $d_{xy}$  or  $d_{xz}$  orbitals.  $\kappa$  and  $P$  are related to the Cr unpaired electron wavefunction parameters  $|\Psi(0)|^2$  and  $\langle r^{-3} \rangle$ .<sup>16-18</sup>


**Figure 5.1:**

**Left:** Schematic structure of the  $\text{Cr}_8$  unit in the unhydrated peroxochromates  $\text{Na}_3\text{CrO}_8$ ,  $\text{K}_3\text{CrO}_8$  and  $\text{Rb}_3\text{CrO}_8$ .

**Right:**  $\text{K}_3\text{CrO}_8$  lattice as projected down the  $b$ -axis.

Using the literature values  $\lambda=383\text{ cm}^{-1}$ ,<sup>19</sup>  $\Delta E_{xy}=35000\text{ cm}^{-1}$  and  $\Delta E_{xz}=18000$ ,<sup>12, 15</sup> McGarvey calculated  $g_{\parallel} = 1.91$  and  $g_{\perp} = 1.96$ . Since these values are lower than the observed  $g$ -values, some covalent bonding must be included. Extending the group theoretical analysis to the eight Cr-O bonds yields that from these, two belong to the symmetry  $A_1$ , two to  $B_2$  and four to  $E$ . The possible combinations of the Cr orbitals with the oxygen orbitals are  $(s, d_{z^2})$ ,  $(p_z, d_{xy})$  and  $(p_x, p_y, d_{xz}, d_{yz})$ . If a linear combination of the chromium orbitals with the appropriate oxygen orbitals is made, the wavefunctions 5.6–5.8 are obtained:

$$\Phi_{cov}(x^2 - y^2) = \alpha d_{x^2-y^2}(\text{Cr}) + \sqrt{(1 - \alpha^2)^2} \Phi(B1)(O_2) \quad (5.6)$$

$$\Phi_{cov}(xz, yz) = \beta d_{xz}, d_{yz}(\text{Cr}) + \sqrt{(1 - \beta^2)^2} \Phi(E)(O_2) \quad (5.7)$$

$$\Phi_{cov}(xy) = \gamma d_{xy}(\text{Cr}) + \sqrt{(1 - \gamma^2)^2} \Phi(B2)(O_2) \quad (5.8)$$

As shown by Dalal,<sup>20</sup> equations 5.2–5.5 then expand to:

$$g_{\parallel} = g_e - \frac{8\lambda\alpha^2\gamma^2}{\Delta E_{xy}} \quad (5.9)$$



$$g_{\perp} = g_e - \frac{2\lambda\alpha^2\beta^2}{\Delta E_{xz}} \quad (5.10)$$

$$A_{\parallel} = -\kappa + P\left(-\frac{4}{7}\alpha^2 + (g_{\parallel} - g_e) + \frac{3}{7}(g_{\perp} - g_e)\right) \quad (5.11)$$

$$A_{\perp} = -\kappa + P\left(\frac{2}{7}\alpha^2 + \frac{11}{14}(g_{\perp} - g_e)\right) \quad (5.12)$$

In these equations,  $\alpha, \beta$  and  $\gamma$  are coefficients which indicate the weight of oxygen orbital mixing with the Cr  $d_{x^2-y^2}$ ,  $d_{xz,yz}$  and  $d_{xy}$  orbitals respectively. A value of 1 indicates a completely ionic bond; a value of  $1/2\sqrt{2}$  indicates a covalent bond.<sup>12</sup> Values smaller than  $1/2\sqrt{2}$  are not allowed, since then the wave function does not contribute to the paramagnetism.

Ideally, one would like to substitute the spin Hamiltonian parameters in equations 5.9–5.12 and calculate  $\alpha, \beta, \gamma, \kappa$  and  $P$  directly. Since the solution of equations 5.2–5.5 is underdetermined, this is not possible. Dalal tried to solve this problem by using equations 5.2–5.5 as an initial guess for  $\kappa$  and  $P$ , and then self-consistently solving equations 5.2–5.5. However, this implies  $\alpha=1$ , and also fixes the values of  $\beta$  and  $\gamma$ . This means that the values determined for  $\alpha, \beta$  and  $\gamma$  by Dalal are most likely incorrect.

It is however possible to obtain limits for the values of  $\alpha, \beta$  and  $\gamma$ . For example, if the  $g$  values for  $\text{K}_3\text{CrO}_8$  in  $\text{K}_3\text{NbO}_8$  (as determined by Dalal<sup>4</sup>) are substituted in equations 5.9–5.11, and the products  $\alpha^2\beta^2$  and  $\alpha^2\gamma^2$  are calculated, we obtain:

$$\alpha^2\beta^2 = 0.40 \quad (5.13)$$

$$\beta^2 = 0.59\gamma^2 \quad (5.14)$$

Combined with the inequalities  $1/2\sqrt{2} \leq \alpha, \beta, \gamma \leq 1$ , this limits  $\alpha, \beta$  and  $\gamma$  to:

$$0.83 \leq \alpha \leq 0.90 \quad 0.71 \leq \beta \leq 0.77 \quad 0.92 \leq \gamma \leq 1.00 \quad (5.15)$$

If these limiting values are used,  $\kappa$  and  $P$  for  $\text{K}_3\text{NbO}_8$  can be determined to be  $15.0 \cdot 10^{-4} \pm 0.2 \cdot 10^{-4} \text{ cm}^{-1}$ , resp.  $30.9 \cdot 10^{-4} \pm 0.2 \cdot 10^{-4} \text{ cm}^{-1}$ .

As shown in Figure 5.2,  $\kappa$  and  $P$  are strongly limited by the value of  $\alpha$ , which in turn depends strongly on the values of  $g_{\perp}$  and  $g_{\parallel}$ , as can be seen from equation 5.12. This means that  $g_{\perp}$  and  $g_{\parallel}$  need to be determined as accurately as possible. The most accurate way to obtain the spin Hamiltonian parameters would be to measure the  $g$ -values using high-frequency EPR, and measure the hyperfine parameters at 9 GHz.

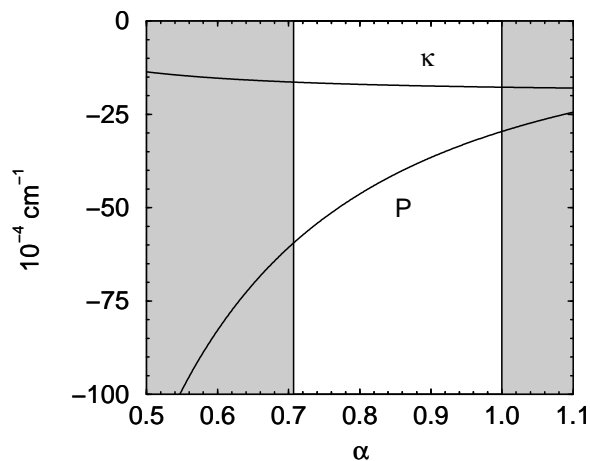


**Figure 5.2:** Dependency of the isotropic hyperfine contact term  $\kappa$  and the Cr unpaired electron wavefunction parameter  $P$  on the oxygen orbital mixing coefficient  $\alpha$ . The valid region for  $\alpha$  is indicated by the lines at  $\alpha = 1$  and  $\alpha = 1/2\sqrt{2}$ ; non-valid values for  $\kappa$  and  $P$  are grayed out.

It should be noted that it is impossible to determine the hyperfine parameters from pure peroxychromate powders, because the linewidth of the EPR spectra is broadened too much by dipolar and exchange interactions. The conventional solution for this problem is to dilute the compound of interest in an isomorphic diamagnetic compound, which for  $\text{K}_3\text{CrO}_8$  is  $\text{K}_3\text{NbO}_8$ . Another experimental difficulty is that in natural Cr, the most abundant Cr isotope ( $^{55}\text{Cr}$ ) has no nuclear spin; the abundance of  $^{53}\text{Cr}$  ( $I=3/2$ ) is only 9.5%. In exploratory experiments using Cr with natural concentrations  $^{53}\text{Cr}$ , it was found that some or all of the hyperfine components suffered from low S/N or were obscured by the  $I=0$  peak of  $^{55}\text{Cr}$ . A typical example is shown in the left spectrum of Figure 5.3(right). Using  $\text{Rb}_3\text{NbO}_8$  doped with  $^{53}\text{Cr}$  enriched  $\text{Cr}^{3+}$  gives the spectrum shown in Figure 5.3.

## 5.2 Experimental

### 5.2.1 Sample preparation

Pure  $\text{M}_3\text{CrO}_8$  crystals were grown using literature methods.<sup>1,21</sup>  $^{53}\text{Cr}$ -doped  $\text{M}_3\text{NbO}_8$  samples were made using the method of Balke and Smith,<sup>4,22</sup> with minor modifications.  $^{53}\text{Cr(V)}\text{O}_3$  was prepared from  $^{53}\text{Cr}_2\text{O}_3$  (97%  $^{53}\text{Cr}$ , Chemotrade GmbH) by fusing 5 mg  $^{53}\text{Cr}_2\text{O}_3$  with 0.17 g  $\text{KNO}_3$  and 0.19 g  $\text{Na}_2\text{CO}_3$ , and dissolving the residue in 5 mL water.  $\text{K}_3\text{CrO}_8$  in  $\text{K}_3\text{NbO}_8$  was prepared as described by Cage *et al.*<sup>4</sup>

**$\text{Li}_3\text{NbO}_8$ ,  $\text{Na}_3\text{NbO}_8$ :** A 100 mL beaker containing 1.1 g  $\text{Nb}_2\text{O}_5$  and 11.5 g  $\text{LiOH}\cdot\text{H}_2\text{O}$  (or 15 gr  $\text{NaOH}$ , for  $\text{Na}_3\text{NbO}_8$ ) was heated over a flame until gas evo-

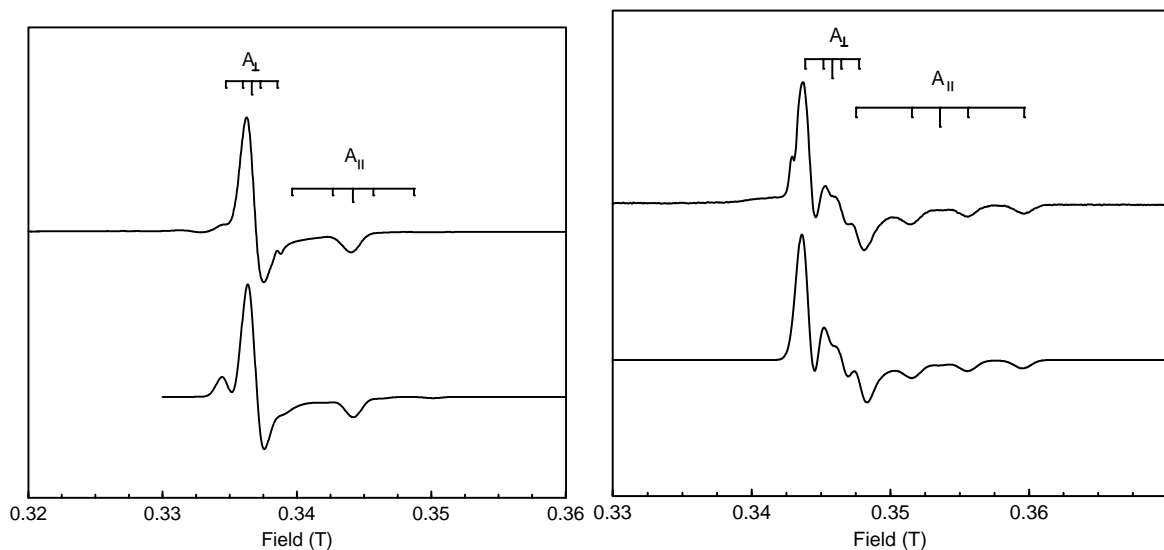


**Figure 5.3:** 9.2 GHz EPR spectra of Cr in  $\text{Rb}_3\text{NbO}_8$ , using Cr Cr with  $^{53}\text{Cr}$  in natural concentrations (left) and using 97%  $^{53}\text{Cr}$  (right).

lution had ceased. After cooling, the resulting solids were dissolved in 400 mL boiling water, and 1.6 mL of the  $^{53}\text{Cr}(\text{V})$  solution was added, followed by 10 mL of 30%  $\text{H}_2\text{NbO}_2$ .

**$\text{Rb}_3\text{NbO}_8$ ,  $\text{Cs}_3\text{NbO}_8$ :** A 100 mL beaker containing 0.3 g  $\text{Nb}_2\text{O}_5$  and 4.8 g  $\text{RbOH}$  (or 5 gr  $\text{CsOH}\cdot\text{H}_2\text{O}$ , for  $\text{Cs}_3\text{NbO}_8$ ) was heated over a flame until a clear liquid was obtained. After cooling, the resulting solid was dissolved in a minimum amount of distilled water (6 mL for  $\text{Rb}_3\text{NbO}_8$ , 3 mL for  $\text{Cs}_3\text{NbO}_8$ ), and 0.2 mL of the  $^{53}\text{Cr}(\text{V})$  solution was added, followed by 1.0 mL of 30%  $\text{H}_2\text{NbO}_2$ . The solution was placed in a refrigerator, yielding 1.5 g of slightly yellowish doped  $\text{Rb}_3\text{NbO}_8$  crystals. Crystal formation of  $\text{Cs}_3\text{NbO}_8$  was only possible if a top layer of ethanol or acetone was carefully added to the cold solution. The fused solid formed by Cs darkens quickly if exposed to light.

9 GHz EPR spectra were measured on a Bruker ER-220D spectrometer. EPR spectra were simulated using the computer program described in ref. 23.

## 5.2.2 X-ray diffraction

For all structures, single crystals were mounted in air on a glass fibre. Intensity data were collected at room temperature. An Enraf-Nonius CAD4 single-crystal diffractometer was used, using  $\text{Mo-K}\alpha$  radiation, in  $\theta - 2\theta$ -scan mode. Unit cell

**Table 5.1:** Interatomic distances (in Å) and angles in  $\text{M}_3\text{CrO}_8$  ( $\text{M}=\text{Li, Na, K, Rb, Cs}$ ).  $\text{Cr-O}_a$ ,  $\text{Cr-O}_b$  distances and  $\text{O}_a\text{-Cr-O}_a$ ,  $\text{O}_b\text{-Cr-O}_b$  angles for  $\text{Li}_3\text{CrO}_8$  and  $\text{Cs}_3\text{CrO}_8$  are averaged values. The distance given for  $\text{Cr-Cr}$  is the shortest  $\text{Cr-Cr}$  distance; this is not necessarily the distance which allows superexchange via the peroxide ions.

Compound	$\text{Cr-O}_a$	$\text{Cr-O}_b$	$\text{O}_a\text{-O}_b$	$\text{O}_a\text{-Cr-O}_a$	$\text{O}_b\text{-Cr-O}_b$	$\text{Cr-Cr}$	reference
$\text{Li}_3\text{CrO}_8 \cdot 10\text{H}_2\text{O}$	1.892	1.932	1.441	88.8	177.3	7.16	present work
$\text{Na}_3\text{CrO}_8 \cdot 14\text{H}_2\text{O}$	1.912	1.934	1.473	88.9	178.8	6.21	present work
$\text{K}_3\text{CrO}_8$	1.882	1.955	1.460	85.5	174.9	6.76	11
$\text{Rb}_3\text{CrO}_8$	1.874	1.958	1.457	88.5	176.6	6.29	present work
$\text{Cs}_3\text{CrO}_8 \cdot 3\text{H}_2\text{O}$	1.900	1.936	1.44	89.2	177.2	7.05	present work

dimensions were determined from the angular setting of 25 reflections. Intensity data were corrected for Lorentz and polarization effects. Semi-empirical absorption correction ( $\psi$ -scan)<sup>24</sup> was applied. The structure was solved by the program system DIRDIF<sup>25</sup> using the program PATTY<sup>26</sup> to locate the heavy atoms and was refined with standard methods (refinement against  $F^2$  of all reflections with SHELXL97<sup>27</sup>) with anisotropic parameters for all atoms. A structure determination summary and a list of atom coordinates are given in Table 5.6–5.9 respectively.

### 5.3 Results

From the crystal structures of the peroxychromates, the bond angles and distances in the  $\text{Cr}_8$  unit shown in Table 5.1 has been compiled. This table shows that — except for  $\text{Li}_3\text{CrO}_8$  — the distance between the oxygens in the peroxo ligand decreases in the order  $\text{Na} > \text{K} > \text{Rb} > \text{Cs}$ . atom, which suggests a change in the binding of the peroxo ligand.

Also, the metal-ligand distances appear to indicate a ‘twist’ of the peroxo ligand, with one  $\text{Cr-O}$  distance slightly increasing, and the other  $\text{Cr-O}$  distance slightly decreasing.

Unfortunately, these trends are not reflected with a similar clearness in the EPR data. The  $g$ -values of the pure peroxychromates (given in Table 5.3) show no clear trend in either direction, even if the hydrated peroxychromates are omitted.

It is assumed that the (electronic) structure of the peroxytitanate host is the same as the corresponding peroxychromate compound. Unfortunately, when the  $g$  values of the doped samples (given in Table 5.2) are compared with those of the pure compounds (Table 5.3), it seems that this is only the case for  $\text{K}$  and  $\text{Rb}$ .

Crystal structure analysis seems to agree with these findings;  $\text{Rb}_3\text{NbO}_8$  and  $\text{K}_3\text{NbO}_8$  are isomorphous with  $\text{K}_3\text{CrO}_8$ ,<sup>29,30</sup> whereas  $\text{Na}_3\text{NbO}_8$  exists as

**Table 5.2:** Spin Hamiltonian parameters for  $M_3CrO_8$  ( $M=Li, Na, K, Rb, Cs$ ) in  $M_3NbO_8$  at 9.3 GHz.

Compound	$g_x$	$g_y$	$g_z$	$A_{  }(10^{-4} \text{ cm}^{-1})$	$A_{\perp}(10^{-4} \text{ cm}^{-1})$	reference
$Li_3NbO_8$	1.985	1.985	1.950	$18.1 \pm 0.5$	$35.5 \pm 1$	present work
$Na_3NbO_8$	1.985	1.985	1.9485	$10.6 \pm 0.5$	$35.6 \pm 0.5$	present work
$K_3NbO_8$	1.9856	1.9856	1.9429	$10.4 \pm 0.1$	$37.06 \pm 0.1$	present work
$K_3NbO_8$	1.9851	1.9851	1.9427	$10.65 \pm 0.04$	$35.87 \pm 0.07$	4
$Rb_3NbO_8$	1.9845	1.9845	1.941	$12.0 \pm 0.5$	$37.0 \pm 0.3$	present work
$Cs_3NbO_8$	2.000	2.000	1.982	—	$23 \pm 3$	present work

**Table 5.3:** Spin Hamiltonian parameters for the pure peroxychromates, as determined using HF-EPR at 95 GHz by Dalal (taken from ref. 2 and 11)).

Compound	$g_x(\pm 0.0005)$	$g_y(\pm 0.0005)$	$g_z(\pm 0.0005)$
$Li_3CrO_8 \cdot 10H_2O$		1.9834	1.9533
$Na_3CrO_8$	1.9848	1.9802	1.9544
$Na_3CrO_8 \cdot 14H_2O$		1.9821	1.9476
$K_3CrO_8$	1.9852	1.9852	1.9431
$Rb_3CrO_8$	1.9825	1.9825	1.9426
$Cs_3CrO_8 \cdot 3H_2O$	1.9817	1.9702	1.9546

**Table 5.4:** OO-Cr LCAO parameters for the peroxychromates  $M_3CrO_8$  ( $M=Li, Na, K, Rb$ ). Values for Cs have been omitted due to excess error in the spin Hamiltonian parameters. The errors in  $\kappa$  and  $P$  have been calculated by taking the difference of the result from using  $\alpha_{min}$  and  $\alpha_{max}$  to determine  $\kappa$  and  $P$ .

Compound	$\alpha_{min}$	$\alpha_{max}$	$\beta_{min}$	$\beta_{max}$	$\gamma_{min}$	$\gamma_{max}$	$\kappa$	$P$
$Li_3CrO_8 \cdot 10H_2O$	0.77	0.90	0.71	0.83	0.86	1.00	$-17.10 \pm 0.61$	$-43.1 \pm 13.5$
$Na_3CrO_8$	0.78	0.90	0.71	0.81	0.87	1.00	$-17.13 \pm 0.54$	$-42.3 \pm 11.9$
$K_3CrO_8$	0.82	0.89	0.71	0.76	0.93	1.00	$-17.21 \pm 0.27$	$-40.7 \pm 6.0$
$K_3CrO_8^4$	0.83	0.90	0.71	0.77	0.92	1.00	$-17.24 \pm 0.32$	$-40.0 \pm 6.9$
$Rb_3CrO_8$	0.84	0.92	0.71	0.77	0.91	1.00	$-17.29 \pm 0.32$	$-38.8 \pm 7.0$

**Table 5.5:**

**Left:** Values of  $P$  for chromium ions, taken from ref. 17.

**Right:** Effect of bond order and charge on the bond lengths of dioxygen species, taken from ref. 28.

Ion	$P$	Ion	Bond order	O-O distance, Å
$Cr^{5+}$	50.2	$O_2^+$	2.5	1.123
$Cr^{4+}$	45.0	$O_2$	2	1.216
$Cr^{3+}$	39.7	$O_2^-$	1.5	1.28
$Cr^{2+}$	34.6	$O_2^{2-}$	1	1.49
$Cr^+$	29.5			
$Cr^0$	24.4			

$\text{Na}_3\text{NbO}_8 \cdot 13\text{H}_2\text{O}$ , in which the  $\text{Na}^+$  cations form hydrated trimers, which join together to form one-dimensional chains, intercalated irregularly by the  $\text{NbO}_8$  ions. This is in contrast to both  $\text{Na}_3\text{CrO}_8$  structures,<sup>11</sup> which are highly regular.

From the doped samples, the hyperfine parameters  $A_{\parallel}$  and  $A_{\perp}$  from Table 5.2 were determined. In combination with the  $g$ -values from the pure compounds, shown in Table 5.3, this gives the LCAO parameters shown in Table 5.4. In spite of the difficulties mentioned above,  $\kappa$  and  $P$  show a clear trend when varying the alkali metal ion. The average value of  $\kappa$  ( $17.2 \cdot 10^{-4} \text{ cm}^{-1}$ ) matches with the value observed by Dalal ( $17 \cdot 10^{-4} \text{ cm}^{-1}$ ),<sup>20</sup> but this is more likely caused by the relative insensitivity of  $\kappa$  to changes in  $\alpha$  (see Figure 5.2). However, this value does correspond well with the calculated value of  $17.3 \cdot 10^{-4} \text{ cm}^{-1}$ , which is the value of  $\kappa$  for  $\text{Cr(V)}$  complexes in which symmetry does not allow  $4s$  admixtures in the ground state.<sup>16, 17</sup>

The trends in  $\alpha_{min} \dots \gamma_{max}$  seem to suggest that the binding changes proceed mainly by an increase in the binding between the Cr  $d_{xz}$ ,  $d_{yz}$  orbitals and the oxygen  $p_{xyz}$  orbitals, combined with a simultaneous decrease of the contribution of the Cr  $d_{x^2-y^2}$  orbital.

If the values of  $P$  are compared with those for Cr in various oxidation states, as given in Table 5.5, it can be concluded that the average value of  $P$  ( $41.0 \cdot 10^{-4} \text{ cm}^{-1}$ ) is smaller than the theoretical value of  $50.2 \cdot 10^{-4} \text{ cm}^{-1}$  for  $\text{Cr}^{5+}$ , which suggests that there is considerable charge transfer in the Cr-O bond, from the peroxo ligand to the Cr ion, increasing in the order  $\text{Cs} > \text{Rb} > \text{K} > \text{Na} > \text{Li}$ . If the trends in  $P$  are compared with literature values for Cr in various oxidation states, it can be seen that the effective charge on the Cr atom decreases with increasing alkali metal size, suggesting that there is more electron density in the Cr-O bond. This is also in agreement with the decreasing bond lengths of the peroxo ligands; as can be seen from Table 5.5, superoxides ( $\text{O}_2^-$ ) have shorter bond lengths than peroxides ( $\text{O}_2^{2-}$ ).

## 5.4 Summary

Peroxychromates  $\text{M}_3\text{CrO}_8$  ( $\text{M}=\text{Li}, \text{Na}, \text{K}, \text{Rb}, \text{Cs}$ ) have been prepared and measured using X-band EPR. Information about the unpaired Cr-electron could be obtained by analyzing the trends in  $g$ -values and hyperfine parameters. Although the changes in these parameters are relatively small, they still allowed an estimation of lower and upper bounds for the isotropic hyperfine contact term  $\kappa$  and the parameter  $P$ , which is a measure for the dipolar hyperfine interaction. Comparing these parameters with literature values shows that the charge on the Cr atom decreases as a function of alkali metal atom, in the order  $\text{Cs} > \text{Rb} > \text{K} > \text{Na} > \text{Li}$ . From this trend, it can be concluded that the Cr-peroxide bond increases in strength in the same order, which means that the Cr-peroxide bond is the strongest in  $\text{Cs}_3\text{CrO}_8$ , and the weakest in  $\text{Li}_3\text{CrO}_8$ .

## 5.5 Acknowledgments

We wish to thank Professor Naresh Dalal (HFML, Tallahassee) for helpful discussions and for providing material prior to publication.

**Table 5.6:** Crystallographic data for  $\text{Li}_3\text{CrO}_8$ ,  $\text{Na}_3\text{CrO}_8$  and  $\text{K}_2\text{NaCrO}_8$ .

Empirical formula	$\text{Li}_3\text{CrO}_8 \cdot 10\text{H}_2\text{O}$	$\text{Na}_3\text{CrO}_8 \cdot 4\text{H}_2\text{O}$	$\text{K}_2\text{NaCrO}_8$
Crystal size (mm)	0.26x0.22x0.13	0.18x0.15x0.14	0.31x0.25x0.18
Formula weight	380.98	321.03	281.19
T(K)	293	293	293
Crystal system	Orthorhombic	Tetragonal	Orthorhombic
Space group	CmCm	P42/n	Pcam
a (Å)	7.5255(4)	6.217(3)	8.013
b (Å)	12.1934(15)	6.217(3)	8.6149(9)
c (Å)	16.7441(8)	12.630(4)	9.242(2)
$\alpha$ (°)	90	90	90
$\beta$ (°)	90	90	90
$\gamma$ (°)	90	90	90
V (Å <sup>3</sup> )	1536.5(2)	488.2(4)	638.0(3)
$\rho_{calc}$ (g cm <sup>-3</sup> )	1.647	2.184	2.928
Z	4	2	4
Wavelength (Å)	0.71073	0.71073	0.71073
F(000)	788	322	548
$\theta$ range (°)	3.18 to 26.28	5.65 to 26.25	3.47 to 25.94
Index ranges	$0 \leq h \leq 9$ $-15 \leq k \leq 0$ $-20 \leq l \leq 0$	$0 \leq h \leq 7$ $-7 \leq k \leq 0$ $0 \leq l \leq 15$	$-9 \leq h \leq 9$ $-10 \leq k \leq 10$ $-11 \leq l \leq 11$
Measured reflections	870	571	4600
Unique reflections	870	487	663
Observed reflections ( $I_o > 2\sigma(I_o)$ )	752	162	655
Refined parameters	86	24	66
Goodness-of-fit on F <sup>2</sup>	1.090	1.552	1.241
R ( $I_o > 2\sigma(I_o)$ )	0.0261	0.2053	0.0207
wR2 (all data)	0.0677	0.5624	0.0587
$\rho_{fin}$ (max/min) (e.Å <sup>-3</sup> )	0.346/-0.302	1.694/-1.941	0.374/-0.517



**Table 5.7:** Crystallographic data for  $\text{Li}_3\text{CrO}_8$ ,  $\text{Na}_3\text{CrO}_8$  and  $\text{K}_2\text{NaCrO}_8$ .

<b><math>\text{Li}_3\text{CrO}_8 \cdot 10\text{H}_2\text{O}</math></b>				
	x	y	z	U(eq)
Cr(1)	0	132(1)	2500	14(1)
O(1)	0	169(2)	1347(1)	26(1)
O(2)	0	1240(1)	1710(1)	26(1)
O(3)	1765(2)	-975(1)	2500	24(1)
O(4)	2567(2)	99(2)	2500	24(1)
O(5)	5000	1766(2)	5203(1)	30(1)
O(6)	2326(3)	0	5000	44(1)
O(7)	5000	409(2)	1285(1)	26(1)
O(8)	2224(2)	2419(1)	6281(1)	28(1)
Li(1)	5000	0	5000	30(1)
Li(2)	5000	1954(4)	926(3)	27(1)

<b><math>\text{Na}_3\text{CrO}_8 \cdot 4\text{H}_2\text{O}</math></b>				
	x	y	z	U(eq)
Cr(1)	2500	2500	2500	17(3)
Na(1)	7500	7500	2500	47(4)
Na(2)	7500	2500	3529(12)	47(4)
O(1)	260(3)	4700(3)	2490(17)	62(6)
O(2)	1080(3)	3990(4)	1416(19)	62(6)
O(3)	7500	2500	5390(2)	77(9)
O(4)	7500	7500	4273(17)	77(9)

<b><math>\text{K}_2\text{NaCrO}_8</math></b>				
	x	y	z	U(eq)
Cr(1)	-130(1)	2478(1)	7500	10(1)
K(1)	2500	5137(1)	5000	25(1)
K(2)	731(1)	1882(1)	2500	22(1)
Na(1)	2500	-774(1)	5000	18(1)
O(1)	-88(2)	2435(2)	5403(2)	19(1)
O(2)	905(2)	1236(2)	6081(2)	23(1)
O(3)	1701(3)	3885(2)	7500	20(1)
O(4)	108(3)	4663(2)	7500	20(1)
O(5)	-2060(3)	1114(2)	7500	20(1)
O(6)	-2469(3)	2755(2)	7500	20(1)

**Table 5.8:** Crystallographic data for  $\text{Rb}_3\text{CrO}_8$  and  $\text{Cs}_3\text{CrO}_8$ .

Empirical formula	$\text{Rb}_3\text{CrO}_8$	$\text{Cs}_3\text{CrO}_8 \cdot 3\text{H}_2\text{O}$
Crystal size (mm)	0.20x0.16x0.12	0.25x0.20x0.20
Formula weight	436.41	632.78
T(K)	293	293
Crystal system	Tetragonal	Monoclinic
Space group	$\bar{I}4_2$	P2(1)/n
a (Å)	6.97601(15)	8.4055(7)
b (Å)	6.97601(15)	12.0519(11)
c (Å)	7.8235(5)	11.5449(8)
$\alpha$ (°)	90	90
$\beta$ (°)	90	91.586(7)
$\gamma$ (°)	90	90
V (Å <sup>3</sup> )	380.730(18)	1169.07(16)
$\rho_{calc}$ (g cm <sup>-3</sup> )	3.807	3.595
Z	2	4
Wavelength (Å)	0.71073	0.71073
F(000)	398	1132
$\theta$ range (°)	3.91 to 26.21	2.96 to 26.28
Index ranges	$0 \leq h \leq 9$ $0 \leq k \leq 8$ $-9 \leq l \leq 0$	$-10 \leq h \leq 10$ $-14 \leq k \leq 0$ $-14 \leq l \leq 0$
Measured reflections	242	2484
Unique reflections	135	2368
Observed reflections ( $I_o > 2\sigma(I_o)$ )	121	2214
Refined parameters	20	136
Goodness-of-fit on F <sup>2</sup>	1.396	1.249
R ( $I_o > 2\sigma(I_o)$ )	0.0281	0.0311
wR2 (all data)	0.0865	0.0930
$\rho_{fin}$ (max/min) (e.Å <sup>-3</sup> )	0.816/-0.613	0.945/-0.759

**Table 5.9:** Crystallographic data for  $\text{Rb}_3\text{CrO}_8$  and  $\text{Cs}_3\text{CrO}_8$ .

<b><math>\text{Rb}_3\text{CrO}_8</math></b>				
	x	y	z	U(eq)
Rb(1)	0	0	5000	18(1)
Rb(2)	5000	0	2500	22(1)
Cr(1)	0	0	0	10(1)
O(1)	1290(8)	1290(8)	1759(10)	18(2)
O(2)	1983(7)	1983(7)	114(14)	17(2)

<b><math>\text{Cs}_3\text{CrO}_8 \cdot 3\text{H}_2\text{O}</math></b>				
	x	y	z	U(eq)
Cs(1)	2372(1)	762(1)	5144(1)	33(1)
Cs(2)	452(1)	879(1)	8473(1)	29(1)
Cs(3)	641(1)	5681(1)	3364(1)	32(1)
Cr(1)	94(1)	2371(1)	2485(1)	19(1)
O(1)	-1620(6)	1308(5)	2615(5)	31(1)
O(2)	-244(7)	1043(5)	3338(5)	34(1)
O(3)	-1351(7)	3564(5)	2563(5)	35(1)
O(4)	-794(7)	3256(5)	3714(5)	33(1)
O(5)	-202(6)	2387(5)	848(4)	29(1)
O(6)	920(6)	1535(4)	1205(5)	28(1)
O(7)	2174(6)	2471(5)	3184(5)	32(1)
O(8)	1866(6)	3387(5)	2397(5)	29(1)
O(9)	7272(7)	1033(5)	10100(5)	35(1)
O(10)	5869(7)	1377(5)	4048(5)	39(1)
O(11)	4146(7)	3275(6)	814(5)	41(1)

# Bibliography

- [1] B. Cage, K. Singh, S. Friedberg, S. Shimizu, J.S. Moodera, W.N. Lawless, and N.S. Dalal, *Solid State Comm.*, **2000**, *113*, 93.
- [2] B. Cage and N.S. Dalal, *Chem. Mater.*, **2001**, *13*, 880.
- [3] B. Cage, A.K. Hassan, L. Pardi, J. Krzystek, L.-C. Brunel, and N.S. Dalal, *J. Mag. Res.*, **1997**, *124*, 495.
- [4] B. Cage, A. Weekley, L.C. Brunel, and N.S. Dalal, *Anal. Chem.*, **1999**, *71*, 1951.
- [5] B. Cage and N.S. Dalal, *J. Appl. Phys.*, **2000**, *87*, 6031.
- [6] B. Cage, R. Leniek, and N.S. Dalal, *J. Appl. Phys.*, **2000**, *87*, 6010.
- [7] R.M. Wood, K.A. Abboud, C. Palenik, and G.J. Palenik, *Inorg. Chem.*, **2000**, *39*, 2065.
- [8] L. Vaska, *Acc. Chem. Res.*, **1976**, *9*, 175.
- [9] M. Roch, J. Weber, and A.F. Williams, *Inorg. Chem.*, **1984**, *23*, 4571.
- [10] J. Fischer, A. Veillard, and R. Weiss, *Theoret. Chim. Acta*, **1972**, *23*, 317.
- [11] B. Cage, W. Geyer, K.A. Abboud, and N.S. Dalal, *Chem. Mater.*, **2001**, *13*, 871.
- [12] J.D. Swalen and J.A. Ibers, *J. Chem. Phys.*, **1962**, *37*, 17.
- [13] R. Stomberg and C. Brosset, *Acta Chem. Scand.*, **1960**, *14*, 44.
- [14] L. Vaska, *Acc. Chem. Res.*, **1978**, *11*, 348.
- [15] B.R. McGarvey, *J. Chem. Phys.*, **1962**, *37*, 2001.
- [16] B.R. McGarvey, *J. Phys. Chem.*, **1967**, *71*, 51.
- [17] T. F. Yen, editor. *Charge transfer in the metal-ligand bond as determined by electron spin resonance*, Electron Spin Resonance of metal complexes, 1986.
- [18] L.B. Knight and W. Weltner, *J. Chem. Phys.*, **1971**, *55*, 434.
- [19] C.E. Moore, "Atomic Energy Levels", *National Bureau of Standards*, **1952**, *2*, 467.

- [20] N.S. Dalal, M.M. Suryan, and M.S. Seehra, *Anal. Chem.*, **1981**, 53, 938.
- [21] E.H. Riesenfeld, *Chem. Ber.*, **1905**, 38, 4066.
- [22] C.W. Balke and E.F. Smith, *J. Am. Chem. Soc.*, **1908**, 30, 1637.
- [23] W.R. Hagen, D.O. Hearshen, L.J. Harding, and W.R. Dunham, *J. Magn. Reson.*, **1985**, 61, 233.
- [24] A.C.T. North, D.C. Philips, and F.S. Mathews, *Acta. Cryst. A*, **1968**, 24, 351.
- [25] P.T. Beurskens, G. Beurskens, W.P. Bosman, R. de Gelder, S. Garcia-Granda, R.O. Gould, R. Israel, and J.M.M. Smits. *DIRDIF-96. A computer program system for crystal structure determination by Patterson methods and direct methods applied to difference structure factors*. Crystallography Laboratory, University of Nijmegen, The Netherlands, 1996.
- [26] P.T. Beurskens, G. Beurskens, M. Strumpel, and C.E. Nordman, *Patterson and Pattersons*, (Clarendon Press, Oxford), p. 356, 1987.
- [27] G.M. Sheldrick. *SHELXL-97. Program for the refinement of crystal structures*. University of Gottingen, Germany, 1997.
- [28] N.N. Greenwood and A. Earnshaw, *Chemistry of the elements*, (Pergamon Press, New York), p. 721, 1984.
- [29] H. Haeuseler, M. Wagener, and H Müller, *Z. Naturforsch.*, **1997**, 52 b, 1082.
- [30] I.A. Wilson, *Arkiv Kemi*, **1942**, 15, 1.

## Chapter 6

# Valence isomers of biological metal clusters: multiple forms of $[4\text{Fe-4S}]^{3+}$ clusters in HiPIPs \*

### 6.1 Abstract

The EPR powder pattern from the  $[4\text{Fe-4S}]^{3+}$  cluster in several High Potential Iron-sulfur Proteins (HiPIPs) is complex: it is not the spectrum of a single, isolated  $S=1/2$  system. However, EPR at 9, 35, and 130 GHz reveals that the apparent peak positions are frequency-independent in  $g$ -space: the spectrum is dominated by Zeeman interaction plus  $g$ -strain broadening. The spectra taken at frequencies above X-band are increasingly sensitive to rapid-passage effects, therefore the X-band data, which are slightly additionally broadened by dipolar interaction, have been used for quantitative spectral analysis. For a single geometrical  $[4\text{Fe-4S}]^{3+}$  structure the  $(\text{Fe}^{2.5+})_2$  mixed-valence dimer can be assigned in six different ways to a pair of iron ions, and this defines six theoretical valence isomers. Systematic multi-component  $g$ -strain simulation shows that the  $[4\text{Fe-4S}]^{3+}$  paramagnets in HiPIPs from seven different bacteria each consist of 3-5 discernible species, and these are assigned to actual valence isomers of the clusters. This interpretation constitutes a high-resolution extension of the current literature model, proposed from paramagnetic NMR, of a mixture of at least two mixed valence pairs that are averaged in the room temperature NMR experiments and not resolved in the low temperature Mössbauer spectra. The biological relevance of this complex magnetism, whose occurrence is not limited to the  $[4\text{Fe-4S}]^{3+}$  cluster, remains to be established.

---

\*submitted to J. Biol. Inorg. Chem.

## 6.2 Introduction

Molecular clusters are a form of matter with dimensions between those of molecules and of bulk material. A research plan for clusters containing paramagnetic transition ions is to unravel and to understand the clusters' magnetic properties as a result of their electronic structure. Biological metal clusters pose two additional levels of complexity. Firstly, the low symmetry of the biomacromolecules that form the clusters' external ligands imposes a lowering of the cluster symmetry. This makes it necessary to consider the influence of low symmetry on electronic and magnetic properties. Secondly, biomolecules are biologically relevant, which raises the question whether/how the complexity of a bio-cluster is related to its function in the cell. For example, it has been previously proposed that for iron-sulfur clusters with the core stoichiometry  $(\text{Fe}_2\text{S}_2)_n$  increasing complexity (i.e. increasing n-value) brings along an increase in versatility for multiple-electron redox biochemistry.<sup>1</sup> Although the magnetic properties of biomolecular clusters *per se* do not necessarily have direct biological relevance, again, they can be used as a tool to study electronic properties. The latter are related to low symmetry and to physiology.

A generic program to study magnetism of biomolecular clusters should be hierarchic: understanding should be built up gradually from simple systems to complex ones. For iron-sulfur clusters this means to start with the simplest possible [2Fe-2S] system, then to move on to the larger Fe/S structures, and finally to take a look at hybrid systems (i.e. containing heterometal ions and/or additional prosthetic groups). In a seminal series of studies of ferredoxins in the early seventies Dunham and Sands and collaborators have laid out the basic pattern for the reduced core [2Fe-2S]<sup>1+</sup>: the determinant is strong antiferromagnetic superexchange coupling between the irons. This results in spin ladders with low-spin ground state, localized valence, and exchange-induced paramagnetic shifts in NMR (summarized in ref. 2). The latter have subsequently been fully related to the localized valencies of the irons (summarized in ref. 3). Localized valence (i.e. cluster reduction leads to an extra electron localized on a specific iron ion) may well be a biologically relevant property, e.g., in the Rieske [2Fe-2S] cluster where reduction of the Fe coordinated by two solvent-exposed and deprotonatable histidines is functional in oxidative phosphorylation.<sup>4</sup>

Extending the analysis to larger clusters has been found to be problematic because exchange interaction in iron-sulfur clusters is of a dual nature: in addition to superexchange, leading to localized valence, there is spin frustration and double exchange, tending to de-localize the extra charges from reduction over more than one iron.<sup>5</sup> When a separated pair of  $\text{Fe}^{2+}$  and a  $\text{Fe}^{3+}$  ions is brought together under the interaction of double exchange the result is a mixed-valence pair of two indistinguishable  $\text{Fe}^{2.5+}$  ions. Current opinion has it that [4Fe-4S] cores are made up of

iron pairs dominated by double exchange interaction. For example, the  $[4\text{Fe-4S}]^{3+}$  core in HiPIPs can be thought of as the combination of a ferric pair ( $\text{Fe}^{3+}\text{-Fe}^{3+}$ ) and a mixed-valence pair ( $\text{Fe}^{2.5+}\text{-Fe}^{2.5+}$ ). This basic concept has been used to explain (and, therefore, to find support in) signs of  $^{57}\text{Fe}$  hyperfine couplings in Mössbauer spectra.<sup>6</sup> At "higher" temperatures,  $T \geq 77$  K, all four Fe ions are usually found to have very similar isomer shifts and quadrupole splittings i.e. to be essentially indistinguishable in terms of charge.<sup>6-9</sup> The pair-of-pairs model is a minimum hypothesis consistent with the limited resolution of the Mössbauer spectroscopic method for this problem. Theoretically, there are six different ways to take two Fe ions in a  $[4\text{Fe-4S}]$  cluster to form a mixed-valence pair; since the surrounding of the cluster in the proteins is asymmetric, the six possibilities should be electronically inequivalent and therefore observable. Multiplicity of  $[4\text{Fe-4S}]^{3+}$  sites has indeed been observed in the EPR of  $\gamma$ -irradiated single crystals of synthetic model compounds, and this has been assigned to topological multiplicity of the mixed-valence pair.<sup>10</sup> Multiple signals in the EPR of HiPIPs is a long-standing observation.<sup>11</sup> In selenium-substituted HiPIP this has also been found<sup>12</sup> and later suggested to be related to different topologies of the mixed-valence pair.<sup>13</sup> Paramagnetic shifts in  $^1\text{H-NMR}$  data of oxidized HiPIPs provides a clear indication for the occurrence at room temperature of more than one valence isomer, i.e. more than one pair-of-pairs. The NMR experiment defines a fast-exchange situation, and it has therefore been interpreted in terms of the average of (at least) two valence isomers.<sup>3, 14, 15</sup>

To put all these qualitative results on a quantitative footing we have systematically re-investigated the magnetic structure of HiPIP  $[4\text{Fe-4S}]^{3+}$  clusters using multi-frequency EPR spectroscopy and quantitative  $g$ -strain analysis.

## 6.3 Material & methods

### Proteins

The HiPIPs used in this study are from *Ectothiorhodospira vacuolata* strain b1, isoprotein-I, *Ectothiorhodospira vacuolata* strain b1, isoprotein-II, *Rhodopila globiformis* strain 7950, *Rhodocyclus gelatinosus* (strain 2.2.1) [previously: *Rhodopseudomonas gelatinosa*], *Rhodocyclus tenuis* (strain 2761) [previously: *Rhodospirillum tenue*], *Chromatium vinosum* strain D, *Ectothiorhodospira halophila*, isoprotein-I. The purification procedures were cited in ref. 16, except for *E. halophila*.<sup>15</sup>

### Spectroscopy

X-band (9 GHz) EPR was done on a Bruker ER 220 spectrometer. The Q-band (35 GHz) spectrometer was constructed from a Varian E 110 Q-band bridge, a Varian 60 MHz NMR magnet connected to a Varian EPR power supply, a PAR 117



lock-in amplifier and a home built cryo-insert plus modulation unit. The high-Q cylindrical TE011 cavity was constructed from silver-plated ‘wonderstone’ ceramic (pyrophyllite). The D-band (130 GHz) spectrometer was described previously in ref. 17.

### Analysis

The  $[4\text{Fe-4S}]^{3+}$  cluster in all oxidized HiPIPs studied thus far is an effective  $S=1/2$  system; high-spin signals have never been reported. Furthermore, since exchange interaction in the cluster is much stronger than the Zeeman interaction (e.g. referene11) no significant contributions are expected of excited-state manifolds of the spin ladder to the low-temperature EPR spectra. Therefore, the EPR is expected to be dominated by the Zeeman interaction and its distribution ( $g$ -strain) with possibly minor contributions from intermolecular dipolar interaction and from unresolved superhyperfine interaction. This expectation is confirmed by multi-frequency experiments (see below). This means that the previously developed  $g$ -strain simulator<sup>18-20</sup> can be applied for quantitative data analysis, as it is based on the assumption of  $S=1/2$  subject to Zeeman interaction, distributed by an external source, plus a small residual broadening to account for weak, unresolved interactions that contribute to the overall inhomogeneous line width. The simulator is particularly suited to address the question of detectability of valence isomers, because it was developed for analysis of spectra from multiple overlapping components.<sup>19</sup> The appropriate line-width expression in  $g$ -space for an  $S=1/2$  system subject to  $g$ -strain is:<sup>20</sup>

$$W = |l_x^2 g_x \Delta_{xx} + l_y^2 g_y \Delta_{yy} + l_z^2 g_z \Delta_{zz} + l_x l_y \Delta_{xy} \sqrt{g_x g_y} + l_x l_z \Delta_{xz} \sqrt{g_x g_z} + l_y l_z \Delta_{yz} \sqrt{g_y g_z}| / g + W_0$$

The parameters  $g_i$  are the three principal values of the  $g$ -matrix values. The  $g$ -strain is generally not co-linear with  $g$ , therefore, it is usually parameterized in terms of six line-width parameters ( $\Delta_{xx}, \Delta_{yy}, \Delta_{zz}, \Delta_{xy}, \Delta_{xz}, \Delta_{yz}$ ) that form the elements of a real, symmetric line-width matrix, and that describe the elements of the  $g$ -strain matrix in the axis system of the  $g$ -matrix (i.e. in the average molecular axes system). The dimensionality of the line-width matrix being three reflects the assumption of full statistical correlation between the principal values of the  $g$ -strain matrix.<sup>18</sup> The last term,  $W_0$ , is an independent, isotropic contribution to the line width as an effective description of the bundled minor, unresolved interactions.

Altogether, the above analysis means that a single spectral component (one valence isomer) is described by a minimum of ten EPR parameters. The cross terms  $\Delta_{ij}$  and the residual term  $W$  may each be zero (i.e. undetectably small) reducing the number of parameters to less than ten but at least six; all  $\Delta$ -values may be positive or negative (from negative correlation between the magnitudes of p-matrix elements). In case of one or more negative  $\Delta$ 's the  $g$ -strain line width becomes

zero for at least one intermediate orientation (i.e. B not along one of the molecular axes). In that case a finite  $W$  takes the additional role of a protection against numerical zero-divide even though the actual value of  $W$  is much smaller than the  $\Delta_{ii}$ 's and, therefore, not a significant fitting parameter. An initial estimate of the  $g$ -values and the values of  $|\Delta_{ii}|$  is usually readily read out from the experimental data.

## 6.4 Results

### Multi-frequency EPR of HiPIPs

The EPR of  $[2\text{Fe-2S}]^{1+}$  in proteins is determined by a combination of interactions independent of the external field, B, and interactions linear in B (Zeeman interaction and  $g$ -strain). Increasing the microwave frequency and, therefore, the field B makes the interactions linear in B dominant.<sup>21</sup> These are the proper conditions to determine the multiplicity (if any) and stoichiometry of individual components corresponding to the spectrum. The situation for  $[4\text{Fe-4S}]^{3+}$  clusters in HiPIPs is less clear. Few data taken at frequencies other than X-band have been published.<sup>11</sup> Also, X-band EPR of HiPIPs typically shows a complexity (see below) not found in the spectra of  $[2\text{Fe-2S}]$  ferredoxins. In one case, *C. vinosum* HiPIP in the presence of 0.2 M NaCl, the complexity has been analyzed in terms of a dipolar interaction resulting from dimerization.<sup>7</sup>

We have measured the EPR of HiPIPs at 9, 35, and 130 GHz in order to determine the relative contribution of interactions linear in B and independent of B. As an example, we present in fig. 6.1 the multi-frequency data for *C. vinosum* HiPIP under non-dimerizing conditions. This example was chosen because the *C. vinosum* protein has the most complex spectrum of all HiPIPs studied by us (see below). The figure illustrates an unexpected practical difficulty in these types of experiments. Although the samples used are pure and of high concentration (typically several mM), and although the EPR spectra are relatively sharp, the Q-band and especially D-band spectra suffer from relatively poor signal-to-noise ratios and imperfect baselines. We found that the EPR of these systems can only be obtained over a narrow temperature window. This window shifts to higher values and reduces in width with increasing frequency. A qualitative interpretation of this phenomenon is proposed in the Discussion section, below. Typical limiting values are approximately 15–30 K in X-band, 25–35 K in Q-band, and a few degrees around 35 K in D-band. Above the higher limit, the spectra broaden by lifetime broadening (T1- or spin- lattice relaxation). Below the lower limit, the spectra progressively distort by rapid- passage effects and eventually become undetectable. In D-band, it was usually not possible to obtain conventional absorption-derivative spectra. The D-band trace of fig. 6.1 was initially obtained in dispersion mode, and subsequently

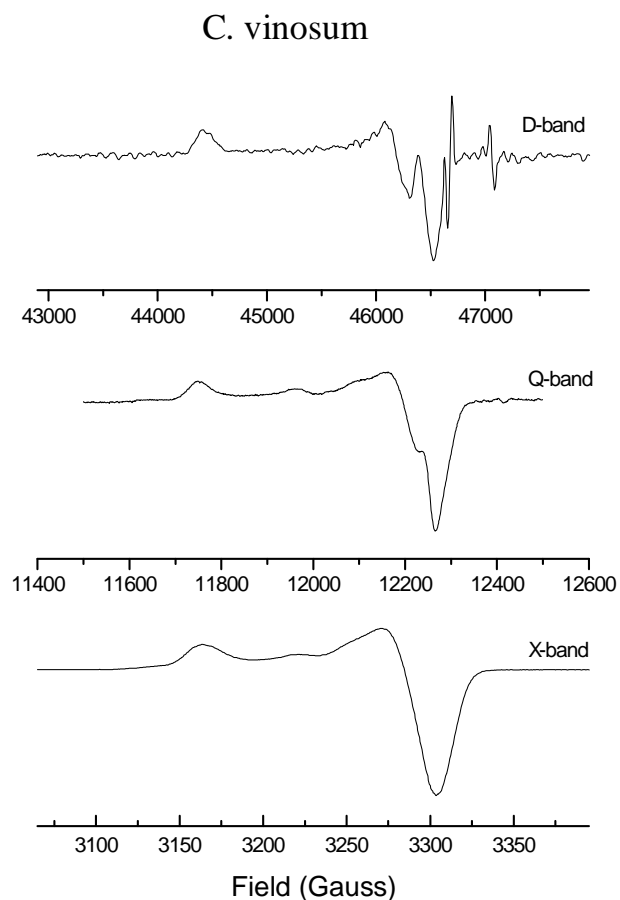


**Figure 6.1:** Multi-frequency EPR of *C. vinosum* HiPIP at 130, 35, and 9 GHz. The three spectra were aligned on a reciprocal  $g$ -value scale to show that all spectral features (except line widths) are positionally invariant, and therefore represent real  $g$ -values. EPR conditions (D, Q, X): microwave frequency, 129987, 34940, 9414 MHz; microwave power, 0.64, 0.5, 0.2 mW; modulation frequency, 25, 80, 100 kHz; modulation amplitude, 6, 4, 4 Gauss; temperature, 35, 25, 15 K.

filtered and differentiated according to ref.<sup>22</sup>

In spite of these experimental difficulties, it is clear from figure 6.1 that the *positions* of all the spectral features are invariant in  $g$ -space. Therefore, they are real  $g$ -values and are not caused by field-independent interactions such as dipole-dipole interac-

tions between clusters in different molecules. This means that we can use the spectra as a basis for multi-component analysis to identify multiple valence isomers. The X-band spectra are significantly broader than the higher-frequency spectra, which indicates significant contribution of unresolved B-independent interactions. However, we chose to use the X-band data for our component analyses because: 1) the high-frequency data usually suffer from some distortion from rapid-passage effects which precludes determination of stoichiometries; 2) the extra broadening at X-band is not dominant (no spectral feature is lost) and is essentially isotropic, therefore it can be easily modeled in the numerical analysis.

### **Stepwise $g$ -strain analysis of *C. vinosum* wild-type HiPIP**

The X-band EPR spectrum of *C. vinosum* HiPIP was analyzed under a  $g$ -strain model, starting from the simplest possible assumption of a single component of high symmetry, and subsequently stepwise increasing the complexity of the model until a quantitative fit of the data was obtained. That fit provides the minimum hypothesis for the interpretation of the spectrum. The major conclusion is that the experimental spectrum is consistent with the existence of more than two valence isomers.

The procedure is illustrated in fig. 6.2 with the fitting parameters compiled in table 6.1. In the top trace, the experimental spectrum was fitted assuming a single component of axial symmetry (i.e.  $g_x = g_y$ ). This initial fit indicates that there is one major component contributing to the overall spectrum, but that it is not of high symmetry. The next step, trace b, is a fit with a single rhombic spectrum with anisotropic  $g$ -strain. After optimization, at least three spectral features remain to be accounted for. Also the major 'perpendicular' feature (the  $g_x, g_y$  region) shows a poor fit in terms of the ratio of the positive and negative amplitudes i.e. intensity above and below the baseline. Allowing the  $g$ -strain to be non-colinear with  $g$  (i.e.  $\Delta_{ij} < 0$ ) gives no significant improvement (not shown). The smallest step of increasing complexity is to assume that the remaining three features are all from one additional rhombic species. The optimized fit is in trace c. Although the overall shape appears to be qualitatively correct, the intensities are consistently wrong at the  $g_z$  of the second species and also at the trough of the  $g_y$  feature of the second species.

Further progress required a change of paradigm: what was assumed to be a  $g_y$  of a second species (i.e. a derivative-shaped feature) is really a  $g_z$  of a third species (i.e. an absorption-shaped feature). In general, all the features on the low-field side of the main perpendicular feature in this and all other HiPIP spectra (see below) can only be fitted assuming that they are all different  $g_z$ 's. This implies that all spectra consist of  $> 3$  components (valence isomers).

The next step was to keep the parameters of the major rhombic component approximately constant and to add two additional components initially assuming axial

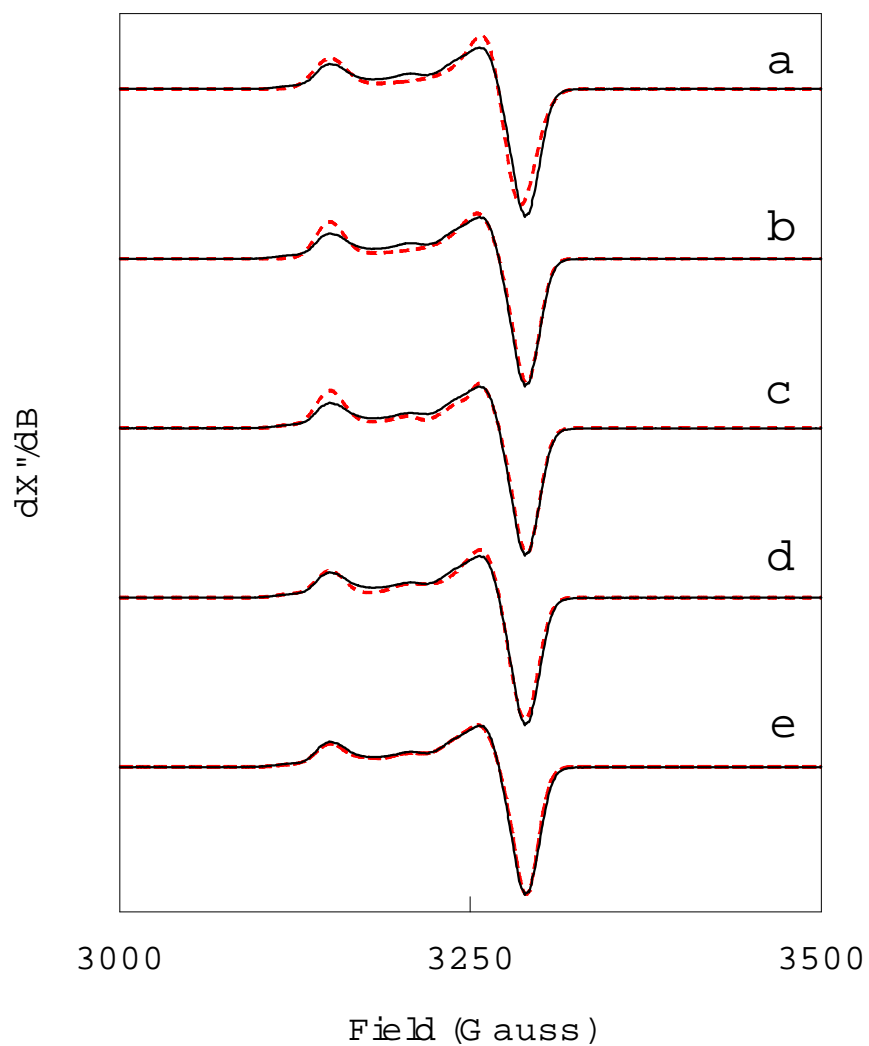


**Figure 6.2:** Different simulation models for the X-band EPR of *C. vinosum* HiPIP. The fitting, with increased complexity, shows that the spectrum consists of (at least) five different components, and these are identified with valence isomers. See the text for details. The fitting parameters for models a-e are given in Table 6.1.

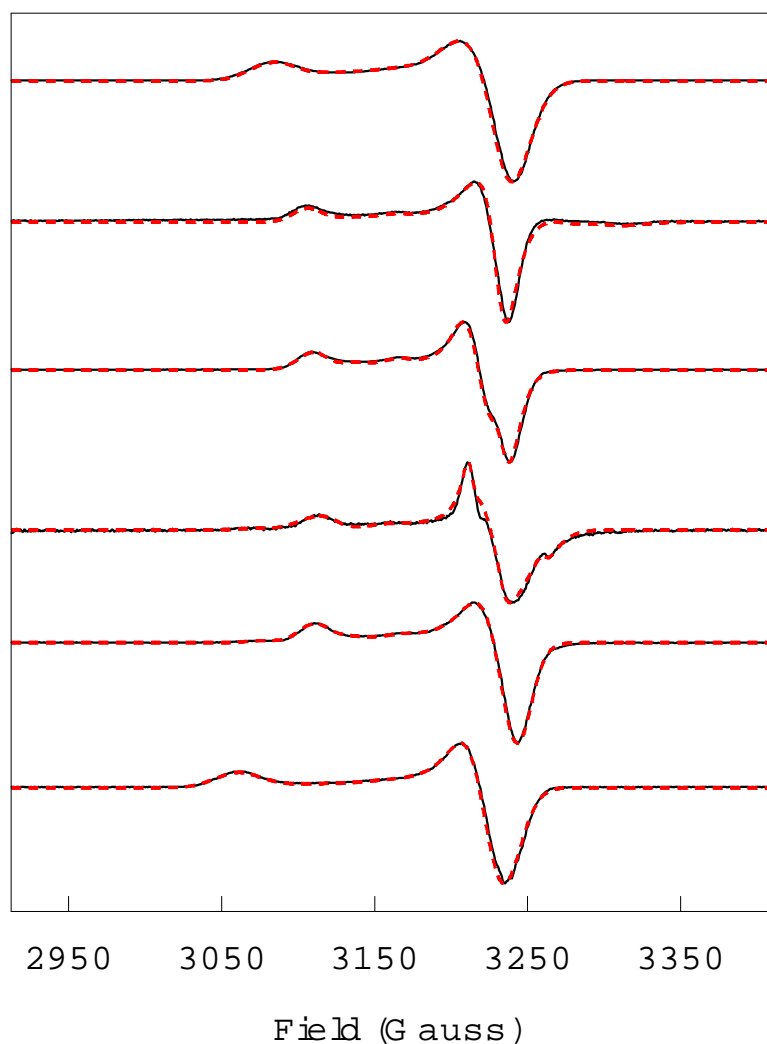


**Figure 6.3:** Optimized simulations of the X-band EPR spectra of HiPIP from (from top to bottom) *R. globiformis*, *R. gelatinosus*, *R. tenuis*, *E. vacuolata, iso-I*, *E. vacuolata iso-II*, and *E. halophila iso-I*. The fitting parameters are compiled in Table 2. EPR conditions: microwave frequency, 9.18 GHz, microwave power, 0.2-0.8 mW; modulation frequency, 100 kHz; modulation amplitude, 5 Gauss, temperature 27 K.

**Table 6.1:** Parameters of different simulation models (Wild type *C. vinosum* HiPIP)

	$g_x, g_y, g_z$	$\Delta_x, \Delta_y, \Delta_z$	Ratio
model-a (single axial component)	2.042, 2.042, 2.126	9, 9, 9	
model-b (single rhombic component)	2.035, 2.0485, 2.126	6, 9, 8	
model-c (all remaining features are one rhombic component)	2.035, 2.0485, 2.126 2.062, 2.085, 2.147	6, 9, 8 3, 5, 7	1 0.05
model-d (remaining features are absorption-like)	2.035, 2.0485, 2.126 2.042, 2.042, 2.145 2.042, 2.042, 2.090	6, 9, 8 8, 8, 8 8, 8, 8	1 0.15 0.15
model-e (all minor features are $g_z$ from rhombic spectra)	2.035, 2.0485, 2.126 2.035, 2.0485, 2.090 2.036, 2.0485, 2.109 2.036, 2.0485, 2.145 2.042, 2.067, 2.067	6, 9, 8 5, 9, 8 5, 9, 8 5, 9, 8 5, 6, 6	1 0.18 0.18 0.12 0.015

symmetry. From the fit, trace d, it is concluded that yet two more components must be present. Also a poor fit of the positive/negative intensity of the major perpendicular region persists. The latter was cured by making the first two minor components rhombic with  $g$ -strain anisotropy comparable to that of the main component. Then, the third and the fourth minor components were added and optimized. After a final global optimization, the resulting trace e was obtained with the parameters shown in table 6.1. Of course the overlap in the perpendicular region is considerable, therefore not all the parameters of each individual component have been determined. However, a major conclusion can be drawn that the EPR spectrum of *C. vinosum* HiPIP requires a minimum of five separate components to be fitted.

### Systematic inventory of HiPIP EPR

The EPR of seven HiPIPs from six sources was analyzed. The final results are compiled in fig. 6.3 and table 6.2. Two HiPIPs have a minor spectral component that is suspect since its  $g$ -values differ significantly from all other sets found: *E. vacuolata* isoprotein-I ( $g_x = 2.00$ ) and *R. gelatinosus* ( $g_x = 1.98$ ). These minor components are possibly from breakdown products.

**Table 6.2:**  $g$ -Strain parameters and weighing factors for all HiPIPs.

a) When  $g$ -values of minor components are (virtually) identical to those of the main component, this means that the minor-component parameters are not resolved and the numbers uses in the simulation are dummies.

b) *E. halophila* II HiPIP has been reported to be present as a single isomer with  $g$ -values 2.024, 2.034, 2.145.<sup>23</sup>

	$g_x, g_y, g_z$	$\Delta_x, \Delta_y, \Delta_z$	$\Delta_{xy}, \Delta_{xz}, \Delta_{yz}$	fractional intensity
<i>E. halophila</i> I	2.0295, 2.035, 2.1435	9, 8.8, 12.5	0, 0, 0	0.91
	2.0295, 2.035, 2.11	9, 8.8, 12.5	0, 0, 0	0.05
	2.0295, 2.035, 2.08	9, 8.8, 12.5	0, 0, 0	0.04
<i>R. globiformis</i>	2.025, 2.039, 2.128	9, 10, 12.5	3, 0, 0	0.80
	2.0265, 2.0265, 2.08	9, 9, 11	0, 0, 0	0.08
	2.0265, 2.0265, 2.10	9, 9, 11	0, 0, 0	0.12
<i>E. vacuolata</i> I	2.0287, 2.0287, 2.109	10.5, 10.5, 10	0, 7, 7	0.70
	2.007, 2.031, 2.0438	5, 4, 2.5	5.7, 0, 3	0.14
	2.0275, 2.0275, 2.077	8.5, 8.5, 9	0, 0, 0	0.08
	2.027, 2.027, 2.138	9, 9, 9	0, 0, 0	0.08
<i>E. vacuolata</i> II	2.025, 2.038, 2.112	6.5, 6.5, 8	3, 0, 0	0.70
	2.0265, 2.0265, 2.075	6.5, 6.5, 8	0, 0, 0	0.07
	2.0265, 2.0265, 2.135	6.5, 6.5, 9	0, 0, 0	0.13
	2.0265, 2.0265, 2.095	6.5, 6.5, 8	0, 0, 0	0.10
<i>C. vinosum</i>	2.035, 2.0485, 2.126	6, 9, 8	0, 0, 0	0.67
	2.035, 2.0485, 2.09	5, 9, 8	0, 0, 0	0.12
	2.036, 2.0485, 2.109	5, 9, 8	0, 0, 0	0.12
	2.036, 2.0485, 2.145	5, 9, 8	0, 0, 0	0.08
	2.042, 2.067, 2.067	5, 6, 6	0, 0, 0	0.01
<i>R. gelatinosus</i>	2.0305, 2.0305, 2.1127	7.5, 7.5, 7.5	3, 0, 0	0.64
	1.978, 2.004, 2.047	8, 8, 8	0, 8, 8	0.10
	2.03, 2.03, 2.076	7, 7, 8.5	3, 0, 0	0.13
	2.03, 2.03, 2.094	7, 7, 8.5	3, 0, 0	0.13
<i>R. tenuis</i>	2.024, 2.0388, 2.110	5, 5.5, 7.5	3, 5, 5	0.67
	2.024, 2.0388, 2.075	5, 5.5, 8	3, 5, 5	0.13
	2.024, 2.0388, 2.095	5, 5.5, 9	3, 5, 5	0.20



For some fits a significant non-colinearity of the  $g$ -strain was required. None of the spectra have the complexity of the *C. vinosum* wild-type HiPIP EPR, however, all fits are indicative of at least three different components. As a general conclusion, we can state that the current literature model of HiPIPs as constituted of different valence isomers<sup>3,14,15</sup> is: i) indeed valid, and ii) must be extended to more than two isomers to account for the complexity found in the  $g$ -strained EPR from the  $[4\text{Fe-4S}]^{3+}$  cluster of any of seven different HiPIP proteins.

## 6.5 Discussion

### Generalization of the valence-isomer model

In an early Mössbauer study on the  $[4\text{Fe-4S}]^{3+}$  cluster of *C. vinosum* HiPIP, Dickson *et al.*<sup>24</sup> found a qualitative dichotomy in the form of two opposing hyperfine fields in the spectra taken with an applied magnetic field and at a temperature of 4 K, which suggested an inequivalence in the iron ions. ENDOR measurements by Anderson *et al.*<sup>25</sup> led to a similar conclusion. In a subsequent attempt at quantitative Mössbauer spectroscopy, in 1980, Middleton *et al.*<sup>6</sup> decided to fit their data under the model of two independent components in a one-to-one stoichiometry. This key assumption implies two types of iron ions grouped as pairs, which translates to the 'reasonable' physical picture of a  $(\text{Fe}^{3+}\text{-Fe}^{3+})$  pair and a  $(\text{Fe}^{3+}\text{-Fe}^{2+})$  pair with delocalization of the extra electron over the mixed-valence pair, and with parallel magnetic coupling between irons within a pair and antiparallel coupling between the pairs, resulting in the observed system spin  $S=1/2$ . The authors of the 1980 pairwise model were careful to note that it "may correspond to a considerable oversimplification", but also that "fitting the Mössbauer data with more elaborate models is probably not meaningful".<sup>6</sup> In addition, they noted that the model does not apply to HiPIP at temperatures of 77 K and up, because the Mössbauer spectroscopy indicated four very similar irons apparently with identical formal valencies of  $\text{Fe}^{2.75+}$ .<sup>6</sup> A subsequent Mössbauer study on *E. halophila* HiPIP-II was confirmative of the model at low temperature and its breakdown at higher temperatures.<sup>8</sup> In a recent study of *E. halophila* HiPIP-I, using ENDOR and Mössbauer spectroscopy, Dilg *et al.*<sup>9</sup> conclude similarly, and they propose a refinement of the data analysis by inclusion of electronic relaxation and of low-symmetry effects.

In the present work we explored a full generalization of the model of a pair-of-pairs in which the assignment of the mixed-valence pair is not a priori limited to one pair (or to a minimum of two pairs, based on paramagnetically shifted NMR, see below) of iron ions in a cluster. This generalization was already implicit in the the 1980-model of Middleton *et al.*,<sup>6</sup> however, at that time experimental data of sufficient resolution and theoretical tools of sufficient sophistication for meaningful testing were not available.

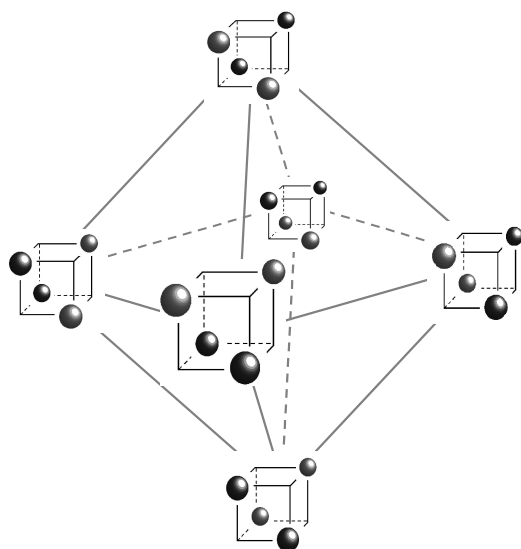


**Figure 6.4:** A graphical representation of the generalized pair-of-pairs model for tetrahedral  $[4\text{Fe}-4\text{S}]^{3+}$  cores. Mixed-valence pairs are shown in dark gray, all-ferric pairs are in light gray, sulfide ions have been omitted. The six possible valence isomers interconvert through interchange of one dark gray  $\text{Fe}^{2.5+}$  and one light gray  $\text{Fe}^{3+}$ .

The generalized model is graphically represented in fig. 6.4. The addition of an electron to a fully oxidized  $[4\text{Fe(III)}-4\text{S}]$  cluster is assumed to result in delocalization over two iron ions, indicated in the graph as dark gray balls. This results in six chemically fully equivalent valence isomers. The isomers can be interconverted into each other by formal transfer of half-a-charge from one iron ion to another (interchange of a dark and a light gray ball). Arranging these 12 interconversions using non-crossing reaction paths results in the octahedral scheme of fig. 6.4. Three additional interconversions, viz along the body diagonals of the octahedron, have not been drawn because they represent formal transfer of one full charge (complete interchange of dark and light gray). Rapid equilibrium between all six isomers would represent delocalization of the extra electron over all four iron ions, and this is a model for high-temperature Mössbauer data. Asymmetry of ligation external to the  $[4\text{Fe}-4\text{S}]$  core, as in a protein, would render the six isomers electronically and energetically inequivalent. This, combined with relatively slow interconversion rates between isomers, forms a model for low-temperature EPR data.

### Relation to previous EPR studies

In the present work, the dominant factors determining the detailed shape of the EPR powder pattern of HiPIPs have been determined to be the Zeeman interaction combined with  $g$ -strain. Therefore, quantitative analysis of HiPIP EPR requires an appropriate tool to describe  $g$ -strain. The statistical theory of  $g$ -strain was developed in the course of the '80s.<sup>18-21</sup> In early EPR studies on HiPIPs, line-shape analysis was based on a (usually poorly documented) ad hoc description of inhomogeneous broadening as a symmetrical distribution in magnetic-field space colinear with the  $g$ -matrix. Therefore, these analyses can only be expected to provide very qualitative indication of signal multiplicity.

Antanaitis and Moss<sup>11</sup> were the first, in 1975, to use frequency-dependent EPR for the study of HiPIP. The data on *C. vinosum* HiPIP taken at 9 and 35 GHz clearly indicated that the peak positions correspond to real  $g$ -values and that broadening is dominated by  $g$ -strain, although this conclusion was not drawn at that time. Spectral simulation of signal multiplicity indicated two major and one minor species, which is qualitatively and quantitatively inconsistent with our present analysis. It was later shown by Dunham *et al.*<sup>7</sup> that *C. vinosum* HiPIP dimerizes upon freezing in high-salt solution (a typical condition to store HiPIPs), which results in dipolar interaction. Moulis *et al.*<sup>12</sup> studied the selenium derivative of *C. vinosum* HiPIP, i.e. containing a  $[4\text{Fe-4Se}]^{3+}$  cluster. Simulation of the spectrum required four rhombic species with respective weight of 65, 18, 10, 7%. This result is somewhat closer to ours for the native protein (cf. Table 2), however, this simulation was not based on a rationalized broadening model, therefore it can only be qualitatively correct at best. The same ad hoc simulation approach was very recently applied to the EPR of *E. halophila* HiPIP-I,<sup>9</sup> and the result (one major and only one minor component) is qualitatively similar to ours (three components, cf. Table 2). Gloux *et al.*<sup>11</sup> and Le Pape *et al.*<sup>13</sup> have studied model compounds containing the  $[4\text{Fe-4S}]^{3+}$  core using single-crystal EPR. The dilute  $[4\text{Fe-4S}]^{3+}$  centers were created by  $\gamma$ -irradiation of crystallized  $[4\text{Fe-4S}]^{2+}$  core containing compounds. The detected multiplicity in sites was interpreted in terms of different topologies for the mixed-valence pair. Interestingly, five different species were identified for a symmetrical and three different species for an asymmetrical model compound, which goes some way towards our suggestion that in a fully symmetrical  $[4\text{Fe-4S}]^{3+}$  cluster each of the six possible topologies for the mixed-valence pair should be equally likely.

Gloux *et al.*<sup>11</sup> also discuss the EPR spectrum of *C. vinosum* HiPIP, and, with reference to unpublished experiments by J. Gaillard, they reach the conclusion that the spectrum is made up of four different components. The interpretation is partially based on different saturation behavior of spectral features. We would like to point out that the theory of  $g$ -strain implies continuously varying saturation behavior over the powder envelope of a single species;<sup>21</sup> therefore, differential saturation is not a reliable criterion for deconvolution of these complex spectra.

In one case only thus far, has it been possible to quantitatively super-reduce a HiPIP to the  $[4\text{Fe-4S}]^{1+}$  state: Heering *et al.*<sup>26</sup> have super-reduced *R. globiformis* HiPIP with Ti(III)citrate. The resulting X-band EPR spectrum shows multiplicity of components, and this indicates that the occurrence of valence isomers in biological  $[4\text{Fe-4S}]$  clusters is not limited to the 3+ state. Also, the  $[4\text{Fe-S}_4]^{1+}$  core in  $\gamma$ -irradiated model compounds occurs in more than one form.<sup>11</sup>

### Relation to average paramagnetic NMR shifts

Bertini *et al.*<sup>14, 15, 27, 28</sup> were the first to show that the model of a single, localized mixed valence pair was insufficient to explain the complex pattern of temperature-dependent paramagnetic shifts in the resonances from  $\beta$ -CH<sub>2</sub> protons in HiPIP. They proposed a minimum model with two topologies for the mixed-valence pair, which was parameterized in terms of the percentage ferric character, of a particular iron ion of the cluster (Cys-36 bound Fe in *E. halophila* HiPIP-I<sup>15</sup>). A plot of averaged hyperfine shift of, e.g., the  $\beta$ -CH<sub>2</sub> protons of Cys-36 versus the percentage ferric character was found to be approximately linear. The point of calibration was the shift data from *E. halophila* HiPIP-II. Its  $[4\text{Fe-4S}]^{3+}$  cluster exists supposedly as a single valence isomer based on EPR<sup>23</sup> and NMR data.<sup>15, 29</sup>

It is at present not possible to assign a specific EPR sub-spectrum to a specific geometrical valence isomer. Therefore, it is not obvious how the NMR and EPR data can be compared quantitatively. In the quoted NMR analysis, the percent ferric character of Cys-36 bound Fe runs from 24% (*E. halophila* I) to 70% (*R. gelatinosus*). The EPR intensities reported in Table 2 cannot be grouped in a set that would be quantitatively consistent with the percent ferric character deduced from NMR. This inconsistency may well reflect different valence isomer distributions at cryogenic (EPR) and ambient (NMR) temperatures. Indeed, inspection of the fractional intensities of the various isomers at low temperature suggests that, at variance with room temperature estimates, one isomer is always largely predominant over the others.

Nevertheless, a qualitative correlation is indicated. The isomer having the mixed-valence pair on the irons bound to cysteines II and III (counting system defined in<sup>15</sup>), and assumed to be the only one present in the HiPIP II from *E. halophila*, could be the one with the highest  $g_z$  feature ( $g_z = 2.145$ ). According to NMR data, the relative amount of this isomer decreases in the order: *E. halophila* II > *E. halophila* I > *R. globiformis* > *E. vacuolata* I > *E. vacuolata* II > *C. vinosum* > *R. gelatinosus*.

In the EPR spectra, the isomer with the highest  $g_z$  value decreases in a similar order: *E. halophila* II > *E. halophila* I > *R. globiformis* > *E. vacuolata* II > *E. vacuolata* I = *C. vinosum* and is absent in *R. gelatinosus*. For the isomer with the mixed valence pair bound to cysteines III and IV,<sup>15</sup> the correlation is less obvious, but this could correspond to the EPR isomer which is dominant in *E. vacuolata* I and II, *R. gelatinosus* and *R. tenuis*. This isomer would be characterized by a  $g_z$  value of 2.103–2.113. *C.*

*vinosum* HiPIP is left out of these correlations because its  $g_z$  value is intermediate between those of the other two isomers and because it has the spectrum with the largest number of species.

## 6.6 Concluding remarks

The present work is the first attempt to quantitatively resolve valence isomers in  $[4\text{Fe-4S}]^{3+}$  clusters in HiPIPs. Multiple forms have been observed for all HiPIPs studied, however, the number of forms identified never exceeds the theoretical maximum of six for a single structure, which indicates that the cluster can still be defined to be in a single  $S=1/2$  magnetic ground state at low temperatures.

The present results are consistent with those from other spectroscopies, notably low-temperature Mössbauer, low-temperature ENDOR, ambient-temperature NMR, in the sense that the first two methods apparently provide insufficient resolution for the positive identification of the multiplicity of forms detectable with EPR, and the third method only gives access to a time averaged spectrum.

A biological relevance of multiple valence isomers has not been established. In recent years it has become increasingly clear that the (main) biological function of HiPIPs is electron transfer between membrane-bound respiratory-chain complexes of photosynthetic bacteria (cf. references 30–32). It is possible that valence isomer multiplicity is related to the redox chemistry of the proteins. To our knowledge, no experimental data (e.g. EPR lineshape analysis as a function of redox potential) are available at present to test such a hypothesis.

## 6.7 Acknowledgements

This work was supported in part by the European Commission through the HMC Network Programme 'Structure-function relationships of iron-sulfur proteins', ER-BCHRXTC940626, and by the National Institutes of Health, GM 21277.

# Bibliography

- [1] W.R. Hagen, A.J. Pierik, and C. Veeger, *J. Chem. Soc. Faraday Trans.*, **1989**, 85, 4083.
- [2] R.H. Sands and W.R. Dunham, *Quart. Rev. Biophys.*, **1974**, 7, 443.
- [3] I. Bertini, S. Ciurli, and C. Luchinat, *Struct. Bonding*, **1995**, 83, 1.
- [4] T.A. Link, *Adv. Inorg. Chem.*, **1999**, 47, 83.
- [5] V. Papaefthymiou, J.-J. Girerd, I. Moura, J.J.G. Moura, and E. Münck, *J. Am. Chem. Soc.*, **1987**, 109, 4703.
- [6] P. Middleton, D.P.E. Dickson, C.E. Johnson, and J.D. Rush, *Eur. J. Biochem.*, **1980**, 104, 289.
- [7] W.R. Dunham, W.R. Hagen, J.A. Fee, R.H. Sands, J.B. Dunbar, and C. Humblet, *Biochim. Biophys. Acta*, **1991**, 1079, 253.
- [8] I. Bertini, A.P. Campos, C. Luchinat, and M. Teixeira, *J. Inorg. Biochem.*, **1993**, 52, 227.
- [9] A.W.E. Dilg, G. Mincione, K. Achterhold, O. Iakovleva, M. Mentler, C. Luchinat, I. Bertini, and F.G. Parak, *J. Biol. Inorg. Chem.*, **1999**, 4, 727.
- [10] J. Gloux, P. Gloux, B. Lamotte, J.-M. Mouesca, and G. Rius, *J. Am. Chem. Soc.*, **1994**, 116, 1953.
- [11] B.C. Antanaitis and T.H. Moss, *Biochim. Biophys. Acta*, **1975**, 405, 262.
- [12] J.-M. Moulis, M. Lutz, J. Gailliard, and L. Noodleman, *Biochemistry*, **1988**, 27, 8712.
- [13] L. le Pape, B. Lamotte, J.M. Mouesca, and G. Rius, *J. Am. Chem. Soc.*, **1997**, 119, 9757.
- [14] L. Banci, I. Bertini, S. Ciurli, S. Ferretti, C. Luchinat, and M. Piccioli, *Biochemistry*, **1993**, 32, 9387.
- [15] I. Bertini, F. Capozzi, L.D. Eltis, I.C. Felli, C. Luchinat, and M. Piccioli, *Inorg. Chem.*, **1995**, 34, 2516.
- [16] H.A. Heering, Y.B.M. Bultink, W.R. Hagen, and T.E. Meyer, *Biochemistry*, **1995**, 34, 14675.
- [17] P.J. van Dam, A.A.K. Klaassen, E.J. Reijerse, and W.R. Hagen, *J. Magn. Reson.*, **1997**, 130, 140.
- [18] W.R. Hagen, D.O. Hearshen, R.H. Sands, and W.R. Dunham, *J. Magn. Reson.*, **1985**, 61, 220.

- 
- [19] W.R. Hagen, D.O. Hearshen, L.J. Harding, and W.R. Dunham, *J. Magn. Reson.*, **1985**, *61*, 233.
- [20] W.R. Hagen, *Advanced EPR; Applications in biology and biochemistry*, (Elsevier, Amsterdam), p. 785–812, 1989.
- [21] W.R. Hagen and S.P.J. Albracht, *Biochim. Biophys. Acta*, **1982**, *702*, 61.
- [22] A. Savitzky and M.J.E. Golay, *Anal. Chem.*, **1964**, *36*, 1627.
- [23] R. Kappl, S. Ciurli, C. Luchinat, and J. Hüttermann, *J. Am. Chem. Soc.*, **1999**, *121*, 1925.
- [24] D.P.E. Dickson, C.E. Johnson, R. Cammack, M.C.W. Evans, D.O. Hall, and K.K. Rao, *Biochem. J.*, **1974**, *139*, 105.
- [25] R.E. Anderson, G. Anger, L. Petersson, A. Ehrenberg, R. Cammack, D.O. Hall, R. Mullinger, and K.K. Rao, *Biochim. Biophys. Acta*, **1975**, *376*, 63.
- [26] H.A. Heering, Y.B.M. Bulsink, W.R. Hagen, and T.E. Meyer, *Eur. J. Biochem.*, **1995**, *232*, 811.
- [27] I. Bertini, F. Briganti, C. Luchinat, A. Scozzafava, and M. Sola, *J. Am. Chem. Soc.*, **1991**, *113*, 1237.
- [28] I. Bertini, F. Capozzi, S. Ciurli, C. Luchinat, L. Messori, and M. Piccioli, *J. Am. Chem. Soc.*, **1992**, *114*, 3332.
- [29] L. Banci, I. Bertini, F. Capozzi, P. Carloni, S. Ciurli, C. Luchinat, and M. Piccioli, *J. Am. Chem. Soc.*, **1993**, *115*, 3431.
- [30] A. Hochkoeppler, S. Ciurli, G. Venturoli, and D. Zannoni, *FEBS Lett.*, **1995**, *357*, 70.
- [31] A. Hochkoeppler, D. Zannoni, S. Ciurli, T.E. Meyer, M.A. Cusanovich, and G. Tollin, *Proc. Natl. Acad. Sci. U.S.A.*, **1996**, *93*, 6998.
- [32] M.M. Pereira, J.N. Carita, and M. Teixeira, *Biochemistry*, **1999**, *38*, 1276.

# Summary

This thesis describes the application of high-frequency electron paramagnetic resonance (HF-EPR) on several (model) systems, representing different classes of magnetic (bio)molecules. EPR is a technique which allows the determination of the electronic structure of materials containing unpaired electrons. This is possible because elementary particles such as protons and electrons have a property called 'spin', which is best compared to a small electric charge, spinning around its axis. The effect of spin is that every particle can be regarded as a tiny magnet. If a magnetic field is applied to a particle with spin, the spin of the particle can be aligned along the direction of the magnetic field or against the direction of the magnetic field. The two states are of different energy. Using the proper amount of energy (in the form of microwave radiation for electrons, and radiowaves for protons) spins can be transferred from one state to another.

The precise amount of energy required to enable this transition strongly depends on the environment of the unpaired electron, and on the interactions it has with its environment. In other words, the required amount of energy contains chemical information. The energies of the interactions between electrons and atomic nuclei (hyperfine interactions) are usually rather small. This type of interactions can be studied in great detail with conventional EPR spectrometers. An example of such a study is given in chapter 5, wherein the chromium-oxygen bond in  $M_3CrO_8$ -compounds (with  $M=Li, Na, K, Rb$  or  $Cs$ ) is investigated.

Some transition metals (especially iron, cobalt, nickel and manganese) can have electronic states in which several unpaired electrons are present. In these states the systems are called 'high-spin systems'. The energies of the interactions between the unpaired electrons in high spin systems are usually much larger than hyperfine interactions. Since this interaction is also present without magnetic field applied, it is also termed 'zero field interaction'. The size of the zero field splitting is determined to a very large extent by the environment of the atom, i.e. again a source of chemical information. High spin systems are often also chemically and biologically relevant; research on this interaction should result in a complete picture of the electronic structure of the metal centre.

Due to the size of the zero field splitting, EPR spectra of high spin systems mea-



sured at conventional frequencies are often either too complicated to analyse in a straightforward way, or not very informative. If these measurements are taken using higher microwave frequencies (130 to 380 GHz), the zero field interaction is much easier to analyse.

In chapter 2 it is shown that the spectrometer designs as used in conventional EPR spectrometers can not be simply translated to higher microwave frequencies. It is better to adapt the resonator of the HF-EPR spectrometer to the relaxation behavior of the sample.

In chapter 3, several high spin systems are measured over a range of microwave frequencies, varying from 4 to 380 GHz. Although the EPR spectra of the studied systems are simplified greatly at higher frequencies, it also turned out that every spin parameter has its own optimum frequency area. For a correct determination of all spin parameters, EPR spectra at several frequencies are required. Furthermore, HF-EPR allows the determination of distributions in the zero field splitting parameters, which can be correlated to structural distributions in the environment of the high-spin system.

Chapter 4 shows that distributions in zero field splitting parameters are the cause of the characteristic lineshape of EPR-spectra of  $\text{Fe}^{3+}$  in Fe(III)-EDTA and in the protein rubredoxin. Although it is possible to obtain an impression of the size of these distribution using 9 and 35 GHz EPR spectra, it remains difficult to determine the shape of these distributions, even using 130 GHz EPR. It is expected that future technological developments in HF-EPR will allow these distributions to be determined much easier using HF-EPR at 300 to 600 GHz.

In the final two chapters typical applications of 'conventional' EPR are described. In chapter 5, alkali-chromium complexes are studied using EPR, with the intention to obtain more insight in the electronic structure of the chromium complexes. The measurements in this chapter show that the effective charge on the chromium atom decreases as a function of the alkali metal atom, in the order  $\text{Cs} > \text{Rb} > \text{K} > \text{Na} > \text{Li}$ .

In Chapter 6 is shown that the 9 GHz EPR spectra of so-called High Potential Iron-Sulfur Proteins (HiPIPs) can be described as a superposition of 3–5 different species, which can be assigned to actual valence isomers of the iron-sulfur cluster. This interpretation is an extension of the existing model based on data obtained using paramagnetic NMR.

# Samenvatting

Dit proefschrift beschrijft de toepassing van hoog-frequent electron paramagnetische resonantie (HF-EPR) op verschillende (model)systemen. EPR is een techniek die het mogelijk maakt om de electronische structuur van materialen met ongepaarde electronen te bestuderen. Dit is mogelijk doordat elementaire deeltjes zoals protonen en electronen een eigenschap hebben die 'spin' wordt genoemd, die nog wel het beste kan worden vergeleken met een ronddraaiende elektrische lading, die om zijn as draait. Het effect van 'spin' is dat ieder deeltje kan worden beschouwd als een klein magneetje. Als een deeltje met spin in een magneetveld wordt gebracht, kan de spin van het deeltje zich met het veld mee richten, of tegen het veld in gaan staan. De twee toestanden hebben verschillende energie. Met behulp van de juiste hoeveelheid energie (in de vorm van microgolffstraling voor electronen, en radiogolven voor protonen) kunnen spins van de ene naar de andere toestand worden overgebracht.

De preciese hoeveelheid energie die nodig is om een electronspin van de ene naar de andere toestand over te brengen is sterk afhankelijk van de omgeving waarin het electron zich bevindt, en welke interacties het electron heeft met zijn omgeving. De energieën van de interacties die electronen met atoomkernen hebben, zijn meestal vrij klein. Dit soort interacties zijn met conventionele EPR-apparatuur dan ook goed te bestuderen. Een voorbeeld van zo'n studie staat in hoofdstuk 5, waarin de chroom-zuurstof binding in verbindingen van het type  $M_3CrO_8$  (waarin M een lithium-, natrium-, kalium-, rubidium of cesium-atoom is) wordt onderzocht.

Sommige overgangsmetalen (met name ijzer, cobalt, nikkel en mangaan) kunnen meerdere ongepaarde electronen bezitten; in dat geval worden ze ook wel 'hoog-spin' systemen genoemd. De energieën van interacties tussen verschillende ongepaarde electronen in een hoog-spin systeem zijn meestal veel groter. Omdat deze interactie ook aanwezig is zonder magnetisch veld, wordt dit ook wel de 'nulveldsplitsing' genoemd. De grootte van de nulveldinteractie wordt in hoge mate door de omgeving van het atoom bepaald. Hoog-spin systemen zijn vaak ook chemisch en biologisch relevant; onderzoek van deze interactie zou uiteindelijk een beeld moeten geven van de electronische structuur van het metaalcentrum.

Vanwege de grootte van de nulveldinteractie zijn EPR-spectra van hoog-spin systemen bij conventionele frequenties (9 GHz) te gecompliceerd om op een eenvoudige manier te analyseren, of niet erg informatief. Door metingen uit te voeren bij hogere microgolffrequenties (130 tot 380 GHz) is deze interactie wel eenvoudig te analyseren.

Hoofdstuk 2 laat zien dat de spectrometerontwerpen zoals die in gebruik zijn voor EPR-spectrometers bij conventionele frequenties niet exact gekopieerd kunnen worden naar hogere microgolffrequenties. Om zo min mogelijk experimentele problemen te hebben, is het het beste om de resonator van de spectrometer aan te passen aan het relaxatiegedrag van het te bestuderen systeem.

In hoofdstuk 3 worden een aantal hoog-spin systemen gemeten bij verschillende microgolffrequenties, variërend van 4 tot 380 GHz. Hoewel EPR-spectra van de onderzochte systemen heel erg vereenvoudigd worden bij hogere frequenties, blijkt ook dat iedere systeemp parameter zijn eigen optimale frequentiegebied heeft. Om alle spinparameters goed te kunnen bepalen, zijn EPR-spectra gemeten bij verschillende frequenties nodig. Wel is het zo dat verdelingen in de nulveldsplittingsparameters goed bepaald kunnen worden met HF-EPR. Deze parameters kunnen ook gecorreleerd worden aan structurele verdelingen in de directe omgeving van het hoog-spin systeem.

Hoofdstuk 4 laat zien dat verdelingen in nulveldsplittingsparameters de oorzaak zijn van de karakteristieke lijnvorm van EPR-spectra van  $\text{Fe}^{3+}$  in Fe(III)-EDTA en in rubredoxine-eiwitten. Hoewel het mogelijk is om met behulp van 9 en 35 GHz EPR-spectra een indruk te krijgen hoe groot deze verdelingen zijn, blijft het lastig om de vorm van de verdelingen eenduidig te achterhalen. Hoewel de nulveldsplittingsinteracties in deze systemen zelfs voor de frequenties die hier gebruikt zijn nog te groot zijn, is wel duidelijk dat deze distributies met HF-EPR (bij 300 tot 600 GHz) in principe veel gemakkelijker zijn te bepalen.

De laatste twee hoofdstukken beschrijven typische toepassingen van 'conventionele' EPR. In hoofdstuk 5 worden verschillende alkali-chroom-complexen bestudeerd met EPR, met de bedoeling om aan de hand van met EPR bepaalde parameters meer inzicht in de elektronische structuur van de chroom-complexen te krijgen. Het blijkt dat de effectieve lading op het chroom-atoom afneemt als functie van het alkali-atoom, in de volgorde  $\text{Cs} > \text{Rb} > \text{K} > \text{Na} > \text{Li}$ .

In hoofdstuk 6 wordt beschreven dat de 9 GHz EPR spectra van zogeheten High Potential Iron-Sulfur Proteins (HiPIPs) beschreven kunnen worden als een superpositie van 3–5 verschillende species, waarbij ieder spectrum toegewezen kan worden aan valentieisomeren van het ijzer-zwavel cluster. Deze interpretatie is een uitbreiding van het bestaande model, wat gebaseerd is op data verkregen met behulp van paramagnetische NMR.

# Curriculum Vitae

Alex Priem werd op 26 augustus 1971 geboren te Leiden. In 1989 behaalde hij het VWO-diploma aan het Willem van Oranje College te Waalwijk. In september 1989 is hij begonnen met de studie scheikunde aan de Katholieke Universiteit Nijmegen, alwaar in 1989 het propedeutisch examen werd behaald. Het doctoraal examen werd in augustus 1995 afgelegd met als hoofdvakrichting Organische Chemie bij Prof. Dr. R.J.M. Nolte en als uitgebreide bijvakrichting Experimentele Vaste Stof Fysica bij Prof. Dr. H. van Kempen. Vanaf december 1995 was de schrijver werkzaam als assistent in opleiding bij de afdeling molecuulspectroscopie onder begeleiding van Prof. Dr. W.R. Hagen. De resultaten van het in deze periode verrichte onderzoek worden in dit proefschrift beschreven.